ARISTOTLE UNIVERSITY OF THESSALONIKI
SCHOOL OF GEOLOGY
DEPARTMENT OF GEOLOGY

PAVLOS K. BONATIS
Geologist

# STRONG GROUND MOTION SIMULATION IN THE CENTRAL IONIAN ISLANDS USING A HYBRID (DETERMINISTIC AND STOCHASTIC) APPROACH

MASTER THESIS

*POSTGRADUATE STUDIES PROGRAMME 'APPLIED & ENVIRONMENTAL GEOLOGY', DIRECTION: 'APPLIED GEOPHYSICS & SEISMOLOGY'*

THESSALONIKI
2020

PAVLOS K. BONATIS
ΠΑΥΛΟΣ Κ. ΜΠΟΝΑΤΗΣ
Πτυχιούχος Γεωλόγος

# STRONG GROUND MOTION SIMULATION IN THE CENTRAL IONIAN ISLANDS USING A HYBRID (DETERMINISTIC AND STOCHASTIC) APPROACH

# ΥΠΟΛΟΓΙΣΜΟΣ ΕΔΑΦΙΚΗΣ ΚΙΝΗΣΗΣ ΣΤΗΝ ΠΕΡΙΟΧΗ ΤΩΝ ΚΕΝΤΡΙΚΩΝ ΙΟΝΙΩΝ ΝΗΣΩΝ ΜΕ ΕΦΑΡΜΟΓΗ ΥΒΡΙΔΙΚΗΣ (ΑΙΤΙΟΚΡΑΤΙΚΗΣ ΚΑΙ ΣΤΟΧΑΣΤΙΚΗΣ ΜΕΘΟΔΟΛΟΓΙΑΣ

Υποβλήθηκε στο Τμήμα Γεωλογίας στα πλαίσια του Προγράμματος Μεταπτυχιακών Σπουδών 'Εφαρμοσμένη και Περιβαλλοντική Γεωλογία', Κατεύθυνση 'Εφαρμοσμένη Γεωφυσική και Σεισμολογία'

Ημερομηνία Προφορικής Εξέτασης: 17/02/2020
Oral Examination Date: 17/02/2020

**Three-member Examining Board**

Karakostas Vassileios Professor AUTH, Supervisor
Papadimitriou Eleftheria Professor AUTH, Member
Kaviris Georgios Assistant Professor NKUA, Member

**Τριμελής Εξεταστική Επιτροπή**

Καρακώστας Βασίλειος Καθηγητής ΑΠΘ, Επιβλέπων
Παπαδημητρίου Ελευθερία Καθηγήτρια ΑΠΘ, Μέλος Τριμελούς Εξεταστικής Επιτροπής
Καβύρης Γεώργιος Επίκουρος Καθηγητής ΕΚΠΑ, Μέλος Τριμελούς Εξεταστικής Επιτροπής

STRONG GROUND MOTION SIMULATION IN THE CENTRAL IONIAN ISLANDS USING A HYBRID (DETERMINISTIC AND STOCHASTIC) APPROACH – *Master Thesis*


ΥΠΟΛΟΓΙΣΜΟΣ ΕΔΑΦΙΚΗΣ ΚΙΝΗΣΗΣ ΣΤΗΝ ΠΕΡΙΟΧΗ ΤΩΝ ΚΕΝΤΡΙΚΩΝ ΙΟΝΙΩΝ ΝΗΣΩΝ ΜΕ ΕΦΑΡΜΟΓΗ ΥΒΡΙΔΙΚΗΣ (ΑΙΤΙΟΚΡΑΤΙΚΗΣ ΚΑΙ ΣΤΟΧΑΣΤΙΚΗΣ ΜΕΘΟΔΟΛΟΓΙΑΣ – *Μεταπτυχιακή Διπλωματική Εργασία*

Citation:
Bonatis P. K., 2020. - Strong ground motion simulation in the Central Ionian Islands using a hybrid (deterministic and stochastic) approach. Master Thesis, School of Geology, Aristotle University of Thessaloniki, # pp.
Μπονάτης Π. Κ., 2020. - Υπολογισμός εδαφικής κίνησης στην περιοχή των Κεντρικών Ιονίων Νήσων με εφαρμογή υβριδικής (αιτιοκρατικής και στοχαστικής) μεθοδολογίας. Μεταπτυχιακή Διπλωματική Εργασία, Τμήμα Γεωλογίας Α.Π.Θ., # σελ.

# Preface

The current thesis concerns multiple concepts of engineering seismology that are taken into account in order to perform a complete Probabilistic Seismic Hazard Assessment for the Central Ionian Islands as well as an accurate estimation of strong ground motion for the two strongest earthquakes that occurred in the region during the past few years. This study was conducted within the framework of the postgraduate studies programme "Applied and Environmental Geology" (Specialization field: "Applied Geophysics and Seismology") of the School of Geology of the Aristotle University of Thessaloniki.

In the ***first*** *chapter*, the seismotectonic characteristics of the study area are introduced along with the historical and instrumental seismicity data. In the ***second*** *chapter*, the basic principles and the methodology used for the Probabilstic Seismic Hazard Assessment are described, whereas, in the ***third*** chapter, the results are presented in terms of seismic hazard maps. The ***fourth*** *chapter* introduces a series of concepts regarding the simulation of strong ground motion. The two case studies are presented along with the simulation parameters used in the computations. The ***fifth*** *chapter* contains the broadband ground motion simulation results. A validation of the resulting simulations is attempted and then the final synthetic spectra and waveforms are provided. In the ***final*** *chapter*, the most critical conclusions are summarized. Limitations, potential implications and future perspectives are also discussed.

I would like to thank the three members of my supervisory and examination committee, Dr. Karakostas V. and Dr. Papadimitriou E. from the Aristotle University of Thessaloniki and Dr. Kaviris G. from the National and Kapodistrian University of Athens, for their mentoring and support. Their suggestions and guidelines led to the improvement of this study. I would also like to thank Dr. Akinci A., Senior Researcher at the INGV (Istituto Nazionale di Geofisica e Vulcanologia) for her valuable contribution to this study. Her insight and knowledge about the subject were vital and helped me substantially throughout this research. I wish to thank Dr. Kostas Chousianitis, Associate Researcher of the Geodynamic Institute of the National Observatory of Athens for his help regarding R-CRISIS software and the data he generously provided. Moreover, I would like to express my gratitude to my friend and colleague Christos Millas, MSc Seismologist, who was always willing to offer his help and moral support. Last but not least, I would like to express my gratitude to the PhD candidates of the Geophysics Department for their companion, advice and encouragement throughout my thesis.

# Table of contents

# Abstract

Seismic hazard analysis constitutes an indispensable component for seismologists, engineers and decision makers to reduce seismic risk and, thus, disasters, economic loss and fatalities caused by major earthquakes. The reliable assessment of seismic hazard plays a decisive role for updating and improving the seismic building code and design codes for a certain area.

The area of Greece and its surroundings exhibits the highest seismic activity in the Mediterranean and is placed among the most seismically active regions worldwide (Papazachos & Papazachou, 2003). This thesis is focused on the area of the Central Ionian Islands, the most seismically active region of Greece. The study area is characterized by the frequent occurrence of strong destructive earthquakes causing loss of human life, damage to buildings and economic losses. The evolution of technology, especially concerning the construction techniques and materials, has significantly reduced the negative effects of earthquakes during the last decades. This has been achieved by the implementation of seismic hazard assessment studies, taken into account in the building codes, during the construction of technical projects and designing protection measures.

Seismic hazard in the Central Ionian Islands is estimated using two different approaches, a probabilistic assessment and a hybrid quantitative approach for earthquake scenarios. In the first part of this Master's thesis a Probabilistic Seismic Hazard assessment is attempted using the Cornell - Mcguire method (Cornell, 1968, 1971; McGuire, 1976). In this approach, seismotectonic and geological data are combined along with an earthquake catalogue in order to delineate seismogenic zones within which earthquakes occur at rates defined by a recurrence relationship (e.g. Gutenberg - Richter) and are assumed to have the same occurrence probability at any location. The earthquake catalogue is used to extract critical seismicity parameters such as seismicity rates, b-value of the Gutenberg-Richter relationship and the expected maximum magnitude. A ground motion prediction equation (GMPE) is then assigned to each zone, combining these parameters within a probabilistic framework to obtain a single ground motion value related to a specified probability of exceedance (or non-exceedance) for a certain time period. A set of grid points covering the study area, each of them being assigned with a peak ground motion parameter, is used to illustrate the final results in terms of seismic hazard maps.

In the second part, physics-based broadband ground motion simulations are attempted for the two most recent strong earthquakes, namely the 26$^{th}$ January 2014

Kefalonia M6.1 and the 17th November 2015 Lefkas M6.5 that occurred in the study area. A hybrid approach is adopted to calculate realistic time series that can be validated by comparing the peak ground acceleration values obtained by the recorded data and also with well-known ground motion prediction equations. The low-frequency part of the synthetics is computed using a discrete wavenumber finite element method by convolving Green's functions with a kinematic slip model in the frequency domain. A stochastic finite fault model approach based on the dynamic corner frequency is applied to calculate the higher frequencies. Then, the broadband synthetic time series are generated after merging the two separate techniques by performing a weighted summation at intermediate frequencies.

# Περίληψη

Οι μελέτες σεισμικής επικινδυνότητας αποτελούν πολύτιμο εργαλείο για τους σεισμολόγους, τους μηχανικούς και την πολιτική προστασία για την ελαχιστοπίηση του σεισμικού κινδύνου δηλαδή των υλικών και οικονομικών επιπτώσεων και των απωλειών ανθρώπινων ζωών από ισχυρούς σεισμούς. Η αξιόπιστη εκτίμηση της σεισμικής επικινδυνότητας διαδραματίζει καθοριστικό ρόλο για την αναθεώρηση και τη βελτιστοποίηση των αντισεισμικών κανονισμών και των κανόνων σχεδιασμού μίας περιοχής μελέτης.

Η ευρύτερη περιοχή του Ελλαδικού χώρου χαρακτηρίζεται από τα υψηλότερα επίπεδα σεισμικής δραστηριότητας στη Μεσόγειο και κατατάσσεται στις πιο ενεργές σεισμικά περιοχές στον κόσμο (Παπαζάχος & Παπαζάχου, 2003). Η παρούσα διατριβή εστιάζει στην περιοχή των κεντρικών Ιονίων Νήσων, την πιο σεισμικά ενεργή περιοχή της Ελλάδας. Η περιοχή μελέτης χαρακτηρίζεται από ισχυρούς καταστροφικούς σεισμούς που έχουν ως αποτέλεσμα την απώλεια ανθρώπινων ζωών, βλάβες σε κτήρια και οικονιμικές ζημιές. Η διαρκής εξέλιξη της τεχολογίας, ειδικά όσον αφορά στις τεχνικές δόμησης και στα υλικά κατασκευής, έχει οδηγήσει σε αξιοσημείωτη μείωση των αρνητικών επιπτώσεων των σεισμών, κατά τις τελευταίες δεκαετίες. Αυτό έχει επιτευχθεί μέσω της εκπόνησης μελετών σεισμικής επικινδυνότητας που λαμβάνονται υπόψη κατά την κατασκευή τεχνικών έργων, κατά το σχεδιασμό της πολιτικής προστασίας και στους αντισεισμικούς κανονισμούς.

Η σεισμική επικινδυνότητα στις κεντρικές Ιόνιες Νήσους εκτιμάται εφαρμόζοντας δύο διαφορετικές προσεγγίσεις, μία πιθανολογική και μία ποσοτική υβριδική μέθοδο για σενάρια σεισμών. Στο πρώτο μέρος της παρούσας μεταπτυχιακής διατριβής επιχειρείται πιθανολογική εκτίμηση της σεισμικης επικινδυνότητας με χρήση της κλασικής μεθοδολογίας των Cornell - Mcguire (Cornell, 1968, 1971; McGuire, 1976). Σε αυτή την προσέγγιση, σεισμοτεκτονικά και γεωλογικά δεδομένα συνδυάζονται με τη χρήση ενός καταλόγου σεισμών με σκοπό τον ορισμό σεισμικών ζωνών. Εντός των ζωνών λαμβάνουν χώρα σεισμοί με ρυθμό επανάληψης που ορίζεται από μία σχέση επανενμφάνισης (π.χ. Gutenberg - Richter) και θεωρείται οτι έχουν την ίδια πιθανότητα γένεσης σε οποιοδήποτε σημείο εντός τη σεισμικής ζώνης. Ο κατάλογος σεισμών χρησιμοποιείται για τον προσδιορισμό καθοριστικής σημασίας παραμέτρων όπως των ρυθμών σεισμικότητας, των τιμών της παραμέτρου b της σχέσης Gutenberg-Richter και του μέγιστου εκτιμώμενου μεγέθους σεισμού. Στη συνέχεια, ανατίθεται μια εμπειρική σχέση πρόβλεψης της ισχυρής εδαφικής κίνησης (GMPE) σε κάθε σεισμική ζώνη και συνδυάζει τις προαναφερθείσες

παραμέτρους σε ένα πιθανολογικό πλαίσιο με αποτέλεσμα τον υπολογισμό τιμών εδαφικής κίνησης συνδεδεμένες με ορισμένη πιθανότητα υπέρβασης (ή μη υπέρβασης) σε ορισμένο χρονικό διάστημα. Χρησιμοποιείται κάναβος που καλύπτει την περιοχή μελέτης, κάθε σημείο του οποίου χαρακτηρίζεται από μία τιμή εδαφικής παραμέτρου (επιτάχυνση) με σκοπό την απεικόνιση των τελικών αποτελεσμάτων υπό τη μορφή χαρτών επικινδυνότητας.

Στο δεύτερο μέρος επιχειρείται προσομοίωση της ισχυρής εδαφικής κίνησης σε ένα ευρύ φάσμα συχνοτήτων, για τους δύο πιο πρόσφατους ισχυρούς σεισμούς (26ης Ιανουαρίου 2014 Mw6.1 & 17ης Νοεμβρίου 2015 Mw6.5) που έλαβαν χώρα στην περιοχή μελέτης. Υιοθετήθηκε μία υβριδική μέθοδος με σκοπό τον υπολογισμό ρεαλιστικών χρονοσειρών οι οποίες μπορούν να επαληθευτούν αφενός μέσω της σύγκρισης με τις διαθέσιμες σεισμικές καταγραφές και αφετέρου με εμπειρικές σχέσης πρόβλεψης της ισχυρής εδαφικής κίνησης. Το μέρος των συνθετικών χρονοσειρών που αντιστοιχεί στις χαμηλές συχνότητες (έως 2 Hz) προσομοιώθηκε μέσω της μεθόδου discrete wavenumber finite element (DWFE) η οποία πραγματοποιεί συνέλιξη συναρτήσεων Green με ένα κινηματικό μοντέλο στο πεδίο των συχνοτήτων. Αντίστοιχα για τις υψηλότερες συχνότητες χρησιμοποιήθηκε μία στοχαστική προσέγγιση πεπερασμένου ρήγματος με χρήση της δυναμικής γωνιακής συχνότητας. Τελικά, η ευρέος φάσματος χρονοσειρά δημιουργήθηκε με τη συγχώνευση των αποτελεσμάτων των δύο ξεχωριστών τεχνικών προσομοίωσης.

# List of abbreviations

| | |
|---|---|
| AHEAD | European Archive of Historical EArthquake Data |
| CMT | Centroid Moment Tensor |
| CS | Cephalonia Segment |
| DT07 | Danciu & Tselentis (2007) |
| DWFE | Discrete Wavenumber Finite Element |
| EC8 | EuroCode 8 |
| FAS | Fourier Amplitude Spectrum |
| EPPO | Earthquake Planning and Protection Organization |
| GCMT | Global Centroid Moment Tensor |
| GFT | Goodness of Fit Test |
| GMPE | Ground Motion Predictive Equations |
| GPS | Global Positioning System |
| G-R | Gutenberg - Richter |
| HF | High Frequency |
| HUSN | Hellenic Unified Seismological Network |
| ITACA | ITalian ACcelerometric Archive |
| ITSAK | Institute of Engineering Seismology & Earthquake Engineering |
| KTFZ | Kefalonia Transform Fault Zone |
| LF | Low Frequency |
| LS | Lefkas Segment |
| LSR | Least Squares Regression |
| MA02 | Margaris et al. (2002) |

| | |
|---|---|
| MA78 | Makropoulos (1978) |
| MGFT | Modified Goodness of Fit Test |
| MLE | Maximum Likelihood Estimation |
| NAT | North Anatolian Trench |
| NOA (-IG) | National Observatory of Athens (- Institute of Geodynamics) |
| PGA | Peak Ground Acceleration |
| PGD | Peak Ground Displacement |
| PGV | Peak Ground Velocity |
| PSHA | Probabilistic Seismic Hazard Assessment |
| RMS | Root Mean Square |
| R-W-C | Robson - Whitlock - Cooke |
| SHARE | Seismic Hazard Harmonization in Europe |
| SHEEC | SHARE European Earthquake Catalogue |
| SK03 | Skarlatoudis et al. (2003) |
| SZ | Seismogenic Zone |
| STF | Source Time Function |

# Chapter 1 - Introduction

## 1.1 Seismotectonic properties

Greece, as a part of the SE Mediterranean, belongs to the Alpine Europe. The complex characteristics of the broader area are due to its position in the most geologically active part of the continental margin of the Eurasian (tectonic) plate which is moving southwards and the oldest remnants of the Eastern Mediterranean oceanic plate which is the prolongation of the continental African plate. The subduction of the Eastern Mediterranean plate beneath the Eurasian occurs in an amphitheatrical way, assembling the arched shape of the Hellenic Arc. The geometry of the Arc is defined in a NW – SE general trend, starting from the Ionian islands, in Western Greece and Peloponnesus, then it bends (E-W) from Cythera to Crete and finally obtains a SW-NE direction in Dodecanese Islands till the SW coast of Minor Asia (Fig. 1.1).

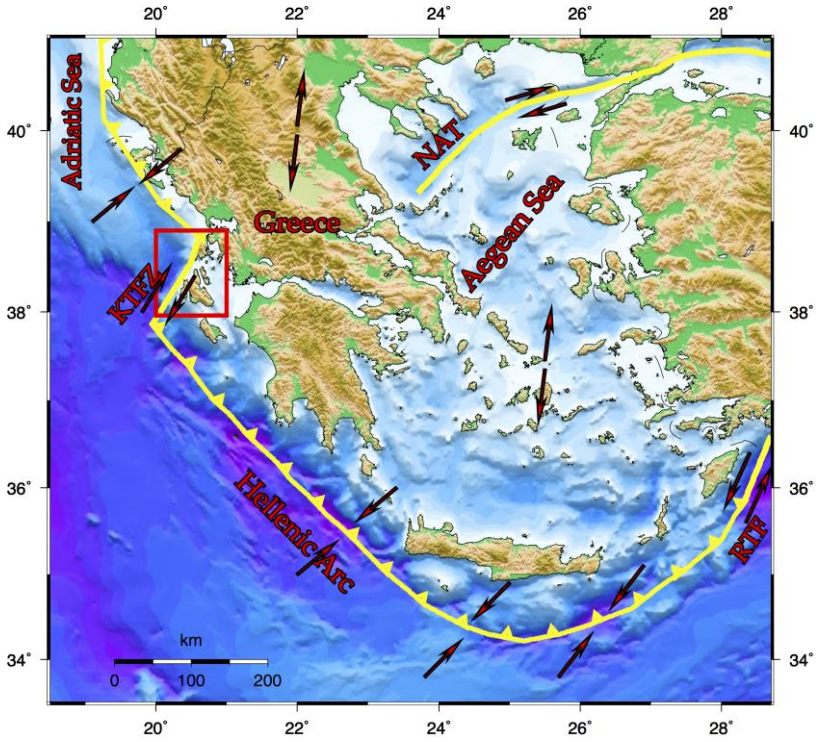


**Figure 1.1:** Main seismotectonic features dominating the Greek region. The black arrows indicate the approximate direction of relative plate motion. The study area is contained in the red rectangle. KTFZ - Kefalonia Transform Fault Zone, NAT - North Aegean Trough, RTF - Rhodes Transform Fault.

According to GPS measurements, assuming a stable African plate, the Arabic plate moves towards the North with a velocity of 10 mm/yr. The Anatolian plate is pushed to the west due to the collision between the Eurasian and the Arabic plate with a velocity of 20 mm/yr, whereas the Aegean area is moving to the SSW with a rate of 40 - 50 mm/yr (Le Pichon et al., 1995; Reilinger et al., 1997, 2000; Kahle et al., 2000). Furthermore, the internal deformation in the Central and South Aegean is determined at 2 mm/yr (Mc Clusky et al., 2000; Nyst et al., 2004) and is illustrated by the existence of major active crustal faults, as well as by the crust thinning (Hatzfeld et al., 2001). Geodetic measurements have also shown that the Anatolian plate is rotating (anticlockwise) around a pole placed north of the Sinai peninsula, in Egypt, and that the central part of the Aegean region is expanded towards SW with respect to Eurasia, at a significantly higher rate than the rate of the African's plate motion towards the North, relative to the European plate (Oral et al., 1995; Kastens et al., 1996). This expansion is terminated by the subduction of the Eastern Mediterranean plate alongside the Hellenic Trench (Jackson, 1994). The motion of the Aegean microplate has been described as a rigid rotation around an Euler pole located North of the Nile delta (Le Pichon et al., 1995).

The Ionian Islands are located at the northwestern end of the subduction zone of the last remnants of the oceanic crust of Tethys under the Aegean continental microplate, domain of the European plate along the active Hellenic Arc (Clement et al., 2000; Papadimitriou et al., 2015). The whole seismotectonic frame is supplemented by the continental collision between the Apulian and the Eurasian plate (McKenzie, 1978). These major active boundaries are connected through a major transform fault zone called the Kefalonia Transform Fault Zone (KTFZ) which is characterized by dextral strike-slip focal mechanisms, often connected with thrust components (Scordilis et al., 1985; Papadimitriou, 1988; Kiratzi & Langston, 1991; Louvari et al., 1999; Sachpazi et al., 2000).

The KTFZ consists of the Lefkas segment (LS) to the North, striking NNE – SSW and the Cephalonia segment (CS) to the South, striking NE – SW (Papazachos et al., 1998; Louvari et al., 1999). The southern segment is longer (~ 95 km) (striking = 35°), causing the strongest earthquakes in the area. Based on historical data, the maximum observed magnitude in this segment equals to M = 7.4 (Papazachos and Papazachou 2003). The northern segment that extends along the west coast of Lefkas island is approximately 35 km long and demonstrates a change of strike (~ 15°) in comparison with the other segment (Karakostas et al., 2004). Strong earthquakes have also occurred in this segment, with a maximum observed magnitude of M = 6.7 (Papazachos and Papazachou, 2003). Papazachos et al. (1998) assigned characteristic focal mechanisms for the LS, with strike = 11°, dip = 60°, rake = 165° and for the CS with strike = 33°, dip = 56°, rake = 163° (Fig. 1.2) The transition zone between these two fault segments has been interpreted as a step-over

zone consisting of smaller parallel fault segments striking WSW-ENE (Karakostas et al., 2015). The importance of this interpretation is that the rupture appears to terminate at this location and does not continue upwards to the North. In view of this, past strong earthquakes have been associated with either the LS or the CS separately (Papazachos & Papazachou, 2003). However, the two fault segments have been activated in the past synchronously as a consequence of stress transfer between them (Papadimitriou, 2002).

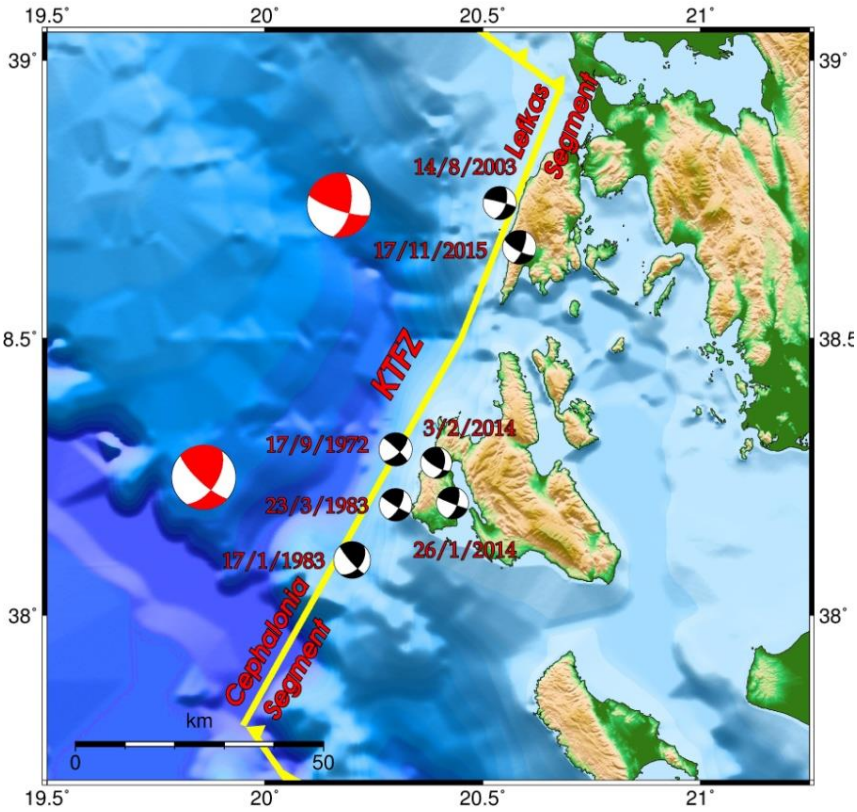


**Figure 1.2:** Major active boundaries in the study area. The subduction front to the south, the Kefalonia Transform Fault Zone (KTFZ) with the distinctive Cephalonia and Lefkada segments (CS and LS) and the collision boundary north of Lefkada Island. The black beach balls indicate the fault plane solutions of the most significant (M ≥ 6.0) earthquakes in the region. The red beach balls illustrate the characteristic focal mechanisms for the LS and CS according to Papazachos et al. (1998).

The existence of the KTFZ was initially proposed from evidence based on bathymetry (Finetti and Morreli, 1973; Stride et al., 1977; Finetti, 1982) and geological mapping (BP Co., 1971; Mercier et al., 1976; Cushing, 1985). The first seismological indications concerning the dextral strike-slip regime in the Ionian islands were published in the 1980s by Scordilis et al., (1985) and Papadimitriou (1988) based on the fault plane solutions of the strongest earthquakes and the epicentral distribution of the relocated earthquake sequences that occurred on 17 January 1983 (M = 7.0) and 23 March 1983 (M =

6.3). After further research was carried out, the presence of the strike-slip faulting style in the area was confirmed by focal mechanisms determined using moment tensor inversion (Papadimitriou P., 1988; Kiratzi and Langston, 1991; Papadimitriou E., 1993), microseismicity studies (Hatzfeld et al., 1995) and geodetic measurements (Kahle et al., 1993, 1995, 1996). Data from later microseismicity studies (Kassaras et al., 1994; Makropoulos et al., 1996) as well as GPS measurements (Cocard et al., 1999; Jenny et al., 2004 ; Hollenstein et al., 2008; Ganas et al., 2013; Boncori et al., 2015; Pérouse et al., 2016) added to the conclusion that this regime extends to the North towards the west coast of Lefkas Island.

Kahle et al. (1995) estimated the displacement of SE Greece in relation to South Italy using GPS data and concluded that the relative motion of the LS and the CS is dextral strike-slip with velocities of 10 mm/yr and 25mm/yr respectively. Peter et al. (1998) performed GPS measurements along the KTFZ and estimated that the relative motion of the LS was 10 mm/yr with respect to a stable point NW of Lefkas Island. Le Pichon et al. (1995) combined SLR (Satellite Laser Ranging) and GPS data in order to examine the relative motion of Anatolia and Aegean microplates and determined that the dextral motion of KTFZ is approximately 25 mm/yr. Coccard et al. (1999) utilized measurements over a five-year period (1993-1998) and assigned a velocity of 10 mm/yr to the LS. Later studies (Hollestein et al., 2008) highlight the broad spatial and temporal range of the velocity field in the region and determine velocities up to 30 mm/yr.

## 1.2 Seismicity of the Central Ionian Islands

### **1.2.1** Historical Seismicity

As a result of their location and complex seismotectonic characteristics, the Central Ionian Islands have suffered numerous strong and destructive earthquakes. Historical information is available for the last six centuries by catalogues of historical seismicity based on testimonials, historical sources and other recorded evidence. One of the first catalogues of historical seismicity for the study area was published by Galanopoulos (1950). In later studies (Galanopoulos, 1953, 1960, 1961) several parameters of the historical earthquakes were listed (e.g. date, time, epicentral coordinates, depth, maximum intensity). Papazachos and Papazachou (2003) have presented an earthquake catalogue with the most significant earthquakes in Greece during the period from 550 B.C. to 2001 A.C. The strongest ($M \geq 6.0$) historical earthquakes derived from this catalogue are illustrated in Figure 1.3 and listed in Table 1.1. Furthermore, another source of information concerning the historical seismicity is the seismological catalogue SHEEC

(SHARE European Earthquake Catalogue) which covers the timespan from 1000 to 1899 and contains data coming from the European archive of historical seismicity AHEAD (Archive of Historical EArthquake Data) (Stucchi et al., 2013).

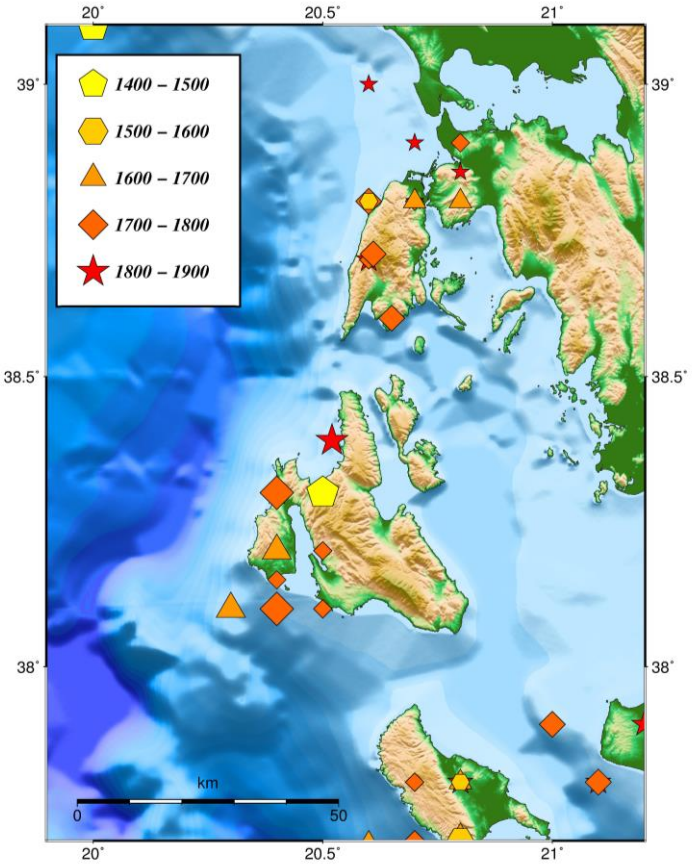


**Figure 1.3:** Locations of historical earthquakes (M ≥ 6.0) that occurred in the Central Ionian Islands since the 15th century. Epicentre locations were obtained by the catalogue of Papazachos & Papazachou, (2003).

**Table 1.1:** Historical seismicity of the Central Ionian Islands. Date (columns 1-3), epicenter coordinates (columns 4-5) and magnitudes (column 6) were obtained by Papazachos & Papazachou (2003). In the last column, moment magnitudes are listed according to SHEEC (SHARE European Earthquake Catalogue).

| Year | Month | Day | Latitude (°) | Longitude (°) | M (Papazachos & Papazachou, 2003) | Mw (Stucchi et al., 2013) |
|---|---|---|---|---|---|---|
| 1469 | - | - | 38.30 | 20.500 | 7.2 | 6.62 |
| 1577 | - | - | 38.80 | 20.600 | 6.2 | 6.23 |
| 1612 | 5 | 26 | 38.80 | 20.800 | 6.5 | 6.30 |
| 1613 | 10 | 12 | 38.80 | 20.800 | 6.4 | 6.28 |
| 1622 | 5 | 5 | 37.70 | 20.60 | 6.0 | 6.00 |

| Year | Month | Day | Latitude (°) | Longitude (°) | M (Papazachos & Papazachou, 2003) | Mw (Stucchi et al., 2013) |
|---|---|---|---|---|---|---|
| 1625 | 6 | 28 | 38.80 | 20.70 | 6.6 | 6.46 |
| 1630 | 7 | 2 | 38.80 | 20.80 | 6.7 | 6.49 |
| 1633 | 11 | 5 | 37.70 | 20.80 | 7.0 | 6.56 |
| 1636 | 9 | 30 | 38.10 | 20.30 | 7.2 | 6.62 |
| 1638 | 7 | 16 | 38.20 | 20.40 | 6.4 | 6.28 |
| 1658 | 8 | 24 | 38.20 | 20.40 | 7.0 | 6.70 |
| 1704 | 11 | 22 | 38.80 | 20.70 | 6.3 | 6.38 |
| 1714 | 8 | 7 | 38.40 | 21.70 | 6.3 | 6.28 |
| 1722 | 6 | 5 | 38.70 | 20.60 | 6.4 | 6.28 |
| 1723 | 2 | 22 | 38.00 | 20.60 | 6.7 | 6.32 |
| 1741 | 6 | 23 | 38.15 | 20.40 | 6.4 | 6.28 |
| 1759 | 6 | 13 | 38.20 | 20.50 | 6.3 | 6.26 |
| 1766 | 7 | 24 | 38.10 | 20.40 | 7.0 | 6.56 |
| 1767 | 7 | 22 | 38.30 | 20.40 | 7.2 | 6.65 |
| 1769 | 10 | 12 | 38.80 | 20.60 | 6.7 | 5.82 |
| 1783 | 3 | 23 | 38.71 | 20.60 | 6.7 | 6.64 |
| 1791 | 11 | 2 | 37.90 | 21.00 | 6.8 | 6.78 |
| 1815 | - | - | 38.80 | 20.70 | 6.3 | 6.26 |
| 1820 | 2 | 21 | 38.80 | 20.60 | 6.4 | 6.55 |
| 1825 | 1 | 19 | 38.70 | 20.60 | 6.5 | 6.71 |
| 1862 | 3 | 14 | 38.30 | 20.40 | 6.5 | 6.44 |
| 1867 | 2 | 4 | 38.39 | 20.52 | 7.4 | 7.15 |
| 1869 | 12 | 28 | 38.85 | 20.80 | 6.4 | 6.68 |

### **1.2.2** Instrumental Seismicity

It is obvious that after the installation of the first seismograph in the Greek territory, in 1899 and of the first seismometer in 1911, significant improvement in earthquake detectability was achieved. During the early 60s the first electromagnetic instruments started to operate in Athens and years later electromagnetic type photographic recording satellite stations were set up. As time passed, the network was continuingly improving following the evolution of technology. Since the beginning of 2005, a national project was launched that intended to unify the seismological networks of the Greek Institutions. Nowadays, the Hellenic Unified Seismic Network that operates since 2008 consists of stations from the seismic networks of a) the Geodynamic Institute, of the National Observatory of Athens, b) the Geophysics Department of the Aristotle

University of Thessaloniki, c) the Seismological Laboratory of the National and Kapodistrian University of Athens, d) the Seismological Laboratory of the University of Patras. The strongest earthquakes occurred during the instrumental era (with data from Papazachos & Papazachou, 2003 and the bulletins of the Seismological Station of the Aristotle University of Thessaloniki) are illustrated in Figure 1.4 and listed in Table 1.2.

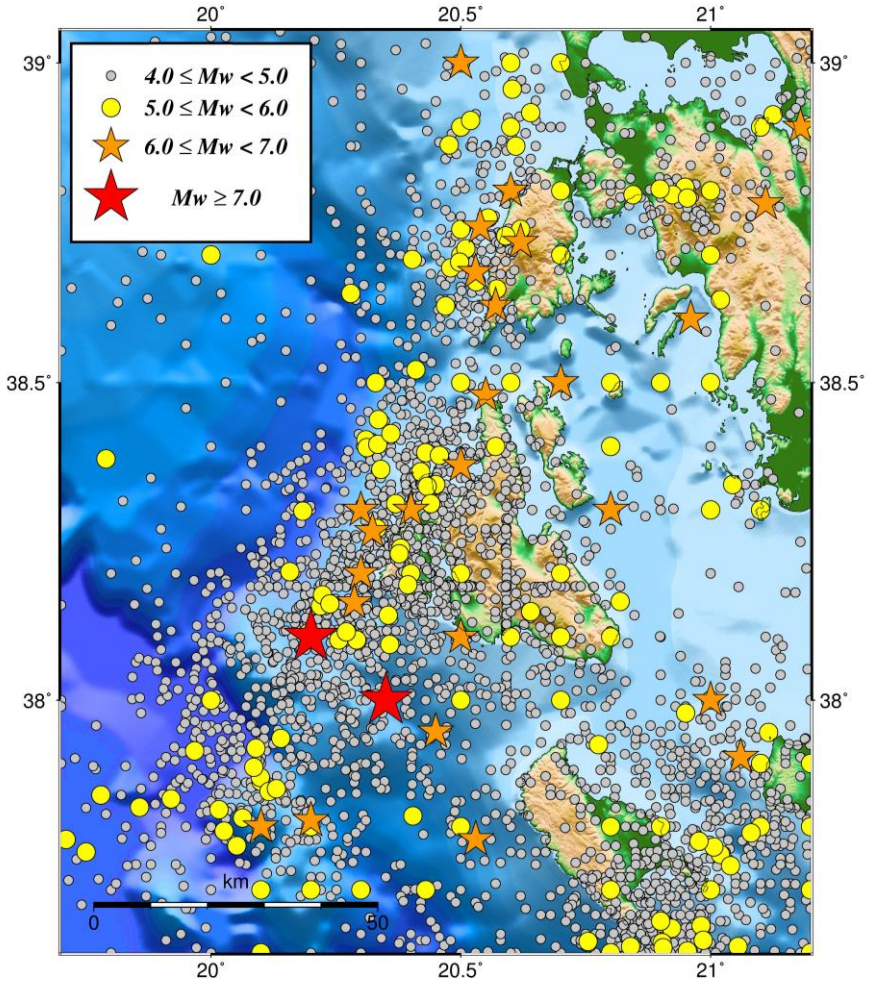


**Figure 1.4:** Locations of earthquakes with Mw ≥ 4.0 recorded in the instrumental era (1900 - 2018). Earthquake data were acquired from the homogeneous earthquake catalogue of Papazachos et al. (2010) along with data from the Hellenic Unified Seismological Network and compiled from the bulletins of the Central Seismological Station of the Geophysics Department of the Aristotle University of Thessaloniki, for the period 2010 - 2018.

**Table 1.2:** Instrumental seismicity (Mw ≥ 6.0) of the Central Ionian Islands. Date and time (columns 1-4) and epicenter coordinates (columns 5-6) were obtained by Papazachos et al. (2010) and the bulletins of the Department of Geophysics of the Aristotle University of Thessaloniki. In the last column, moment magnitudes from the updated and extended catalogue for Greece and adjacent areas (Makropoulos et al., 2012) are also listed for comparison purposes.

| Year | Month | Day | Time | Latitude (°) | Longitude (°) | Mw (AUTH) | Mw (Makropoulos et al., 2012) |
|---|---|---|---|---|---|---|---|
| 1912 | 1 | 24 | 16:22:51 | 38.100 | 20.500 | 6.8 | 6.1 |
| 1914 | 11 | 27 | 14:39:46 | 38.720 | 20.620 | 6.3 | 5.9 |
| 1915 | 1 | 27 | 1:09:56 | 38.370 | 20.500 | 6.6 | 6.1 |
| 1915 | 8 | 7 | 15:04:03 | 38.480 | 20.550 | 6.7 | 6.3 |
| 1915 | 8 | 10 | 2:02:49 | 38.500 | 20.700 | 6.1 | 6.0 |
| 1915 | 8 | 11 | 9:10:43 | 38.500 | 20.700 | 6.4 | 5.7 |
| 1948 | 4 | 22 | 10:42:45 | 38.620 | 20.570 | 6.5 | 6.5 |
| 1953 | 8 | 9 | 7:41:07 | 38.300 | 20.400 | 6.4 | 5.9 |
| 1953 | 8 | 11 | 3:32:22 | 37.950 | 20.450 | 6.8 | 6.6 |
| 1953 | 8 | 12 | 9:23:52 | 38.000 | 20.350 | 7.2 | 7.0 |
| 1953 | 8 | 12 | 12:05:21 | 38.000 | 21.000 | 6.3 | 6.1 |
| 1953 | 8 | 12 | 14:08:39 | 38.300 | 20.800 | 6.0 | 5.9 |
| 1953 | 10 | 21 | 18:39:52 | 38.600 | 20.960 | 6.3 | 6.2 |
| 1972 | 9 | 17 | 14:07:15 | 38.300 | 20.300 | 6.3 | 5.8 |
| 1983 | 1 | 17 | 12:41:31 | 38.100 | 20.200 | 7.0 | 6.7 |
| 1983 | 3 | 23 | 23:51:06 | 38.200 | 20.300 | 6.2 | 6.0 |
| 2003 | 8 | 14 | 5:14:55 | 38.744 | 20.539 | 6.2 | 5.8 |
| 2014 | 1 | 26 | 13:55:41 | 38.154 | 20.287 | 6.1 | 6.1 |
| 2014 | 2 | 3 | 3:08:44 | 38.266 | 20.323 | 6.0 | 5.7 |

# Chapter 2 - Probabilistic Seismic Hazard Assessment

## 2.1 Basic principles

Seismologists and earth scientists in general deal, for many years, with the critical challenge of clearly defining and quantifying seismic hazard given that it is the main component for risk assessment and other applications. According to the probabilistic point of view, seismic hazard (H) is defined as the occurence probability of a certain level of seismic ground motion (Y) at a site of interest in a specified time period. In a broader sense it also includes the potential for earthquake-related phenomena such as soil liquefaction, fault rupture and ground shaking. Seismic ground motion (Y) is most commonly expressed in terms of peak ground acceleration (PGA), peak ground velocity (PGV), peak ground displacement (PGD) or macroseismic intensity (I). Seismic hazard is often confused with seismic risk even though they are two fundamentally different concepts. Seismic hazard, as outlined above, describes a natural phenomenon, whilst seismic risk describes the probability of human loss and damage to the man-made and the natural environment as a result of their exposure to seismic hazard (Wang, 2009). The properties of the building infrastructure are defined by the notion of vulnerability (V) which in practical terms is the feasibility of an exposed structure to be affected by the phenomena characterizing the hazard. Accordingly, seismic risk (R) can be expressed as:

$$R = H*V \tag{2.1}$$

The convolution of seismic hazard (H) and vulnerability (V) highlights the mutual conditioning that exists between them. If there is no hazard, then nothing is exposed and vulnerable and there is nothing to be threatened if no one and nothing is exposed and vulnerable.

A probabilistic seismic hazard analysis (PSHA), as first formalized by Cornell (1968), includes the evaluation of hazard in terms of seismic ground motion at a site by taking into account all available earthquakes in the area.

A PSHA can be summarized into a five step procedure (Fig. 2.1) as listed below:

1) Identification of the seismically active regions (seismogenic zones) using all available data such as earthquake catalogues and seismotectonic properties.

2) Definition of the seismicity model for every seismic source and estimation of the seismicity rates (the rates at which earthquakes of certain magnitude are expected to

occur). Therefore, every source zone is characterized by a probability distribution of earthquakes with a magnitude equal or greater than a threshold magnitude.

3) Prediction of the seismic ground motion (Y) distribution as a function of earthquake magnitude and distance (and possibly soil and focal mechanism type), through ground motion prediction equations (GMPEs) formerly known as ground motion attenuation relationships. The ground motion is expressed as an engineering variable (PGA, PGV, PGD, I) in terms of exceedance or non-exceedance probabilities for a certain time period or the corresponding return period.

4) Aggregation of the exceedance probabilities of the different seismic sources to evaluate the impact of multiple sources at a given site.

5) Estimation of the uncertainties in earthquake magnitude, location and seismic ground motions.

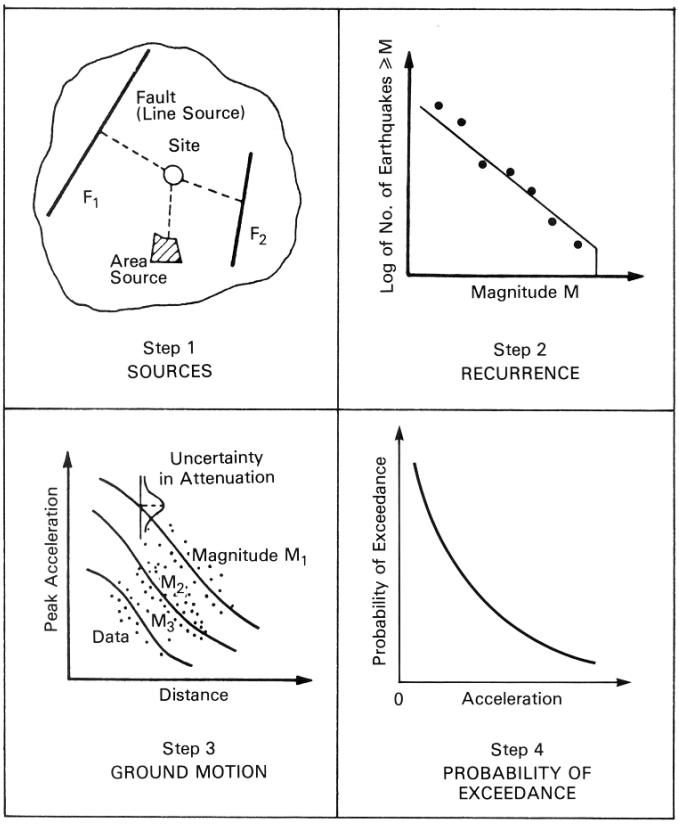


**Figure 2.1:** Basic steps of probabilistic seismic hazard analysis (after Reiter, 1990)

The seismic ground motion intensity measure (Y) at a given site varies depending on the earthquake magnitude and the distance between the earthquake source and the particular site. This intensity may be expressed by the macroseismic intensity (I) where Y = I, peak ground acceleration (A) where Y = logA, peak ground velocity (V) where Y = logV and peak ground displacement (D) where Y = logD. It has been proven that these measures follow a statistical law (eq. 2.2) similar to the Gutenberg & Richter (1944) law applied on earthquake magnitudes.

$$\log(N_t) = a_t - bY \tag{2.2}$$

where $N_t$ represents the number of earthquakes in which the ground motion intensity in the site of interest, over a period of t years, reaches values equal to or greater than Y. Constants $a_t$ and b are usually computed by the least squares method given that $\log(N_t)$ and Y are known. It is apparent that if the magnitude (M) is used instead of the other intensity measures, equation (2.2) corresponds to the Gutenberg - Richter law. Equation (2.2) is often reduced over a one-year period:

$$\log(N_1) = \alpha - bY \tag{2.3}$$

where $N_1$ is the annual number of occurrences where the ground motion intensity exceeds the value Y, at a given site. Parameter α is given by:

$$\alpha = a_t - \log(t) \tag{2.4}$$

and represents the decimal logarithm of the annual number ($N_0$) of observations which occurred at a given site and caused intensity equal to or greater than zero. The mean annual number of earthquakes producing intensity equal or greater than $Y_k$ is computed by:

$$N = 10^{(a-Y_k)} \tag{2.5}$$

which is commonly used in the following form:

$$N = N_0 \, e^{-\beta Y} \tag{2.6}$$

where $\beta = \frac{b}{\log(e)}$ and $N_0 = 10^{(a)}$

The average return period (in years) of earthquakes that caused intensity equal to or greater than $Y_k$ is given by:

$$T(Y_k) = \frac{e^{\beta Y_k}}{N_0} \tag{2.7}$$

The exceedance probability of a specific value of intensity $Y_k$ over a period of t years, having an average return period T($Y_k$) as expressed in equation (2.7), is estimated by:

$$P_t = 1 - e^{(-\frac{t}{T_k})} \quad (2.8)$$

Equation (2.8) is derived by assuming that the time distribution of earthquakes that cause intensities of a specific value over an annual period follows a Poisson distribution. Hence, the non-exceedance probability (or the probability of an earthquake source to cause an intensity lower than $Y_k$) is given by:

$$F = 1 - P_t \quad (2.9)$$

It is worth noting that if the exceedance probability of an intensity value over a period of t years is known, then the intensity $Y_t$ can be calculated by:

$$Y_t = \frac{ln(N_0 t)}{\beta} - \frac{ln\,[-ln(1-P_t)]}{\beta} \quad (2.10)$$

Accordingly, if the exceedance probability over a year is known, then it is possible from equation (2.10) to estimate the corresponding probability over any other time period as:

$$P_t = 1 - e^{t\,ln(1-P_1)} \quad (2.11)$$

## 2.2 Definition of Seismogenic Zones (SZs)

The selection of seismic source zones, since the development of the first probabilistic seismic hazard assessments (Cornell, 1968) to the most contemporary ones, is considered a critical component. SZs are described as geographic regions (polygons) that delineate areas with relatively uniform seismicity characteristics (Reiter, 1990). The maximum magnitude, depth distribution, type of faulting and activity rates for different earthquake magnitudes are among the elements considered to be uniform within a SZ. The division of the study area using seismological, seismotectonic and geological criteria, as well as the available information used to describe the characteristics of future seismicity, plays an important role. The results are highly dependent on the likelihood of agreement between the predictions of the mathematical model and the future seismicity. Direct fault modeling is considered the most appropriate approach when tectonic features and their corresponding activity rates are well documented in the study area. Adequate correlation between historical and instrumental seismicity is also a critical aspect. These conditions are not fully met for the purpose of the present study, therefore, the implementation of a detailed seismic zonation model was judged necessary.

The first effort of a global seismic zonation dates five decades ago, when Flinn and Engdahl (1965) proposed a seismic regionalization scheme based on previous work by Gutenberg and Richter (1944). This scheme and its revisions (Flinn et al., 1974; Young et al., 1996) have been used by seismologists for many years in order to identify and define seismic zones. Various researchers have suggested seismic zonation models for the Greek territory (Papazachos, 1980, 1990; Hatzidimitriou et al., 1985; Papazachos and Papaioannou, 1993; Papaioannou and Papazachos, 2000; Papaioannou, 2001; Slejko et al., 2010; Giardini et al., 2013; Vamvakaris et al., 2016). The first attempt was conducted by Papazachos (1980) using the earthquake epicentral distribution, focal mechanisms and known seismic fault data. Over the next decades, more detailed work has been accomplished, taking into account additional parameters such us geological and geomorphological data. Papaioannou and Papazachos (2000) proposed a model consisting of 67 seismic sources associated with shallow seismicity in the south Balkan area. One year later, Papaioannou (2001) created a hybrid model, consisting of both faults and shallow seismic zones that were taken into account for the revision of the Greek Building Code (2001). The following years, a new seismic zonation model was conducted by Slejko et al. (2010) in the framework of the SEAHELLARC project for the purpose of assessing seismic and tsunami hazard for the SW Peloponnese region. In 2013 the SHARE (Seismic Hazard Harmonization in Europe) project (2009-2013) provided a zonation model covering the whole European territory (Giardini et al., 2013). According to the SHARE results, 40 seismic sources correspond to the Greek territory referring both to shallow and intermediate depth seismicity. The most recent published seismic zonation model for the broader Aegean area was presented by Vamvakaris et al. (2016) and includes 113 seismic zones of shallow earthquakes. This model takes into account multiple seismicity characteristics combined with seismotectonic and neotectonic information.

In this thesis, regional seismogenic zones for the Central Ionian Islands have been defined, in order to be taken into account for the probabilistic seismic hazard calculations. It should be noted that seismic sources were determined for a more extended area than the area of interest given that they contribute to the hazard computations. The delimitation of the seismic sources was performed in compliance with the following principle. The zones must be large enough to include a certain number of earthquakes to estimate the recurrence parameters whereas, at the same time, they must be small enough to account for uniformity in the seismicity. The criteria specified towards the determination of the regional area zones were based on the updated implementation guidelines for hazard studies, according to the Seismic Hazard Analysis Committee (SSHAC, 1997). The criteria hierarchy, from the most important to the supplementary ones can be expressed as follows: *a) Type of faulting* is the primary factor of seismic source delineation. Areas connected with known tectonic features that exhibit similar

focal mechanisms are distinguished. *b) Level of seismicity*. Additionally to the focal mechanism distribution, the epicentral distribution of earthquakes is also a factor. Seismic source zones where focal mechanisms are relatively similar may demonstrate variations in their seismicity level. As a result, regions of low seismicity are separated from more active ones. *c) Other geological criteria* such as geological boundaries and bathymetry data have also been taken into account when needed. The ideal goal is to combine all available information, mentioned above, to determine seismotectonically homogeneous zones.

The characteristics of the 10 seismogenic zones that have been identified in this study are given below:

***Seismogenic zone 1:*** Corfu island region: This SZ contains almost the whole island of Corfu and a part of western continental Greece. The boundaries of the zone separate the territory between west of Corfu which is characterized by ENE-WSW shortening as a result of continental convergence, and a NNW extension to the east, close to the Pindos mountains. These observations were performed by a handful of studies (e.g. Kiratzi et al., 1987; Waters, 1994; Hatzfeld et al., 1995), geomorphological studies (King et al.,1993) and crustal deformation analysis (Papazachos & Kiratzi, 1996). The transition from the extensional inner Aegean regime to the compressional outer Aegean regime is evident from the available focal mechanisms that reveal the tectonic diversity of the area, which varies from thrust and strike-slip to normal (King et al., 1983; Doutsos et al., 1987; Hatzfeld, 1995). Focal mechanisms were the main criterion for the delineation of this SZ.

***Seismogenic zone 2:*** Lefkas segment zone: SZ2-6 contain the areas dominated by the segments of the KTFZ. The distinction in five different SZs was led by fault segments, epicentral distribution and focal mechanisms. In this regard, this SZ is elucidated by the presence of the LS of the transform fault zone, expanding from the North of Lefkas Island to the South where a transition zone emerges.

***Seismogenic zone 3:*** Step-over area: This zone includes the offshore region between Lefkas and Cephalonia. As analyzed previously (Section 1.2) it is observed that rupture appears to cease inside this area as it is evident by the lack of strong earthquakes and the overall relatively low seismicity (Fig. 2.2).

***Seismogenic zone 4:*** Cephalonia segment zone: The delineation of this zone is based on the predominant tectonic structure that affects the seismicity of the area, which is the CS of the transform fault zone. The highest seismicity of the study area is exhibited inside this region (Fig. 1.4) as it also revealed by the strong and destructive earthquakes that

have occurred during both the historical and instrumental era (Fig. 1.3). Other smaller faults parallel to the main tectonic structure may also contribute to the seismic hazard of the area (Papazachos, 1996).

***Seismogenic zone 5:*** Prolongation of KTFZ to the SW: Inside this region, high levels of seismicity are observed, revealing a strike-slip regime similar to SZ4 with few thrust focal mechanisms being also present. This SZ is differentiated from the CS zone in order to represent two different portions of the KTFZ which have been proven to be activated separately, despite having cole interconnection. The bottom boundaries were set to distinguish this SZ from the zones to the South (SZ9-10) which exhibit thrust faulting.

***Seismogenic zone 6:*** Ithaca and adjacent areas: This SZ is characterized by low to moderate seismicity, mainly connected to the Ionian thrust.

***Seismogenic zone 7:*** Western Central Greece region: This SZ represents the transition from the transform faulting style that dominates the KTFZ region to the extensional stress regime which characterizes Central Greece via the existence of numerous normal faults.

***Seismogenic zone 8:*** Northwestern Peloponnese area: The separation of this SZ is justified by the presence of characteristic dextral strike-slip focal mechanisms, mostly with a NE-SW direction, in the region south of Patras Gulf and north of the Kyparissiakos Gulf. A characteristic example is the Andravida - Patras earthquake sequence in 2008 (Kapetanidis et al., 2008; Kaviris et al., 2010). This faulting pattern is therefore differentiated from a) the normal faults dominating the Corinth Gulf, expressing a uniform extension stress field (e.g. Kapetanidis et al., 2015; Mesimeri et al., 2016, 2018; Kaviris et al., 2017, 2018) and b) the N-S normal faulting observed further to the South. Inside this SZ a relatively aseismic area can be recognized at the southern part of Patras Gulf (Ferentinos et al., 1985).

***Seismogenic zone 9:*** Zante Island region: Zante island and its close surroundings are included in this zone. The delimitation of this SZ is due to the transition from strike-slip faulting (that dominates Cephalonia Island) to thrusting, manifested by the epicentral distribution and fault plane solutions (Kiratzi & Louvari, 2003; Kokinou et al., 2006). Despite the fact that thrust faulting is dominant at Zante Island, strike-slip components are also present in certain fault plane solutions.

***Seismogenic zone 10:*** *Western Hellenic Arc: This* SZ contains the offshore area south of Zante Island, approaching the Hellenic Arc front. This region is characterized by higher seismicity compared to SZ9 and by a more uniform focal mechanism type which exhibits pure thrust regime. In particular, the focal mechanism distribution unveils the activation of parallel low angle thrust faults, striking NW-SE and dipping to the NE (Papazachos, 1996).

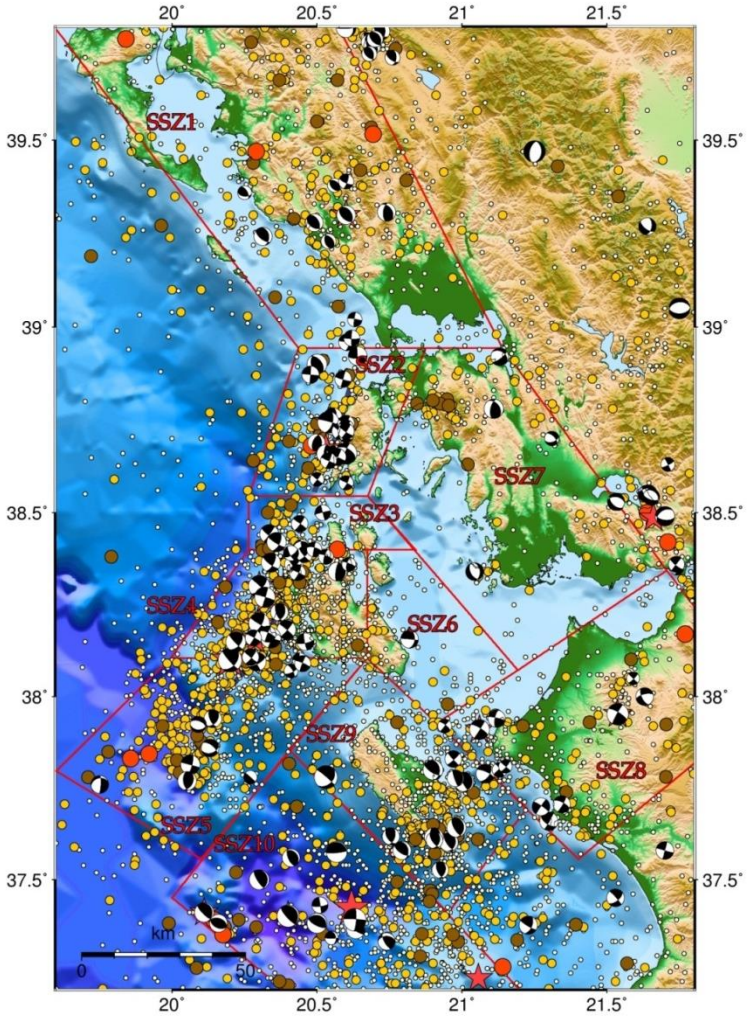


**Figure 2.2:** Map of the study area, with the 10 suggested seismogenic zones determined by the combined use of all available data.

## 2.3 Earthquake catalogue

One of the key elements in PSHA studies is the earthquake catalogue. The catalogue must be as complete and as accurate as possible. However, this may be challenging due to the heterogeneous history of earthquake reporting and magnitude estimation. Both random and systematic errors jeopardize the homogeneity of earthquake catalogues. The first ones are due to the human factor (e.g. picking the arrival times, the condition of the seismological network), whereas the second ones are related with modeling uncertainties (e.g. the adopted velocity model, the earthquake location process) (Habermann, 1987; Husen & Hardebeck, 2011).

It is obvious that the assessment of completeness is a very important process, especially for the preinstrumental part of the catalogue where gaps in the dataset are more likely to exist. There are various approaches concerning the determination of the completeness magnitude ($M_c$) but they can be summarized in two major classes: The catalogue-based methods and the network-based methods (Mignan et al., 2012). The (catalogue-based) method applied in the present thesis is a version of the Goodness-of-Fit (GFT) method (Wiemer and Wyss, 2000) modified by Leptokaropoulos et al. (2013). The GFT method follows the assumption of a Gutenber-Richter (G-R) power law magnitude distribution. The difference between the observed frequency-magnitude distribution and a synthetic distribution is computed in order to evaluate the goodness of fit between them. The a and b values of the G-R law are computed using the maximum likelihood estimation (MLE) technique along with their confidence limits. After that, a synthetic distribution of magnitudes is computed, having the same a, b and Mi (minimum magnitude) values, which represents a perfect fit to a power law. The normalized absolute difference (R) between the cumulative number of observed ($N_{obs}$) and synthetic ($N_{syn}$) events in each magnitude bin is computed by the formula:

$$R = 100 - \left( \frac{\sum_{Mi}^{Mmax} |Nobs - Nsyn|}{\sum_i Nobs} 100 \right) \quad (2.12)$$

The GFT value R interprets the level at which the observed data are simulated by the power law (Woessner and Wiemer, 2005). The satisfying level of agreement is predefined by the user and usually equals to 90% or 95%.

The modified approach (MGFT) of this method (Leptokaropoulos et al., 2013) relies on the creation of synthetic datasets of events by distributing random numbers following the G-R law. A specific number of iterations ($N_i$) of this process results in the creation of Ni synthetic catalogues. These catalogues have only one free parameter, the earthquake magnitude, given that the spatial and temporal parameters are not relevant in this

procedure. Instead of computing the absolute difference between the observations and the synthetic values (as in the GFT method), $N_i$ synthetic catalogues consisting of random events with the same number of data and magnitude distribution are created for the corresponding magnitude bins, each of them having its own occurrence frequency. Then, the parameters a and b of the G-R law are calculated (MLE) for all bins starting from the minimum magnitude Mi. The difference between the synthetic and the observed datasets are calculated by the equation (2.12) producing an average value of differences. The same procedure is employed with Mi+1 as the minimum magnitude and a new G-R law fit with newly computed a and b values. Finally, the mean values of the differences between the frequency-magnitude distribution of the real catalogue and the synthetic one for each magnitude bin are computed and mapped.

A homogeneous earthquake catalogue for the period 550 BC - 2010 was used in this thesis (Papazachos et al., 2000; 2010) along with data from the Hellenic Unified Seismological Network and compiled from the bulletins of the Geophysics Department of the Aristotle University of Thessaloniki, for the period 2010 - 2018. The catalogue for the period 2010-2018 has been compiled using the bulletins of the Department of Geophysics of the Aristotle Uiversity of Thessaloniki and the Geodynamic Institute of the National Observatory of Athens. The catalogue for the period 550BC - 2010 is considered complete for shallow earthquakes for the following periods and magnitudes: $M \geq 4.5$ since 1970, $M \geq 5.0$ since 1950, $M \geq 5.2$ since 1911, $M \geq 6.5$ since 1845 and $M \geq 7.2$ since 1500 (Papazachos and Papazachou, 2003).

An integrated and homogeneous catalogue of earthquakes for the period 1900 - 2018 was compiled in order to accurately calculate the seismicity parameters of the study area. The aggregated results of the completeness analysis of the catalogue per seismogenic zone are presented in Table 2.1. The completeness magnitude ($M_c$) for each wider delineated region is presented, along with the corresponding Mc for the recent instrumental period, which coincides with the operation of the HUSN. In some cases (e.g. SZ1), the 95% level of fit cannot be achieved possibly due to the relatively low sample size of the dataset and the insufficient azimuthal coverage of the area by the seismological network.

A common (often considered necessary) procedure in PSHA is the declustering of the earthquake catalogue, meaning the separation of the dependent events from the background seismicity (Reasenberg, 1985). All instrumental catalogs include seismic sequences, i.e. not only the mainshocks but also their foreshocks and aftershocks. Seismicity models most commonly assume a Poissonian model of earthquake occurrence. It has been recognized in many applications that foreshocks and aftershocks show a minor or major deviation from the Poisson process, thus several methods have been

suggested in order to separate the background seismicity from the raw earthquake data. Most commonly, the methods proposed by Gardner & Knopoff, (1974) and Reasenberg (1985) and their variants are used because they are relatively simple to apply. The main difference among each declustering methodology concerns the selection of the size of the applied spatial and temporal windows.

However, recent studies suggest the use of the full catalog in seismic hazard assessment, identifying that in cases where a declustered catalogue is used the computed seismicity rates lead to significantly underestimated exceedance probabilities. The latter leads, subsequently, to the underestimation of risk derived from the created seismic hazard maps compared with the observed ground motion (e.g. Boyd, 2012; Iervolino et al., 2012; Marzocchi & Taroni., 2014). Taking into consideration the properties of the catalogue used in this thesis, the use of the complete earthquake catalogue was deemed appropriate.

## 2.4 Evaluation of Seismicity Parameters

### **2.4.1** Earthquake recurrence

In order to estimate the recurrence model of each SZ the seismicity is fitted to a Gutenberg-Richter (1944) model. The recurrence rate given by this model is: $\log N = a - bM$, where N is the cumulative number of earthquakes with magnitudes larger than or equal to M over a one year period and constants a, b are the seismicity parameters of the region that describe the activity rate and the relative number of small-to-large earthquakes, respectively (Wiemer & Wyss, 1997).

The computation of the seismicity parameters is crucial in the context of a PSHA, given that they signify the background seismicity and the magnitude size distribution for a study area. The parameter b should not be considered stable in an earthquake catalogue (Marzocchi & Sandri, 2003). It has been scientifically proved that b-values in Greece do not show high deviations between areas with a similar tectonic regime (Kassaras & Kaviris, 2016) but despite this interconnection, the computed values may vary due to the sensitivity, the quality and the variability of the seismological data used for the calculations (Papazachos, 1974). Furthermore, it has been reported that for certain earthquake sequences, the b-value changes before and/or after the main shock and its variations have been investigated as a potential earthquake precursor. It has been observed that b-value increases before the occurrence of large earthquakes, succeeded by a decrease in value afterwards (e.g. Robinson, 1979; Smith, 1981, 1986). Adding to this, in

some circumstances an increase way before the earthquake took place was observed, followed by a slight drop before its occurrence and a significant decline afterwards (e.g. Gupta & Singh, 1989; Sahu & Saikia, 1994; Gupta et al., 1995). Finally, the phenomenon of a b-value decrease before the occurrence of a large earthquake followed by an increase in b-value after the main shock has also been reported (e.g. Scholz, 1968; Wiemer & Wyss, 1997; Wyss & Stefansson, 2006). Regarding the a-values, they depend on the timespan of seismological data, the level of seismicity and the extent of the study area. In general, the higher the a-value estimated, the higher is the seismicity of the area, referring to the same period of time.

The most common methods used in the literature for estimating the parameters a and b are the standard least squares regression (LSR) and the maximum likelihood estimation (MLE) technique (Aki, 1965; Utsu, 1999). MLE is considered the most preferred method, as the higher weight is placed on the more numerous smaller earthquakes (Aki, 1965). On the other hand, the LSR method appears to be more sensitive to the presence of the largest earthquakes in the catalogue, which have higher errors and often are statistical outliers. In cases where the earthquake data produce well behaved log-linear magnitude-frequency distributions, the two methods yield similar results.

According to Aki (1965), the b-value is estimated by the formula:

$$b = \frac{1}{ln[<M> - (Mc - \frac{\Delta M}{2})]} \qquad (2.13)$$

where <M> is the sample mean of the events, Mc is the completeness magnitude and ΔM is the binning width of the catalogue.

The b-value accuracy is estimated by:

$$\sigma_b = \frac{b}{\sqrt{N}} \qquad (2.14)$$

where N is the sample size. The computation of the b-values for each SZ resulted in relatively unstable results, such as strong variations between neighboring zones and unrealistically high values. The latter is caused by the limited data and the narrow magnitude range inside the regional SZs. Consequently, an alternative approach was followed with the b-values computed for larger areas having similar characteristics, e.g. the SZs belonging to the KTFZ (Fig.2.3). On the other hand, the a-values, that describe seismic activity, were computed for each individual SZ.

In the present thesis both methods (LSR and MLE) were applied but no significant differences were found (Table 2.2). The range of variation for the obtained b-values is

coherent with the typical values found in other studies (Papaioannou & Papazachos, 2000; Vamvakaris et al., 2016). The only region which demonstrates an increased deviation from previous assessments is the broader Zante Island region which corresponds to the SZs 9-10. This can be partly explained by the occurrence of the recent strong 26 October 2018 ($M_w$ = 6.8) earthquake and its aftershock sequence that is included only in the present assessment.

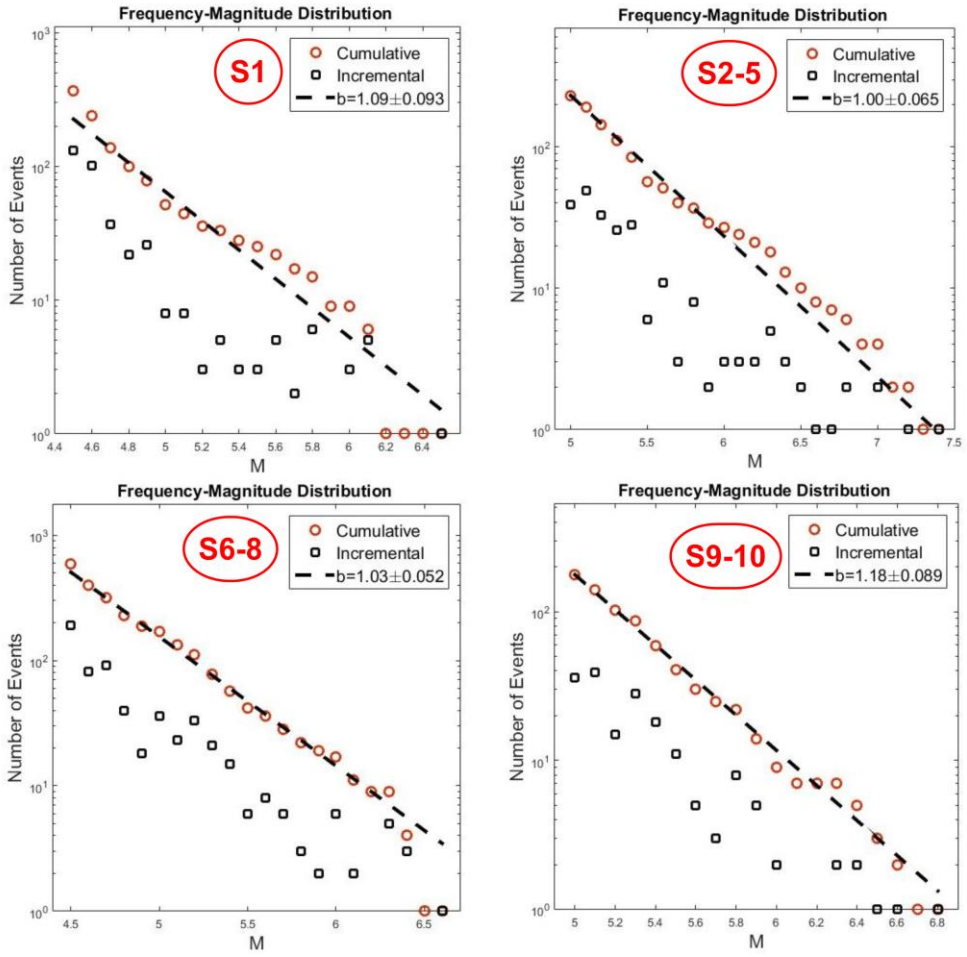


**Figure 2.3:** Frequency - magnitude distributions for the selected regions (S1, S2-5, S6-8, S9-10) using the compiled earthquake catalogue for the period 1900 - 2018, applying the Goodness-of-Fit (GFT) method modified by Leptokaropoulos et al. (2013). Incremental (squares) and cumulative (circles) number of earthquakes per magnitude bin are shown along with the best fitting line (dashed line) as derived from the MGFT for the desired time interval.

**Table 2.1:** Results of the completeness analysis.

| | 1975 - 2018 | | | | 2008 - 2018 | | | |
|---|---|---|---|---|---|---|---|---|
| | MGFT | Level of Fit | GFT | Level of Fit | MGFT | Level of Fit | GFT | Level of Fit |
| SZ1 | 4.7 | 85.3 % | - | 90% | 2.9 | 84.3 % | 2.9 | 95% |
| SZ2-5 | 4.6 | 90.6 % | 4.6 | | 3.0 | 96.8 % | 2.8 | |
| SZ6-8 | 4.6 | 92.7 % | 4.5 | | 2.7 | 96.6 % | 2.6 | |
| SZ9-10 | 4.5 | 95.6 % | 4.5 | | 3.1 | 93.8 % | 3.1 | |

### **2.4.2** Maximum Magnitude ($M_{max}^{exp}$, $M_{max}^{obs}$)

The maximum magnitude defines the upper limit used in the seismic hazard assessment, thus representing the maximum expected magnitude in each SZ. Historical earthquake catalogues represent only a small part of the whole seismic history, even in areas of high seismicity. Therefore, $M_{max}^{exp}$ must be estimated indirectly (Wheeler, 2009a,b). Despite the fact that the $M_{max}^{exp}$ value is required in a PSHA framework, little work has been done in developing appropriate techniques for estimating this parameter. Currently, there is no universally accepted technique for estimating $M_{max}$. However, the current procedures for the $M_{max}^{exp}$ estimation can be divided into two main categories: deterministic and probabilistic.

The deterministic methods are based on the empirical regression relationships between the earthquake magnitude and fault parameters such as fault length, area and dislocation (Wells and Coppersmith, 1994; Papazachos et al., 2004). The probabilistic approaches to estimate $M_{max}$ are based on statistical techniques. The choice of the most appropriate technique depends on the assumption concerning the statistical distribution model (e.g. Poisson distribution) and the available information on past seismicity (Kijko et al., 2011). All available statistical procedures have their limitations, strengths and weaknesses. In general, statistical methods tend to provide underestimated $M_{max}^{exp}$ values, especially when the seismological data are incomplete or in areas of low seismicity (Kijko et al., 2011).

In this thesis, $M_{max}^{exp}$ was estimated using the Robson - Whitlock - Cooke (R-W-C) procedure (Robson & Whitlock, 1964; Cooke, 1979; Kijko & Singh, 2011). According to the R-W-C procedure, if the magnitudes of the earthquakes in a SZ are arranged in ascending order ($m_1 \leq m_2 \leq .... \leq m_{n-1} \leq m_{max}^{obs}$), $M_{max}^{exp}$ is computed by the equation:

$$M_{max}^{exp} = m_{max}^{obs} + 0.5(m_{max}^{obs} - m_{n-1}) \quad (2.15)$$

with its variance:

$$\sigma M_{max}^{exp} = 0.5\ [3\sigma_M^2 + 0.5\ (m_{max}^{obs} - m_{n-1})^2] \quad (2.16)$$

**Table 2.2:** Values of the seismitity parameters (a1, b $\pm\ \boldsymbol{\sigma b}$) of the identified SZs estimated with the MLE (maximum likelihood estimation) and LSR (least squares regression) methods. The $\mathbf{M_{max}^{obs}}$ (maximum observed magnitude) and the $\mathbf{M_{max}^{exp}}$ (maximum ezpected magnitude) following the R-W-C procedure are also reported.

| | | MLE | | | LSR | | | $M_{max}^{obs}$ | R - W - C |
|---|---|---|---|---|---|---|---|---|---|
| **Zone** | **Region** | **b** | **σb** | **a1** | **b** | **σb** | **a1** | | $M_{max}^{exp}$ |
| SZ1 | Corfu Island | 1.09 | 0.09 | 4.48 | 1.01 | 0.05 | 4.06 | 6.5 | 6.7 |
| SZ2 | LS | 1.00 | 0.07 | 3.99 | 0.97 | 0.02 | 3.85 | 6.5 | 6.6 |
| SZ3 | Step-over zone | | | 3.69 | | | 3.56 | 6.1 | 6.3 |
| SZ4 | CS | | | 4.15 | | | 4.00 | 7.4 | 7.6 |
| SZ5 | CS extension to SW | | | 4.28 | | | 4.13 | 7.2 | 7.3 |
| SZ6 | Ithaca and adjacent areas | 1.03 | 0.05 | 4.09 | 1.09 | 0.03 | 4.91 | 6.4 | 6.5 |
| SZ7 | Western Central Greece | | | 3.99 | | | 4.77 | 6.3 | 6.5 |
| SZ8 | NW Peloponnese | | | 4.13 | | | 4.94 | 6.6 | 6.7 |
| SZ9 | Zante Island | 1.18 | 0.09 | 4.97 | 1.23 | 0.12 | 5.24 | 6.5 | 6.8 |
| SZ10 | South of Zante Island | | | 5.22 | | | 5.50 | 6.8 | 6.9 |

## 2.5 Selection of Ground-Motion Prediction Equations

Ground Motion Prediction Equations (GMPEs), previously referred to as attenuation relations, are probabilistic relations between earthquake source parameters (e.g. the moment magnitude), source-to-site distances, types of local site condition and focal mechanisms. In other words, GMPEs are statistical models used to predict the ground shaking in terms of ground motion parameters such as peak ground acceleration, velocity and displacement. GMPEs are a necessary tool for engineering seismology and earthquake engineering and are widely used to assess seismic hazard in terms of the loading that a structure may undergo during a future earthquake.

The general procedure used in developing any GMPE is the regression analysis of the ground motion recordings either from strong ground motion recordings of past events (optimal) or from stochastic simulations (Bajaj et al., 2017). GMPEs may have a variety of functional forms but their majority can be described by the following general form:

$$\log(A,V,D) = f(M,\ldots) + g(X,\ldots) + c + \delta \qquad (2.17)$$

where f(M,...) contains the terms related to the seismic source such as the earthquake magnitude, the focal depth and the faulting style, g(X,...) includes the path effects, and c and δ are terms accounting for the local site condition in the interest area. A,V,D are ground acceleration, ground velocity and ground displacement, respectively.

There are now a handful of GMPEs that have been developed to estimate ground motion parameters from Greek earthquakes (table 2.3):

**Table 2.3:** GMPEs proposed for shallow earthquakes in Greece. A,V,D are the ground motion parameters, R is the epicentral or hypocentral distance, S represents the site condition term, F is related to the faulting type.

| **Ground Motion Prediction Equations** | **Limitations** | **Published by** |
|---|---|---|
| $A = 2164e^{0,7M}(R + 20)^{-1,8}$ | 5.0 ≤ M ≤ 7.5<br>10 km ≤ R ≤ 120 km | Makropoulos (1978)<br>Makropoulos & Burton (1985) |
| $Loga = -1.101 + 0.2615M - logR - 0.00255R$ | | Ambraseys (1991) |
| $Loga = 1.77 + 0.49M - 1.65log(R + 15)$<br>$Logv = -0.39 + 0.61M - 1.62log(R + 10)$ | 4.5 ≤ M ≤ 7.0 | Theodoulidis (1991) |
| $lnPGA = 4.37 + 1.02Ms - 1.65ln(R + 15) + 0.31S \pm 0.66$<br>$lnPGV = -0.18 + 1.29Ms - 1.62ln(R + 10) - 0.22S \pm 0.73$<br>$lnPGD = -4.05 + 1.74Ms - 1.85ln(R + 5) - 0.98S \pm 1.19$ | 4.5 ≤ M ≤ 7.0 | Theodoulidis & Papazachos (1992) |
| $lnPGA = 4.16 + 0.69Mw - 1.24ln(R + 6) + 0.12S + 0.70$<br>$lnPGV = -1.51 + 1.11Mw - 1.20ln(R + 5) + 0.29S + 0.80$<br>$lnPGD = -6.63 + 1.66Mw - 1.34ln(R + 5) + 0.50S + 1.08$ | 4.5 ≤ M ≤ 7.0<br>5 km ≤ R ≤ 120 km | Margaris et al. (2002) |
| $logPGA = 1.07 + 0.45Mw - 1.35log(R + 6) + 0.09F + 0.06S \pm 0.286$ | 4.5 ≤ M ≤ 7.0<br>1 km ≤ R ≤ 160 km | Skarlatoudis et al. (2003) |
| $logPGA = 0.883 + 0.458M - 1.278log_{10}\sqrt{R^2 + 11.515^2} + 0.116F$ | 4.5 ≤ M ≤ 7.0<br>1 km ≤ R ≤ 136 km | Danciu & Tselentis (2007) |

| | | |
|---|---|---|
| $\log_{10}(PGA, PGV) = \alpha + bM + cM^2 + (d + eM)$ $\log_{10}\sqrt{R^2 + (H-h)^2} + f_1\ RS + f_2 SS + e_1 + e_2 SF_s + a_{log10}$(PGA, PGV) | 4.5 < M < 6.6 R ≤ 150 km | Segou & Voulgaris (2013) |
| $logy = a + bM + clog\sqrt{R^2 + h^2} + d\sqrt{R^2 + h^2} + S + F$ | R ≥ 5 km | Chousianitis et al. (2018) |

## 2.6 R-CRISIS software

The probabilistic seismic hazard calculations for the present thesis were performed using the R-CRISIS software, in its latest version (2018). The first version of the program was launched in 1986 but since then, several modifications and updates have been included. It was originally developed in FORTRAN programming language (Ordaz, 1991) without a graphic user interface (GUI) which was introduced later (Ordaz, 1999) in CRISIS99. In 2007, the software was upgraded taking advantage of the possibilities offered by the object-oriented technologies (CRISIS2007). The most recent version of the software (Ordaz et al., 2018) is the result of the work of experts coming from different backgrounds related to the PSHA framework (R-CRISIS). The implemented models and methodologies in R-CRISIS are briefly presented below:

The probabilistic framework employed by R-CRISIS follows the approach initially proposed by Cornell (1968) and improved by Esteva (1970). The study area is divided into seismic sources and an independent earthquake-occurrence model is assigned to each of them along with a ground motion model. Then, the earthquake occurrence probabilities are estimated by means of statistical analysis.

The seismic hazard produced at a single point source (the $k^{th}$ source) by an earthquake of magnitude Mi for the next Tj years is computed by the equation:

$$P\ (A \geq \alpha \mid M_i, T_j, k) = 1 - \sum_{s=0}^{Ns} P_k\left(s, M_i, T_j\right)[1 - P(A \geq a \mid M_i, R_k)]^s \qquad (2.18)$$

where $P(A \geq a \mid M_i, R_k)$ is the exceedance probability of the intensity parameter α, caused by an earthquake of magnitude $M_i$, occurred at a source k, at a distance $R_k$ from the site of interest. This probability depends only on the magnitude (M) and the source-to-site distance (R) and its computation is performed through the use of GMPEs.

Seismic hazard, as expressed in equation (2.18) is preferably described in terms of non-exceedance probabilities, as follows:

$$P\ (A \le \alpha \mid M_i, T_j, k) = 1 - \sum_{s=0}^{Ns} P_k\ (s, M_i, T_j)[P(A \ge a \mid M_i, R_k)]^s \quad (2.19)$$

Equation (2.19) provides the non-exceedance probability of the intensity parameter α assuming that only earthquakes of magnitude $M_i$ occurred. The non-exceedance probability of α, corresponding to the occurrence of earthquakes of all magnitudes at source k during the next Tj years is computed by:

$$P\ (A \le \alpha \mid T_j, k) = \prod_{i=1}^{Nm} P\ (A\ \le \alpha \mid M_i, T_j, k) \quad (2.20)$$

where $N_m$ is the number of magnitude bins of the discretized independent earthquakes. Spatial integration has to be performed in order to account for all possible focal locations. Assuming that the spatial integration process produces N sources and the earthquake occurrences at the discrete sources are independent from each other, then the non-exceedance probability of the intensity parameter α during the next $T_j$ years, caused by earthquakes of all magnitude bins, can be computed by the following equation:

$$P\ (A \le \alpha \mid T_j) = \prod_{k=1}^{N} P\ (A\ \le \alpha \mid T_j, k) \quad (2.21)$$

$$P\ (A \le \alpha \mid T_j) = \prod_{k=1}^{N} \prod_{i=1}^{Nm} P\ (A\ \le \alpha \mid M_i, T_j, k) \quad (2.22)$$

$$P\ (A \le \alpha \mid T_j) = \prod_{k=1}^{N} \prod_{i=1}^{Nm} \sum_{s=0}^{Ns} Pk(s, M_i, T_j)[P\ (A \le \alpha \mid M_i, R_k)]^s \quad (2.23)$$

which finally leads to the following equation:

$$P\ (A \le \alpha \mid T_j) = 1 - \prod_{k=1}^{N} \prod_{i=1}^{Nm} \sum_{s=0}^{Ns} Pk(s, M_i, T_j)[P\ (A \le \alpha \mid M_i, R_k)]^s \quad (2.24)$$

Eventually, equation (2.24) is employed by R-CRISIS in order to compute seismic hazard in cases where the seismic sources are spatially distributed (k = 1,2,…,N), earthquakes of various magnitudes ($M_i$, i = 1,2,…,N) occur and the earthquake occurrence probabilities in known time frames $T_j$, at k sources are defined by the probability $P_k$ (s, $M_i$, $T_j$) of having s events of magnitude $M_i$ during the next $T_j$ years taking place at source k. This is a general description of seismicity that can possibly be provided.

In order to provide a definition of seismicity of an area, three different types of seismicity models can be used in R-CRISIS. Two of them are related to Poissonian occurrences (Modified Gutenberg-Richter model and the Characteristic earthquake model), whereas the third is a generalized non-Poissonian model where the probabilities are provided by the user as an input to the program. In this thesis, the modified Gutenberg-Richter model was used in the calculations, given that there is no evidence for the Characteristic earthquake model based on reliable instrumental seismic data at the

Central Ionian Islands. According to this model the exceedance probability Pe(α,T | M,R) of the intensity parameter α in the next T years, considering an earthquake with magnitude M that occurred at a distance R from the site, is given by:

$$Pe(\alpha,T \mid M,R) = 1 - \exp[-\Delta\lambda(M)T \cdot p_1(\alpha \mid M, R)] \quad (2.25)$$

where Δλ(M) is the Poissonian magnitude exceedance rate associated to the magnitude bin that includes magnitude M. Δλ(M) is generally expressed as in equation (2.26) and for the modified Gutenberg-Richter model in particular, equation (2.27) is utilized.

$$\Delta\lambda(M) = \lambda\left(\frac{M-\Delta M}{2}\right) - \lambda\left(\frac{M+\Delta M}{2}\right) \quad (2.26)$$

$$\lambda(M) = \lambda_o \frac{\exp(-\beta M) - \exp(-\beta M_u)}{\exp(-\beta M_o) - \exp(-\beta M_u)},\ M_o \le M \le M_u \quad (2.27)$$

where $\lambda_o$ is the exceedance rate of the threshold magnitude $M_o$, β is the b-value corresponding to the seismic source given in terms of its natural logarithm and $M_u$ is the maximum magnitude associated with the seismic source.

The seismic sources can be described by various geometry models with different characteristics. The geometry models available in R-CRISIS are a) area sources, when the sources are modeled as polygons defined by the coordinates of their vertexes, b) line sources, when the active sources are simulated as lines (faults) defined by the coordinates of their vertexes, c) point sources, when a collection of (individual) point sources is implemented, with each point being a potential earthquake hypocenter, and d) gridded sources, when the sources are modeled by a collection of point sources located at the nodes of a rectangular grid, parallel to the earth's surface. Each node is then considered as a potential earthquake hypocenter. The combination of multiple geometry models for different sources within the same hazard analysis is possible in the program. In the current study, area sources were delineated to overcome the lack of correlation between earthquakes and known geological structures in the region.

R-CRISIS allows the use of four site-to-source distance types (Fig. 2.4). These are a) the focal distance, b) the epicentral distance, c) the Joyner and Boore distance (closest distance to the projection of the fault plane on the earth's surface) and d) the closest distance to the rupture area. The selection of the type of site-to-source distance in a PSHA project depends mainly on the ground motion prediction equation (GMPE) used. In the present study, the epicentral distance was used as the site-to-source distance type, given that it is employed by all widely used GMPEs derived from purely Greek data.

As previously mentioned, GMPEs combine earthquake characteristics, intensity measures and distances at the computation sites through probabilistic relations. R-CRISIS utilizes four different types of GMPEs: a) *built-in GMPE tables*, coming from a large set of popular models verified and published in the literature. Many of them require the specification of additional parameters, such as the style of faulting and soil type, by the user, b) *GMPE tables*, which are user-prepared attenuation tables that have a specific structure and can be inserted to the program, c) *generalized models*. The difference between these models and the previous types is that they are not explicit functions of magnitude and distance. Each of the events considered in the analysis is interpreted through a collection of probabilistic footprints. Each footprint then extracts, in probabilistic way, the geographical distribution of the computed intensity parameters. The utilization of such models comes in handy in circumstances when the relevant earthquakes are few but clearly identified for example in local studies, and d) *hybrid models,* described as the combination of two or more distributions with different mean values and standard deviations (Scherbaum et al., 2005). Such models are most commonly used when the normal distribution does not seem to fit well with the earthquake data.

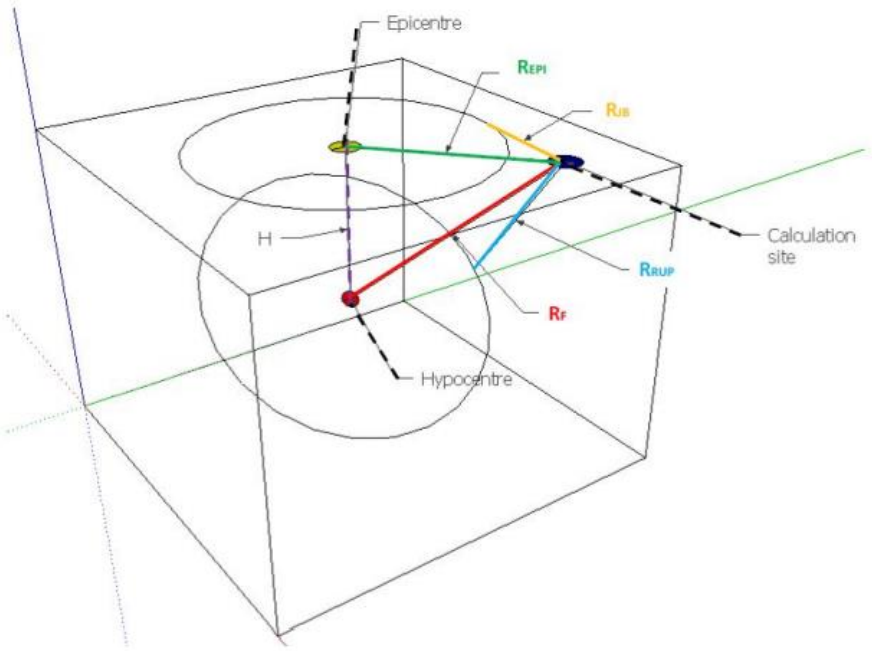


**Figure 2.4:** The four types of site-to-source distances recognized by R-CRISIS (Ordaz et al., 2018). H: focal depth, $\boldsymbol{R_F}$: focal distance, $\boldsymbol{R_{EPI}}$: epicentral distance, $\boldsymbol{R_{JB}}$: Joyner and Boore distance, $\boldsymbol{R_{RUP}}$: closest distance to rupture area.

Lastly, R-CRISIS allows the inclusion of local site effects in the seismic hazard computations. This is accomplished through terms of amplification and deamplification factors that depend on various parameters. The program considers the local site effects via different approaches (e.g. a grid file of Vs30 values). Most modern GMPEs (e.g. table 2.3) account explicitly for the soil type in their formulation, and therefore, provided that the input value is read from a given grid of site effects, the appropriate form of the GMPE may be used in the computations.

# Chapter 3 - Probabilistic Seismic Hazard Assessment results

In order to obtain the seismic hazard maps under the modified Gutenberg-Richter model the calculated seismicity rates (Table 2.2) were assigned, as described in previous sections, to the designated seismogenic zones. All computations were performed using the most recent version of the R-CRISIS software. A grid of 4800 points covering the study area (37.50°N - 39.08°N, 20.2°E - 21.38°E) was generated, with a grid spacing of 0.02° in both latitude and longitude. Five widely applied GMPEs for shallow Greek earthquakes were used (Makropoulos, 1978; Theodoulidis & Papazachos, 1992; Margaris et al., 2002; Skarlatoudis et al., 2003; Danciu & Tselentis, 2007). In the following sections the next acronyms will be used to refer to the selected predictive equations: Makropoulos (1978) denoted as MA78; Theodoulidis & Papazachos (1992) denoted as TP92; Margaris et al. (2002) denoted as MA02; Skarlatoudis et al. (2003) denoted as SK03 and Danciu & Tselentis (2007) denoted as DT07. The site-to-source distance used by all these GMPEs is the epicentral distance (Fig. 2.4). For each grid point, the PGA values were evaluated for generic rock site condition, for probability of exceedance of 10% in the next 50 years, which corresponds to a return period of 475 years.

The analysis of all these maps allows emphasizing the following remarks:

The isoacceleration maps derived from the use of each GMPE clearly delineate western Cephalonia Island as having higher seismic hazard than the rest of the study area which is characterized by relatively moderate seismic hazard levels. For a return period of 475 years, values up to 800 cm/s² are reached (Fig. 3.1e) for rock site conditions. This region coincides with the areas affected by some of the largest earthquakes in the Central Ionian Islands, occurred off the coast of western Cephalonia during the instrumental era, such as the 17th September 1972 (M = 6.3) earthquake (Papazachos & Papazachou, 2003), the 17th Janurary 1983 (M = 7.0) earthquake (Scordilis et al., 1985) and the 2014 doublet (Karakostas et al., 2015) (Fig. 1.2).

On the other hand, lower seismic hazard levels are computed for the island of Lefkas, but these values may not be neglected since they can cause significant damage to the island as previous experience has underscored in the case of 17th November 2015 (Mw = 6.5) earthquake when observed PGA values up to 0.36 g caused several damage and geological effects especially in the SW part of the Island (Papathanassiou et al., 2017; Lekkas et al., 2018).

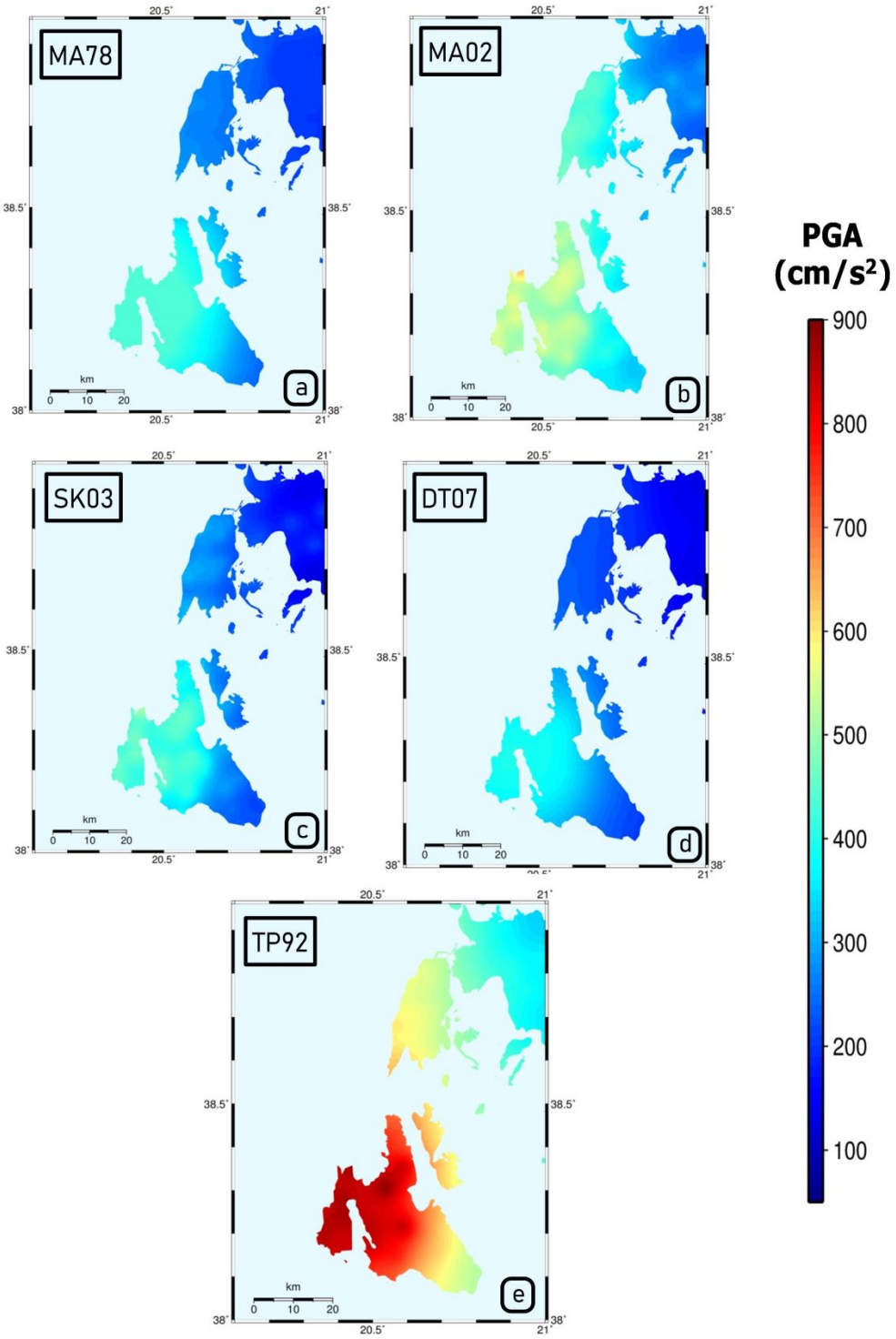


**Figure 3.1:** Seismic hazard maps depicting PGA values with 90% probability of exceedance for the next 50 years (return period of 475 years) using the GMPEs of **a)** Makropoulos et al., 1978 (MA78), **b)** Margaris et al., 2002 (MA02), **c)** Skarlatoudis et al., 2003 (SK03), **d)** Danciu & Tselentis, 2007 (DT07) and **e)** Theodoulidis & Papazachos, 1992 (TP92).

The PGA values estimated from the use of each GMPE exhibit variations in greater or lesser degree. In general, the average values derived from the TP92 relationship are highest ones (fig. 3.1e) whereas the average values from DT07 are the lowest (fig. 3.1d).

As it can be seen in Figure 3.2, the whole region of the Central Ionian Islands is included in Zone III of the Greek Building Code which corresponds to a PGA value of 0.36g with 10% probability of exceedance in the next 50 years. This value is, in greater or lower extent, smaller than the computed values from this study. This can be attributed to various factors: a) The seismological data used in the present study are more updated (until 2018) than the ones used for the compilation of the building code, b) The implementation of the newly proposed delineated seismic sources in this study offers a significant advantage towards a more detailed visual representation of the PGA spatial distribution, c) The methodologies implemented in each assessment are fundamentally different, therefore it may not be efficient to compare discrete PGA values.

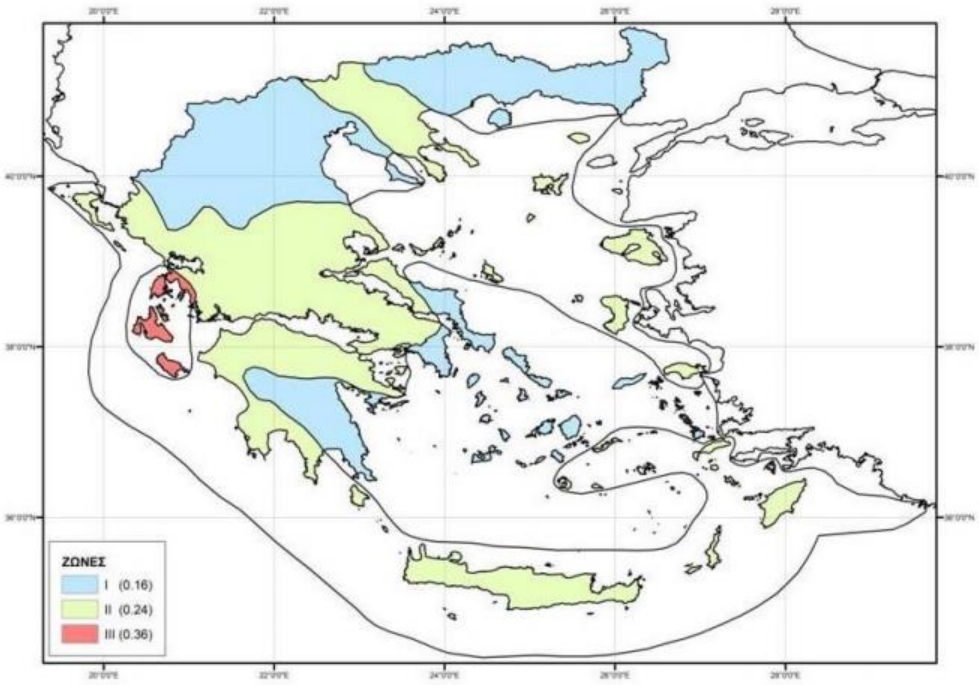


**Figure 3.2:** The current Greek Building Code, effective from 01/01/2014. The three hazard zones (0.16g, 0.24g and 0.36g correspond to Zone I, II and III respectively) refer to an average return period of 475 years in terms of PGA.

Numerous PSHA studies for the Greek territory have been published to date and can be used as a comparison with this study. Banitsiotou et al. (2004) estimated seismic hazard for various sites in Greece in terms of PGA and PGV which led to the distinction of

four seismic hazard zones. PGA values higher than 0.3 g (up to 0.45 g) were computed for the Central Ionian Islands, placing them at the most hazardous zone. Tselentis & Danciu (2010) applied a probabilistic approach similar to the one used in this study with the main difference lying in the assignment of different GMPEs to different seismic sources. In their assessment, Cephalonia Island is dominated by mean PGA values of 0.5 to 0.6 g and Lefkas Island by mean PGA values of 0.4 to 0.5 g. According to Segou (2010) the PGA values corresponding to a return period of 475 years calculated for Cephalonia Island range from 300 to 500 cm/s², with the most increased PGA values observed in Paliki peninsula. The corresponding values for Lefkas Island vary from 300 to 400 cm/s². Furthermore, another PSHA performed by Vamvakaris (2010) also illustrates western Cephalonia as the area with the most increased hazard levels (reaching 0.6 g) in the Central Ionian Islands. Lefkas Island along with the rest of Cephalonia Island display values ranging from 0.4 to 0.5 g with the higher ones determined at the SW part of Lefkas Island (Athani peninsula). Finally, seismic hazard maps were created within the SHARE project (Giardini et al., 2014) as a result of a PSHA carried out for the entire European and East Mediterranean region. Central Ionian Islands are included to the regions assigned with the highest hazard levels (up to 0.5g for a return period of 475 years).

The comparison of previous studies with the present one leads to the following remarks:

a) The spatial distribution of the highest levels of PGA in the present assessment is in good agreement with the maps of Segou (2010) and Vamvakaris (2010). The other studies are not sufficiently detailed to analyze this aspect.

b) Regarding the agreement of the computed levels of PGA, the hazard maps associated with MA78 and DT07 equations (fig. 3.1a & d) are comparable to the values proposed by Banitsiotou (2004) and Segou (2010). However, compared to the other studies the provided results appear to be underestimated, especially concerning Lefkas Island. On the other hand, the hazard maps created by the use of MA02 and SK03 equations (figs. 3.1b & c) contain higher PGA values, providing comparable results and sufficient agreement with other studies (e.g. Vamvakaris, 2010).

c) The differences observed between each PSHA outline the sensitivity of the determined seismic parameters. The major influence in the seismic hazard computations is related to the selection of GMPEs and the delineation of seismic sources. Lower but not negligible influence is related to the seismicity parameters and the regression method used.

d) The created hazard maps (Fig. 3.1a-e) show a more complex structure having more diverse scaling regarding their isoacceleration lines. This was expected since the

delineation of smaller seismic source zones led to more detailed spatial allocation of PGA values, which theoretically results in more realistic data.

# Chapter 4 - Physics-based broadband ground motion simulations

The prediction of strong ground motion at sites of interest for future large earthquakes is a crucial topic of engineering seismology. The scarcity of strong motion data, especially in the near-field, highlights the demand for reliable broadband simulations on which more reliable GMPEs can be based. The ability to generate broadband near-source strong ground motion synthetic waveforms is very important for detailed source modeling, given that the evaluation of source complexity is becoming more feasible in broader spatial and time detail. Furthermore, the potential of calculating large sets of near-source synthetic seismograms that include realistic source complexity is a powerful tool for up-to-date seismic hazard studies aiming to forecast the strong ground motion and its variability in future large earthquakes (Mai & Beroza, 2003).

In the context of engineering seismology, earthquakes initiate ground motions over a wide range of frequencies, whereas the vast majority of man-made structures have natural frequencies of vibration between 0.1 and 20 Hz (Fig. 4.1). For example, a typical 5-story building has a natural period of approximately 0.5 seconds and a natural frequency of approximately 2 Hz. When the slip between the two sides of a fault suddenly accelerates in a small patch of its surface, an earthquake is nucleated and as the rupture propagates, the heterogeneity of the fault leads to the generation of seismic waves over a wide frequency band. The seismic waves, during their course, are subject to refraction and reflection at the boundaries of the crustal layers. In addition, variations in rock type, seismic velocity and density, among others, result in the scattering of seismic waves with frequencies above 0.5 Hz which are observed after the arrival of shear waves traveling directly from the source.

At frequencies below a transition zone (usually at 1 Hz), relatively simple deterministic approaches are able to reproduce the pulse of ground motion observed at locations in the vicinity of the rupture initiation point. On the other hand, at higher frequencies (beyond 5 Hz) the stress field variations on the fault along with the seismic wave scattering in the crust make the use of stochastic approaches essential. In the crucial intermediate frequency band of 0.5 to 5 Hz, i.e. the natural frequencies of most buildings, the combination of these two different approaches is considered to be appropriate in order to effectively create synthetic time histories that match with the recorded ones.

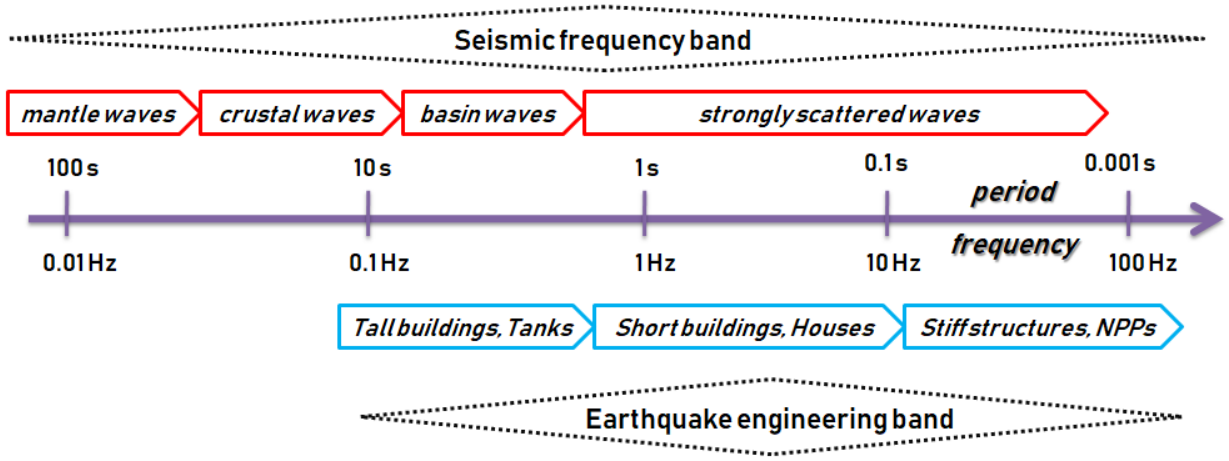


**Figure 4.1:** Seismic frequency band vs. Earthquake engineering band

The first attempts to simulate realistic time series of ground motions were made by Hartzell (1978) and Irikura (1986) who introduced a method of summing the recordings of smaller earthquakes in order to estimate the expected response of a larger earthquake. Since then, numerous methodologies have been proposed to include the source and path effects, as well as other complex characteristics.

The generation of strong ground motion synthetics requires the definition of either dynamic, kinematic or stochastic modeling of the earthquake source. A kinematic source model adopts a user-defined slip distribution along with a source time function (STF). The dynamic models, on the other hand, simulate the earthquake as a dynamically running shear crack that causes the radiation of seismic waves. A user-defined fault plane slips with a corresponding shear stress drop, having an assigned fracture criterion (e.g. slip weakening model) (Guatteri et al., 2004). The main difference between these two source models lies in the consideration of the underlying physical model behind the rupture process. Therefore, a major disadvantage regarding kinematic source models is the prerequisite of theoretical assumptions of the spatiotemporal slip distribution along the fault plane. These assumptions, such as the assumed rupture velocity and the definition of a precise form of the STF, may lead to unrealistic simulations (Song & Dalguer, 2013). On another note, dynamic modeling is more computationally inefficient given that the rupture process is nonlinear and the use of the reciprocity theorem is prevented (Kostrov & Das, 1988; Zhao et al., 2006). A useful alternative to dynamic models are the pseudodynamic models which provide the ability to develop physically and dynamically consistent earthquake source parameters in a relatively efficient way.

The pseudodynamic models, in other words, are kinematic models adjusted to approximate the critical characteristics of a dynamic rupture. This allows us to perform accurate earthquake source model simulations without the intense computational effort of a fully dynamic model (Guatteri et al., 2004).

In the present thesis, a physics-based hybrid approach is adopted to generate broadband strong ground motion seismograms. The low-frequency (LF) portion of the synthetic time series was calculated by using a 3D wave propagation method, whereas a stochastic finite-fault simulation model was implemented to acquire the high-frequency (HF) portion. The separately calculated ground motions were then merged, in order to obtain the entire time series. The LF portion was computed using the discrete-wavenumber finite-element (DWFE) technique of Olson et al. (1984), extended to finite fault discretization (Spudich & Archuleta, 1987; Spudich & Xu, 2002). On the other hand, the EXSIM code (Motazedian & Atkinson, 2005; Boore, 2009) was employed to calculate the HF portion of the seismograms. Finally, the results from the abovementioned techniques were merged by performing a weighted summation at intermediate frequencies to calculate the broadband synthetic time series.

## 4.1 Stochastic Ground Motion Simulation

The ground motion u(t) that is recorded at a seismological station can be expressed as the convolution of the seismic source s(t), the wave propagation path p(t), the local site effect g(t) and the instrument response i(t) (eq. 4.1):

$$u(t) = s(t)*p(t)*g(t)*i(t) \quad (4.1)$$

In the frequency domain, the convolution is equivalent to multiplication, therefore equation (4.1) can be expressed as:

$$U(f) = S(f)\cdot P(f)\cdot G(f)\cdot I(f) \quad (4.2)$$

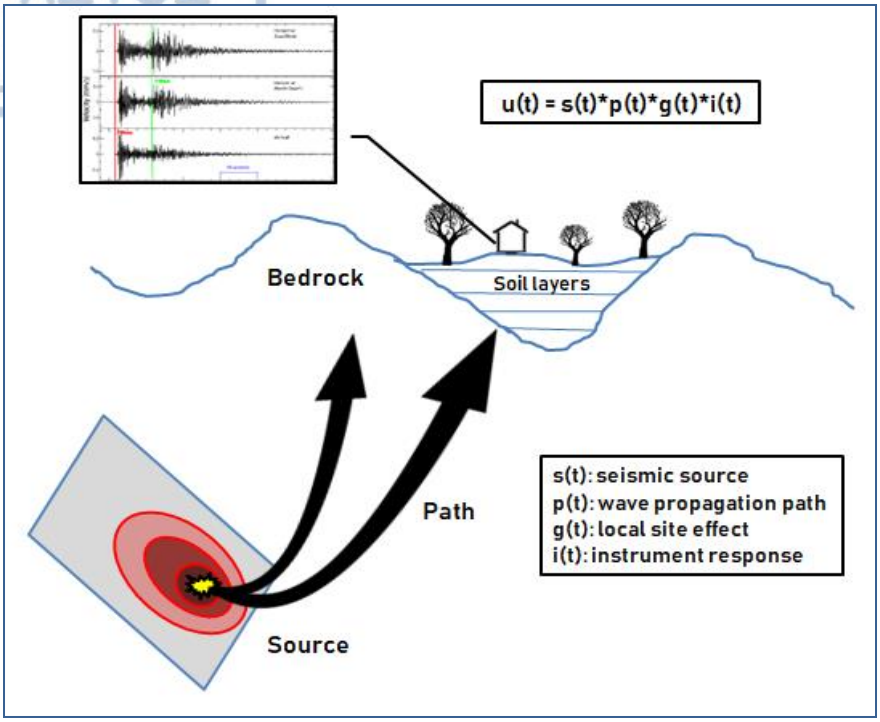


**Figure 4.2:** Schematic representation of seismic wave propagation from the seismic source to the ground surface.

The seismic source characteristics include the effect of various parameters such as the fault dimensions, the seismic moment, the nucleation point, the slip distribution, etc. The path characteristics integrate the attenuation properties, such as the geometrical spreading, on the propagation path. Moreover, the site characteristics are related to the effects of the shallower sedimentary layers to the seismic motions, namely the site amplification factors, the generation of surface waves and so on (Fig. 4.2).

In stochastic simulations, as firstly described by Boore (1983), ground motion can be represented as band-limited white noise (Gaussian noise) with an ω-squared mean Fourier spectrum (Fig. 4.3a) which can be generated theoretically by simple models of the seismic source (Aki, 1967; Brune, 1970, 1971). The simulation methodology is based on the generation of transient time series whose amplitude spectrum matches with the desired spectrum. The simplest representation of the seismic source is the point source model (Boore and Atkinson, 1987; Atkinson and Boore, 1995). The initial step of this approach demands, as mentioned before, the generation of random white Gaussian noise with zero mean and unit variance for a specific finite duration of motion. This generated noise is windowed (usually using Saragoni-Hart and boxcar windows) to form a realistic shape of the acceleration time series (Fig. 4.3b) The time series is then transformed to the

frequency domain (Fig. 4.3c) and the noise spectrum is normalized in a way that the Root Mean Square (RMS) spectrum equals unity (Fig. 4.3d). The theoretically computed deterministic ground motion spectrum is multiplied with the RMS of the random signal spectrum (Fig. 4.3e). Finally, the new spectrum is transformed back into the time domain leading to the resulting stochastic acceleration time series (Fig.4.3f) (Boore, 2003). However, the finite-fault models are most appropriate for the simulation of strong ground motion, as they allow the consideration of effects related to the geometry of the fault, the slip heterogeneity and the source directivity which play an important role on the ground motion simulations.

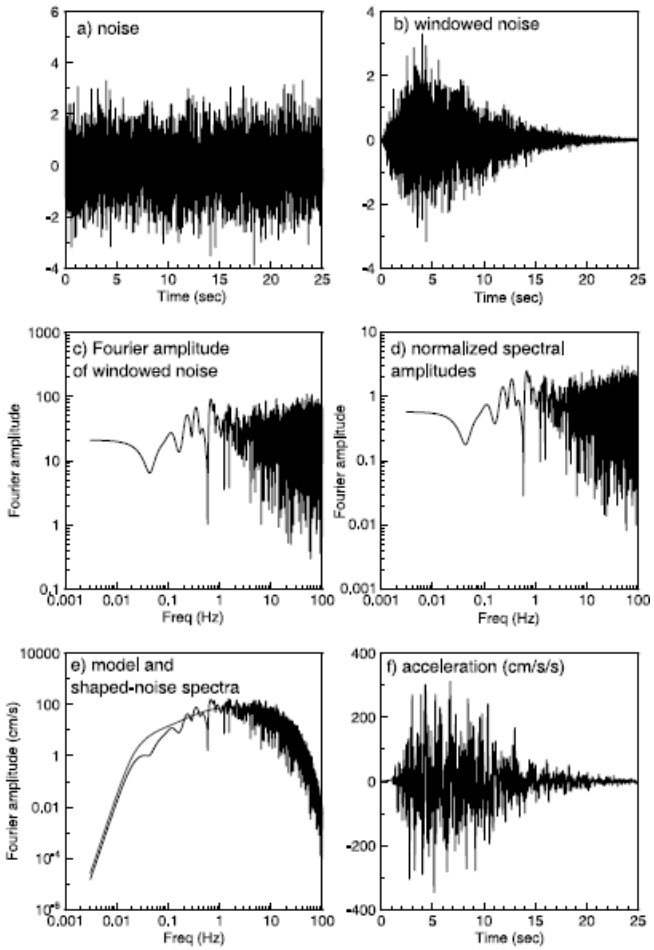


**Figure 4.3:** Illustration of the steps required for the stochastic simulation methodology (after Boore, 2003). a) Generation of a normally distributed signal of zero mean and unit variance. b) Multiplication of the noise signal by a window function (e.g. Saragoni-Hart exponential window). c) Estimating the Fourier transform of the windowed signal. d) Normalization of the resulting signal ensuring that its root mean square amplitude spectrum equals unity. e) Calculation of the theoretical (deterministic) point-source spectrum as a function of frequency in virtue of the seismic moment and distance from the point source. f) Calculation of the inverse Fourier transform of the site spectrum to acquire the simulated seismogram.

## 4.2 Stochastic Finite-Fault Modeling - The EXSIM code

The stochastic finite-fault method of Motazedian & Atkinson (2005) was applied to generate the HF portion of the broadband time series. On that account, EXSIM, an open source code for stochastic ground motion simulation based on a dynamic corner frequency approach was employed (Motazedian & Atkinson, 2005; Boore, 2009; Assatourians & Atkinson, 2012). EXSIM is essentially an extension of the point-source stochastic method (Boore, 1983, 2003) which incorporates the rupture propagation along an extended fault plane. A ruptured fault segment with a size equivalent to its seismic moment is subdivided into a grid of subsources, each one of which is then treated as a point source producing an ω-squared spectrum (Aki, 1967; Brune, 1970; Boore 1983). The corresponding ground motions from all subsources are summed at the observation points in the time domain with an assigned time delay to acquire the ground motion from the entire fault.

In the dynamic corner frequency approach (Motazedian & Atkinson, 2005), the corner frequency of the first subfault (the nearest subfault to the beginning of the rupture) is:

$$f_{011} = 4.9 \cdot 10^6 \cdot \beta \left(\frac{\Delta\sigma}{M_{011}}\right)^{\frac{1}{3}} \quad (4.3)$$

where $M_{011}$ is the seismic moment of the first subfault, Δσ is the stress drop (in bars) and β is the shear-wave velocity (in km/s).

The dynamic corner frequency of the ijth subfault can then be defined as a function of the cumulative number of the subfaults that ruptured at time t:

$$f_{0ij}(t) = N_R(t)^{-\frac{1}{3}} \cdot 4.9 \cdot 10^6 \cdot \beta \left(\frac{\Delta\sigma}{M_{0ave}}\right)^{\frac{1}{3}} \quad (4.4)$$

where $M_{0ave}$ is the average seismic moment of all subfaults.

When t = $t_{end}$, the number of subfaults that ruptured $N_R(t)^{-\frac{1}{3}}$ equals to $N^{-\frac{1}{3}}$. Accordingly, the corner frequency at the end of the rupture is given by:

$$f_{0ij}(t_{end}) = N^{-\frac{1}{3}} \cdot 4.9 \cdot 10^6 \cdot \beta \left(\frac{\Delta\sigma}{M_0/N}\right)^{\frac{1}{3}} \quad (4.5)$$

which therefore equals to $f_0$, the corner frequency of the entire fault. This indicates that the lower limit of the dynamic corner frequency is the corner frequency of the entire

fault. As the rupture propagates towards the end of the fault, the number of the ruptured subfaults increases and, as a consequence, the corner frequency of each subfault and the total radiated spectra decreases. The level of the spectrum of each subfault and the corresponding radiated spectrum at high frequencies is inclined to decrease as the corner frequency decreases, through the dynamic corner frequency approach. Along these lines, the EXSIM algorithm applies a scaling factor in order to adjust this phenomenon and preserve the level of the total radiated energy of subfaults at higher frequencies. In this context, the acceleration spectrum $A_{ij}$(f) of the ijth subfault is expressed as:

$$A_{ij}(\mathrm{f}) = \mathrm{C} \cdot M_{0ij} \cdot H_{ij} \cdot (2\pi f)^2 \,/\, [\,1 + (f/f_{0ij})^2] \tag{4.6}$$

where $H_{ij}$ represents the scaling factor applied to preserve the high frequency spectral content of the subfaults.

The radiated energy attributable to the entire fault (E) at high frequencies must be N times greater than the radiated energy from the ijth subfault ($E_{ij}$) at high frequencies (eq. 4.7).

$$E_{ij} = \frac{E}{N} \tag{4.7}$$

$$E_{ij} = \frac{1}{N} \int \frac{C\, M_0\, 2\pi f^2}{\left[1 + \left(\frac{f}{f_0}\right)^2\right]} \,\mathrm{df} \tag{4.8}$$

Therefore, combining (4.7) and (4.8), the radiated energy from the ijth subfault at high frequencies is expressed by:

$$E_{ij} = \int \frac{C \cdot M_{0ij} \cdot H_{ij} \cdot (2\pi f)^2}{1 + \left(\frac{f}{f_{0ij}}\right)^2} \,\mathrm{df} \tag{4.9}$$

Given that $M_{0ij} = M_0$ / N, the scaling factor ($H_{ij}$) can be found by equating (4.8) and (4.9):

$$H_{ij} = \left( \frac{N \cdot \Sigma \left( \frac{f^2}{1 + \left(\frac{f}{f_0}\right)^2} \right)}{\Sigma \left\{ \frac{f^2}{1 + \left(\frac{f}{f_{0ij}}\right)^2} \right\}} \right)^2 \tag{4.10}$$

This equation can be solved in the frequency domain for each subfault. The radiated energy from the ijth subfault matches the total radiated energy from the first subfault, but the shape of the spectrum depends on the calculation of the corner frequency derived from the total ruptured area of the fault. Therefore, the radiated energy from each subfault does not change as the rupture propagates but the energy is distributed into lower frequencies.

The cumulative number of subfaults ($N_R$) contributing to the rupture increases with time at the initial stages of the rupture but as time passes by it becomes constant at a settled percentage of the total ruptured area. As a result, the dynamic corner frequency decreases with time close to the initiation of the rupture and after a while it becomes constant. This pattern is controlled by a parameter which defines the maximum ruptured area of the fault at any time. Assuming that 50% of the fault area is ruptured, this means that 50% of the total subfaults are activated and contribute to the dynamic corner frequency, whereas the remaining subfaults are inactive. The ability to define a specific portion of the fault surface as active, reflects the fact that the rupture close to the hypocenter of a large earthquake may have stopped even before the rupture reaches the edge of the fault. In conclusion, one of the main advantages of the EXSIM code is that, by using the dynamic corner frequency approach, the total radiated energy from all subfaults remains the same, independent from their dimensions. Thus, it allows the method to be suitable for a wide range of magnitudes.

### **4.2.1** Source parameters

Source parameters include the fault orientation (strike and dip) and its dimensions, the fault burial depth, the position of the hypocenter on the fault surface, the moment magnitude, the slip distribution along the fault plane and the stress parameter (Δσ).

The stress parameter (Δσ) is one of the most crucial parameters and the most difficult to determine in the context of stochastic ground motion modeling. It must be emphasized that the Δσ value should not be mixed with the stress drop and must be interpreted with caution (Beresnev & Atkinson, 1997). The stress parameter value cannot be calculated directly from the earthquake source but it can be obtained by fitting the observed response spectra. As a result, the quantity Δσ may have little connection with the actual stress change occurring during an earthquake. Generally, the stress drop indicates the difference in the state of stress before and after the rupture initiates. A simple approximation is:

$$\Delta_\sigma = \tau_0 - \tau_1 \quad (4.11)$$

where $\tau_0$ is the stress concentration due to stress accumulation for any point on the fault plane and $\tau_1$ is the final value of stress after slip occurs. Variations of stress drop are expected over the fault plane, therefore in stochastic ground motion simulations, the value used is defined by the integration of static stress drop over the fault plane divided by the fault area.

According to Brune (1970, 1971) the stress drop $\Delta\sigma$ can be expressed as a function of the seismic moment $M_0$ and the corner frequency $f_0$as:

$$\Delta\sigma = \frac{7\,M_0}{16}\left(\frac{2\pi f_0}{2.34\beta}\right)^3 \quad (4.12)$$

where β is the shear wave velocity in km/s. It has been shown that higher stress drop values result in higher ground motion estimation, however, stress drop is not necessarily directly connected with the earthquake size (Kanamori & Anderson, 1975). The range of stress parameters commonly used in stochastic simulations for shallow earthquakes (50 - 100 bars) is significantly lower than the values used for intermediate and deep earthquakes (100 - 600 bars). For the Greek territory, the initial value for the stress parameter is derived from Margaris & Boore (1998) and Margaris & Hatzidimitriou (2002) who performed simulations of response spectra of strong Greek earthquakes. Their average value of 56 bars is close to the average value (60 bars) computed by Kanamori & Anderson (1975).

On a final note, the wide range of possible stress parameter values may lead to significant variability in ground motion estimation. As a result, the forecast of future large earthquakes may present large uncertainties, even though the location and the fault plane geometry can be well specified (Beresnev & Atkinson, 1997). In this regard, a common practice to determine the stress parameter is a trial and error approach.

### **4.2.2** Path properties

Geometric spreading is a factor that reflects the reduction of seismic wave amplitudes due to the distance they travelled. In a simplistic model of a homogeneous and spherical earth, the body wave amplitudes decay inversely proportional to the distance R travelled. However in reality the earth is neither homogeneous nor spherical, so the geometric spreading is different than 1/R. In this regard, a simple model of $R^{-1}$ was specified for near-source distances till a transition distance (40 km) for which $R^{-0.5}$ is

used, where the lower exponent at largest distances represents the transition to surface-wave spreading (Atkinson & Assatourians, 2014).

Furthermore, it is well known that the earth does not demonstrate a perfectly elastic behavior, hence, the seismic waves are exposed to damping during their course on the earth's interior. The medium through which the seismic waves propagate has certain properties that lead to the decrease of their spectral amplitudes. This type of damping is called "anelastic" attenuation and is parameterized by the quality factor Q (Lay and Wallace, 1995). The frequency-dependent anelastic attenuation in terms of the quality factor function is expressed as:

$$Q(f) = Q_0 f^n \tag{4.14}$$

where $Q_0$ is an indication of the heterogeneity of the medium and n is directly proportional to the seismicity of the region (Raghukanth and Somala, 2009). In general, low $Q_0$ and high n values characterize seismically active regions, whereas more stable regions exhibit high Q values with lower n values (Singh et al., 2004).

Worldwide, regions with different seismotectonic features have different Q-values (Aki, 1980; Jin & Aki, 1988). If the Q-value of a region is small, the seismic waves are subject to higher attenuation and their amplitudes are expected to decrease quickly, compared to regions with higher Q-values. Apart from these properties, the quality factor is a crucial parameter for stochastic simulations, considering that the assigned Q value determines the shape of the Fourier amplitude spectrum at higher frequencies.

### **4.2.3** Site properties

The parameters employed in order to quantify the impact of the shallower sedimentary layers to the seismic motion are the kappa parameter and the soil amplification factors. The kappa ($\kappa_0$) parameter is defined as an exponential decay to represent the diminution factor (Anderson & Hough, 1984) and can be regarded as a low-pass filter. The diminution factor D(f) used in the stochastic modeling, in relation with the kappa filter is expressed by:

$$D(f) = e^{-\pi\kappa_0 f} \tag{4.13}$$

The physical significance of the kappa factor is still unresolved. Several researchers support that it is a local site effect connected with the competence of the near-source materials (Hanks, 1982; Atkinson, 2004). On the contrary, others claim that it is related to

source processes related to the size of a minimum cohesive zone (Papageorgiou & Aki, 1983). It is also likely that kappa may have both source and site origins (Atkinson, 1996).

Multiple studies have been conducted in order to determine the kappa values applicable for large earthquakes in Greece. Hatzidimitriou et al. (1993) used a dataset of strong motion accelerograms recorded at sites varying from very soft to stiff soil conditions and estimated an average $\kappa_0$ value of 0.06. The same average value was also obtained from Margaris & Boore (1998), though for class B sites the corresponding value diminishes to 0.035. In latest studies (Klimis et al., 1999), kappa values for NEHRP class C (0.044) and D (0.066) Greek sites were determined in an effort to provide frequency-dependent amplification factors following a class classification system.

The definition of soil types and site amplification factors is a fundamental aspect in ground motion simulations. Local site effects are distinguished from the path effects in the EXSIM algorithm, thus the amplification (or diminution) factors are not associated with the properties of the medium between the seismic source and the site. There are numerous methodologies to determine the local site response, especially when the velocity profile of the local soil layers is known. These methodologies are based on the use of theoretical transfer functions in order to determine the amplification (or diminution) factors. Alternatively, in cases where the velocity profile is unknown, different methodologies are employed, such as the horizontal-to-vertical ratio (H/V) (Nakamura, 1989) and the standard spectral ratio (SSR) (Borcherdt, 1970) methods. It is vital for engineering design and building codes to quantify the effect caused by the soil deposits given that they can potentially amplify ground motions significantly. The level of amplification depends on various factors such as layer thickness, soil compactness and age. Shear wave velocity, density and damping are also controlled by these factors (Siddiqqi & Atkinson, 2002). Generally, soil sites are considered to amplify ground motions more than rock sites, especially at lower (≤ 2 Hz) frequencies. The amplification of rock sites originates from their shear-wave velocity gradient (Beresnev & Atkinson, 1997; Boore & Joyner, 1997) and in some cases can be significant.

## 4.3 The Discrete Wavenumber Frequency Technique - COMPSYN code

The COMPSYN package was employed to generate the LF portion of the broadband time series. It is comprised by Fortran applications aiming to calculate synthetic seismograms for hypothetical fault ruptures occurring on faults of finite spatial extent (Spudich & Xu, 2002). The methodology of Spudich & Archuleta (1987) is used to estimate the representation theorem integral onto the assumed fault surface whereas the

DWFE method of Olson et al. (1984) is applied to calculate the Green's functions that represent the response of the laterally homogeneous velocity structure. The Green's functions are calculated as tractions on the fault plane by taking advantage of the reciprocity theorem and are evaluated on a user-defined grid of points on its surface. Following, the convolution between the slip and the calculated Green's functions is performed based on a kinematic fault model and the result is integrated over the fault surface resulting in the spectra of ground motion at the desired locations. The synthetic time series are ultimately produced by inverse transformation of the synthetic Fourier spectra. It should be noted that COMPSYN does not account for the attenuation of seismic waves in the earth's interior. Nonetheless, in the examined case studies the attenuation effect is considered to be insignificant given that COMPSYN is employed only for the LF motion simulations at close distances from the fault. The COMPSYN package consists of five interconnected applications which are executed one after the other (Fig. 4.4). Each application requires either a user-defined file or / and the output of the previous one.

- OLSON requires a user-defined input file containing the description of the earth's structure represented as a structure of laterally homogeneous horizontal layers with possible discontinuities. OLSON is basically a modified version of the DWFE code of Olson et al. (1984) and is used in order to calculate Green's functions in the wavenumber and frequency domain.

- XOLSON is a fast application that reshuffles the results obtained from the OLSON application.

- TFAULT demands an input file containing the definition of the fault plane by the user as well as the output files created by the XOLSON application. The Green's functions are then evaluated on the fault plane by Bessel transforming the XOLSON output from the wavenumber-frequency to the space-frequency domain.

- SLIP combines the TFAULT output files along with a user-defined rupture model. The dot (scalar) product of the slip and the Green's functions is formed and integrated over the fault surface to produce the ground motion spectra at the desired locations.

- SEESLO is the final application of COMPSYN. It reads the spectral files produced by the SLIP application and performs an inverse Fourier transformation to the time domain. Finally, the filtered velocity and displacement time series are written to ASCII output files.

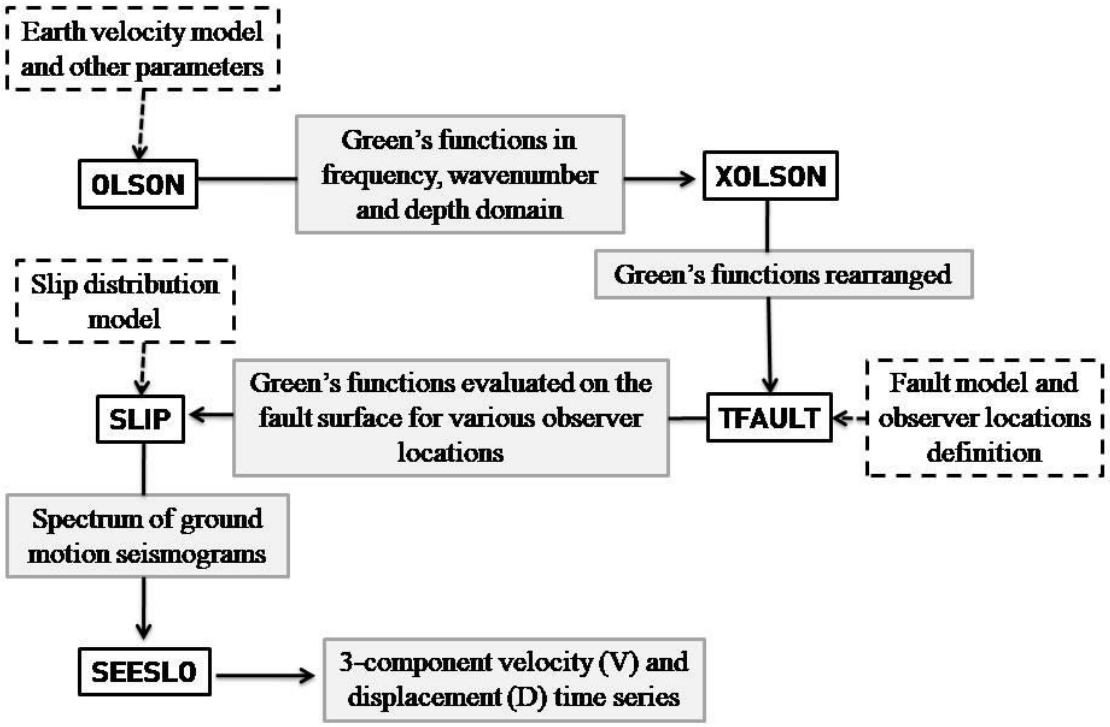


**Figure 4.4:** Flowchart of the COMPSYN package describing the sequence in which applications are run. The boxes with black borders represent the five COMPSYN applications. The boxes with dashed borders explain the user-defined input files and the boxes with gray borders contain the description of the files created by an application.

### **4.3.1** Discrete Wavenumber Finite Element Method (DWFE)

The DWFE method is a procedure for computing the elastic response of a vertically heterogeneous half-space. As for the horizontal dependence of the wavefield, a discrete wavenumber decomposition is applied in the form of a Fourier - Bessel series. According to Olson et al. (1984) a general expression for displacement u in a cylindrically symmetric medium is given by:

$$u\,(r,\phi,z,t) = \sum_m \int_0^\infty \frac{k}{2\pi} \left[U_{zk}^m(z,t)\; R_k^m(r,\phi) + U_{rk}^m(z,t)\; S_k^m(r,\phi) + U_{\varphi k}^m(z,t)\; T_k^m(r,\phi)\right] dk \quad (4.15)$$

Thr vertical derivative of u, $u' \equiv du / dz$ is:

$$u'(r,\phi,z,t) = \sum_m \int_0^\infty \frac{k}{2\pi} \left[U'^m_{zk}(z,t)\; R_k^m(r,\phi) + U'^m_{rk}(z,t)\; S_k^m(r,\phi) + U'^m_{\varphi k}(z,t)\; T_k^m(r,\phi)\right] dk \quad (4.16)$$

where $R_k^m$, $S_k^m$ and $T_k^m$ are the surface vector harmonics (Olson et al., 1984)

r, ϕ and z are the cylindrical coordinates (radial, azimuthial, vertical) in the far field

k is the horizontal wavenumber and

m is the angular order of the Bessel function

The definition of the surface vector harmonics is given by:

$$R_k^m(\mathrm{r},\phi) = Y_k^m(\mathrm{r},\phi)\, e_z \tag{4.17}$$

$$S_k^m(\mathrm{r},\phi) = \frac{1}{k}\,\partial_r\, Y_k^m(\mathrm{r},\phi) e_r + \frac{1}{kr}\partial_\varphi\, Y_k^m(\mathrm{r},\phi)\, e_\varphi \tag{4.18}$$

$$T_k^m(\mathrm{r},\phi) = \frac{1}{kr}\partial_\varphi Y_k^m(\mathrm{r},\phi) e_r - \frac{1}{k}\,\partial_r Y_k^m(\mathrm{r},\phi) e_\varphi \tag{4.19}$$

where $Y_k^m(\mathrm{r},\phi) = J_m(\mathrm{kr}) e^{im\varphi}$ for m = 0, ± 1, ± 2, ...

### **4.3.2** Model parameters

The numerical techniques of Spudich & Archuleta (1987), which are implemented in the framework of the COMPSYN code, require the definition of parameters concerning the earth's velocity structure, the fault characteristics and the earthquake slip distribution. The velocity structure in COMPSYN is considered as one-dimensional in depth and the free surface is set where the depth equals zero. In order to calculate the Green's functions in the wavenumber and frequency domain, the parameters defining the earth's structure are the P and S-wave velocities along with the crustal density as a function of depth. These velocity structures are laterally homogeneous, but possible discontinuities may be portrayed. It is evident that the accuracy of the computed deterministic Green's functions relies on the validity of the assigned velocity model. Another critical factor regarding the calculation of Green's functions in the frequency domain is the fault and stations setting.

For the purpose of generating synthetic seismograms for specific rupture models at the fault surface, an earthquake slip distribution needs to be defined. On that basis, a slip-velocity function is considered to be uniform at all points of the fault surface. This may be a boxcar function, a decaying exponential or other more complicated ones. These functions are characterized by the duration and the amplitude of slip velocity function

and the slip initiation time. These parameters are set in COMPSYN according to the following approach. A set of parallel (equally spaced) lines are specified on the fault plane covering the total ruptured fault extent. Then, four quantities need to be defined at a set of points equally or unequally distributed along this line. These quantities are the rupture time (the time when the rupture is initiated at this point), the duration (for example the time lag when the slip velocity is nonzero when the slip-velocity function is a boxcar) and the amplitude of the slip velocity vector (consisting of the strike-slip and the dip-slip component of the slip velocity). After these quantities are specified, they can be computed at any other point on the fault by linear interpolation.

Apparently, slip is a 2-component vector, as it is derived from a strike-slip and dip-slip component. In COMPSYN, ground displacements are computed by the use of the representation theorem of Spudich (1980):

$$\overline{u}_k\ (x,\omega) = \int_{vmin}^{vmax} \int_{umin}^{umax} \overline{s}\ (u,v,\omega) \cdot \overline{T_k}\ (u,v,\omega;x)\ du\ dv \qquad (4.20)$$

where x is the position of the observer (the location on the earth's surface where the synthetic seismograms will be calculated),

u and v are the coordinates on the fault plane,

k = 1,2 or 3 signifies the x,y or z direction,

$\overline{u}_k$ (x,ω) is the Fourier transform of the k-component of displacement at the observer location x for angular frequency ω,

$\overline{s}$ (u,v,ω) is the Fourier transform of the two component slip vector at the point (u,v) on the fault and

$\overline{T_k}$ (u,v,ω;x) is the Fourier transform of the two component traction vector at u and v on the fault as a result of a point impulsive force in the k-direction at the observer location x.

## 4.4 Merging

The generation of broadband time series requires the implementation of a merging technique that combines the stochastic HF signal with the LF wavefield. There are a handful of methods proposed in the literature for this procedure with the merging taking place either in the time (Berge et al., 1998) or in the frequency domain (Graves & Pitarka,

2004) at a pre-defined matching frequency. However, it has been observed that in many cases the derived response spectra demonstrates an irregular behavior at the frequency part where the deterministic signal ends and the stochastic one begins (Mai & Beroza, 2003). This leads to an underestimation of the energy content around the matching frequency which ultimately leads to inconsistencies in comparison with the real data.

In the present thesis, the method of Mai & Beroza (2003) was used to generate the broadband synthetics. This method has the advantage of minimizing the amplitude and phase mismatch between the LF and HF signals by applying frequency-dependent weighted functions and by using an optimization process operating in a narrow frequency range (0.1 - 0.2 Hz) around a target matching frequency (Mai & Beroza, 2003).

## 4.5 1st case study - The Cephalonia 26th January 2014 M6.1 earthquake

### **4.5.1** The January - February 2014 sequence

The whole earthquake sequence, comprised by two main shocks with approximately the same magnitude, occurring in a short time period (January 26 and February 03) and space. The first mainshock (Mw = 6.1) of January 26 took place in the SW part of Cephalonia Island and more specifically in the Paliki peninsula. According to Karakostas et al. (2015) who performed a high-precision relocation of the complete seismic sequence, the epicenter was located at 38.203°N, 20.4308°E and a focal depth of 16 km was reported. On the other hand, the second mainshock (Mw = 6.0) of February 3 occurred north-northwest of the first one, about 7 km north of Lixouri. The epicenter was relocated at 38.267°N, 20.323°E and a depth of 7 km was reported. Other researchers also attempted the relocation of the whole sequence (Papadopoulos et al., 2014; Karastathis et al., 2015) unveiling a variability in the determination of the epicenters of the two main events. This can be attributed to the diverse use of seismological stations in each study. The moment tensor solutions (obtained by GCMT) determined the focal mechanism of the first (strike = 20° / dip = 65° / rake = 177°) and the second event (strike = 12° / dip = 45° / rake = 154°) of the doublet. The aftershock activity lasted for several months. The strongest aftershock (Mw = 5.5) occurred in the first few hours after the first mainshock (GCMT: strike = 11° / dip = 45° / rake = 120°).

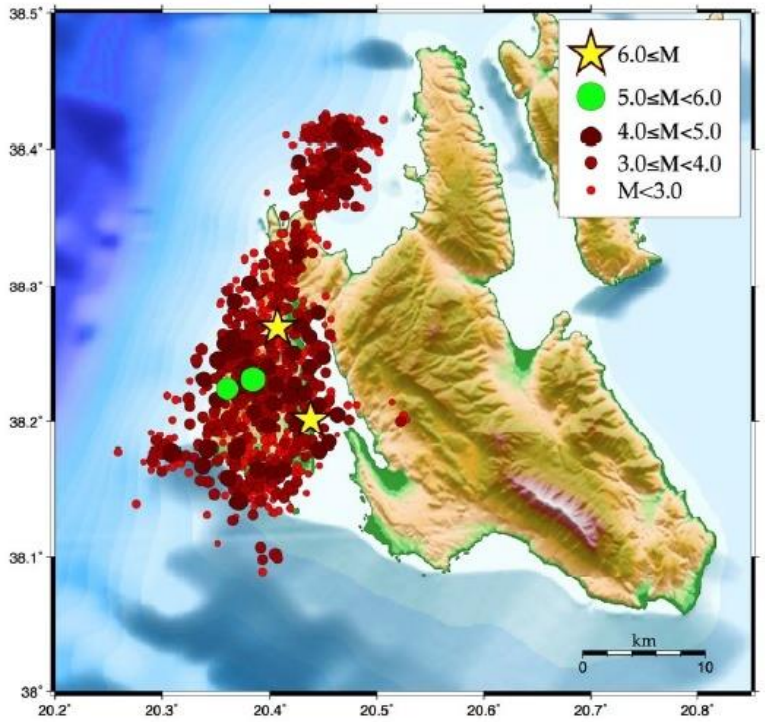


**Figure 4.5:** Relocated aftershock activity of the first 22 days of the sequence (26 January - 16 February 2014) after Karakostas et al. (2015).

The epicentral distribution of the aftershock sequence reveals the activation of a fault striking NNE-SSW, parallel to the major axis of Paliki peninsula, extending for almost 35 km (Papadopoulos et al., 2014; Karakostas et al., 2015; Karastathis et al., 2015). According to Karakostas et al. (2015) the overflowing aftershock sequence following the first main event (Mw = 6.1) of the doublet is concentrated near the focal area and suggest a fault of 13 km length. To the north, an area of relatively low seismicity was identified due to the absence of Mw > 4.0 earthquakes. The southernmost part of this low seismicity area encompassed the second main event (Mw = 6.0) of the doublet (Fig. 4.5) The aftershock sequence of the second event was less intense and revealed a 10 km long rupture plane. The same authors suggest that the low seismicity level observed after the first main event in the area hosting the second main event, may suggest the existence of an asperity that remained locked after the first main shock and was activated during the second one. Moreover, this area was characterized by relatively low seismicity even after the occurrence of the second main shock. This can be explained by the absence of other smaller faults in this area. On the contrary, the southern part exhibited higher seismicity levels as a result of the activation of secondary faults and stress transfer after the second main shock (Karakostas et al., 2015).

From another standpoint, according to Karastathis et al. (2015) there is no convincing evidence to associate the January - February 2014 sequence with the Cephalonia segment of the KTFZ. The onshore strike-slip faulting observed in western Cephalonia could be attributed to the southern prolongation of the Lefkada segment. This is in agreement with the results of Papadopoulos et al. (2014) who proposed the reconsideration of the KTFZ regarding this segment, which does not terminate off the coast of SW Lefkas, but extends further into western Cephalonia and is possibly divided into two branches with an onshore and an offshore segment. Another possible explanation is the activation of a 30 km strike-slip fault zone, trending N-S, that divides the Island into a western and an eastern part. This scenario conceives western Cephalonia as a separate seismotectonic block from eastern Cephalonia, where the large 1953 earthquake sequence occurred (Karastathis et al., 2015).

Strong ground motion recordings are available for the January 26 event mainly from the permanent network of the ITSAK accelerographs (Fig. 4.6). As far as the second main event of February 3 is concerned, additional data were acquired from a temporary network of three accelerographs deployed the days following the first main event. The second main shock demonstrated the highest recorded peak ground motion parameters compared to the first one (Table 5.1). This can be explained by the difference regarding the focal depth of the two main shocks and by the strong evidence of forward directivity characterizing the second event (Sokos et al., 2015; Theodoulidis & Grendas, 2016; Garini et al., 2017). The value obtained at CHV1 (Chavriata) station, located in the southern part of Paliki peninsula (0.77 g), is the largest PGA value ever recorded in Greece (Theodoulidis et al., 2016).

Despite the fact that the level of seismic excitation imposed to the structures of Cephalonia Island was significantly higher than the design values of the previous and current antiseismic regulations, the observed damage was much lower than expected. This can be attributed to the fact that the majority of the structures in the affected areas were constructed after the 1953 (Mw = 7.2) earthquake. Moreover, the traditional construction practice on the island, due to the accumulated experience from its abundant seismic history, was a critical factor to the reduction of expected damage (Theodoulidis et al., 2016). After the January 26 event, the most severe structural damage was observed at the Paliki peninsula, whereas the rest of the island was slightly affected. Although no buildings collapsed, extensive damage was reported in masonry, reinforced buildings and monuments such as monasteries, churches and cemeteries (GEER, 2014; Lekkas & Mavroulis, 2015).

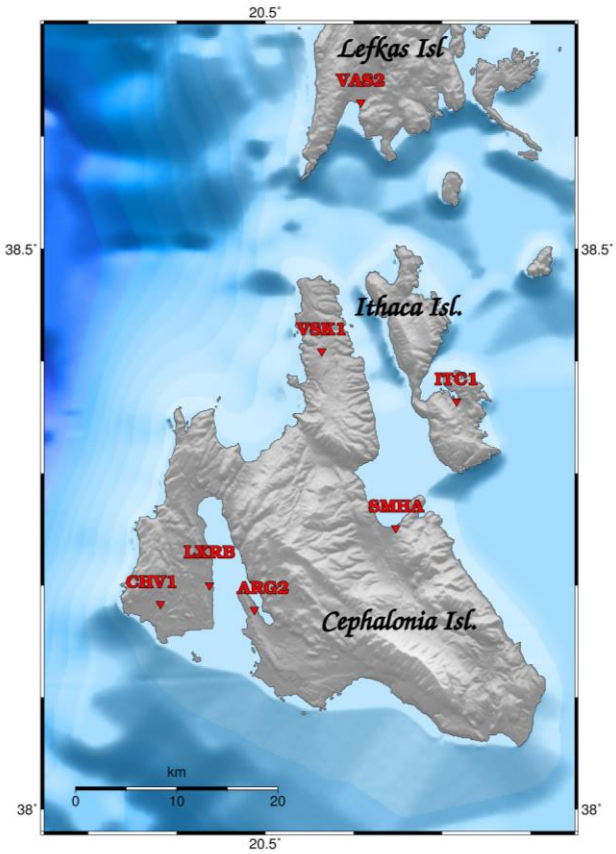


**Figure 4.6:** Locations of the seismological stations providing the strong motion data for the 26th January and 3rd February earthquakes.

**Table 4.1:** Strong motion stations (column 1-5) located close to the epicenter locations (column 6). Recorded PGA values in all three components for the January 26 (Mw = 6.1) and February 3 (Mw = 6.0) earthquakes are presented in columns 7-9.

| | Location | Code | Owner | Lat (°N) | Lon (°E) | Epic. distance (km) | PGA (N-S) (cm/s²) | PGA (E-W) (cm/s²) | PGA (Z) (cm/s²) |
|---|---|---|---|---|---|---|---|---|---|
| **26/1/2014** | Argostoli | ARG2 | EPPO - ITSAK | 38.178 | 20.488 | 13 | 349 | 424 | 324 |
| | Vasilikiades | VSK1 | | 38.412 | 20.562 | 34 | 95 | 79.6 | 55.1 |
| | Ithaca | ITC1 | | 38.365 | 20.716 | 40 | 56.5 | 60.4 | 37.6 |
| | Vasiliki | VAS2 | | 38.630 | 20.608 | 57 | 80 | 86.2 | 61.4 |
| | Lixouri | LXRB | NOA-IG | 38.201 | 20.437 | 10 | 561.6 | 425 | 562 |
| | Sami | SMHA | | 38.251 | 20.648 | 29 | 269.1 | 238.7 | 183 |
| **3/2/2014** | Argostoli | ARG2 | EPPO - ITSAK | 38.178 | 20.488 | 17 | 264.3 | 232.1 | 144.9 |
| | Vasilikiades | VSK1 | | 38.412 | 20.562 | 26 | 56.7 | 53.4 | 25.1 |
| | Lixouri | LXR1 | | 38.201 | 20.438 | 7 | 600.9 | 667 | 481.2 |
| | Chavriata | CHV1 | | 38.183 | 20.382 | 11 | 677 | 751 | 509.2 |

Both events triggered several geological and geotechnical secondary effects. Most of these effects were activated after the first event and were reactivated during the second event, one week later (Valkaniotis et al., 2016). It is evident by the spatial distribution of the observed geotechnical failures that the failures recorded after the first event were further evolved due to the second one (EPPO/ITSAK 2014). The western part of Cephalonia Island (Paliki peninsula and the area around Argostoli Bay) suffered the most damages but a few isolated phenomena were also reported at the northern part of the island (EPPO/ITSAK 2014; GEER, 2014; Valkaniotis et al. 2014).

The geotechnical failures caused by both mainshocks involve slope failures, rock-falls, stonewall failures and small landslides. Significant effects were also observed along the road network and harbor infrastructures, where extensive cracks and failures were created (Valkaniotis et al., 2014; Theodoulidis et al., 2016). Liquefaction phenomena were not induced by the first mainshock. On the contrary, during the second event severe failures and extended liquefaction phenomena occurred at the Lixouri port as well as at the Argostoli port, but on a smaller scale (Lekkas et al., 2014; Theodoulidis et al., 2016).

### **4.5.2** EXSIM parameters

#### **4.5.2.1** Source parameters

All the parameters concerning the fault orientation, the fault geometry and the focal parameters were obtained from Karakostas et al. (2015) who performed a high-precision relocation of the complete seismic sequence. The slip distribution model that was ultimately selected for the ground motion simulations is the one proposed by Millas (2018) and Millas et al. (2018) with minor modifications after personal communication (Fig. 4.7). The final finite-fault model of this earthquake includes a 20 x 20 km$^2$ fault plane discretized into 1 x 1 km$^2$ subfaults. It should be highlighted that due to the large discrepancy between both the proposed fault and slip distribution models, plenty of trials were performed with different models (Papadopoulos et al., 2014; Sokos et al., 2015) in order to determine which one better fits the observed data.

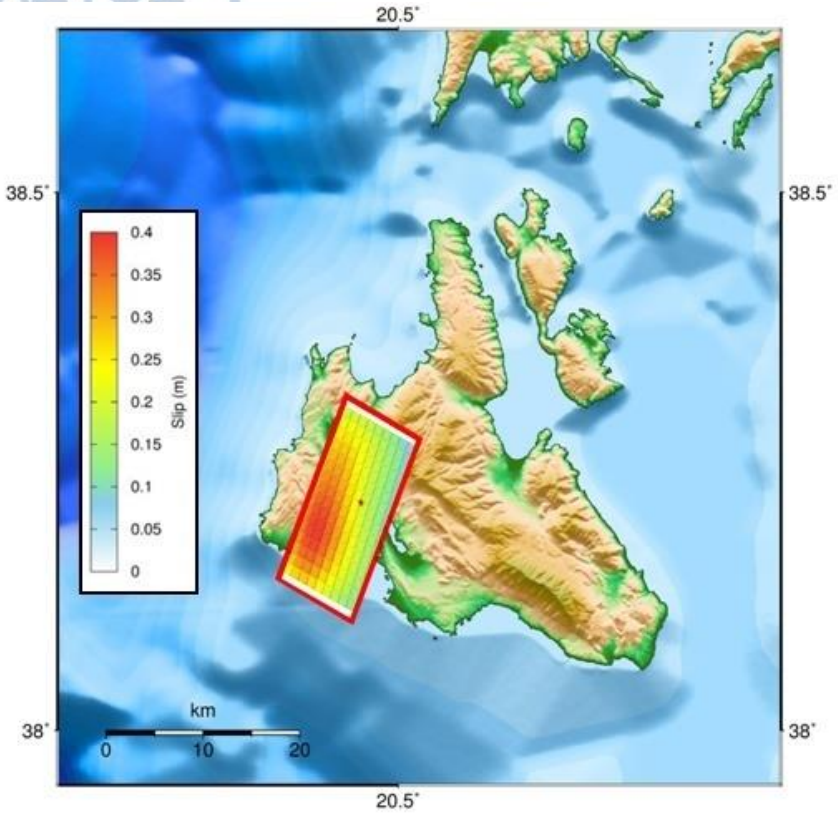


**Figure 4.7:** The slip distribution model (Millas, 2018; Millas et al., 2018) used in the simulations. The red rectangle represents the fault projection on the earth's surface and the red star denotes the epicenter of the earthquake.

The parameters describing the properties of the crustal model, such as the crustal density (rho) and the shear wave velocity (beta) in the vicinity of the source were obtained by Papazachos (1990). The stress parameter ($\Delta\sigma$) was initially set at the mean value of 56 bars computed by Margaris & Hatzidimitriou (2002). However, the visual comparison of simulated and observed Fourier amplitude spectra (FAS) and the direct comparison of simulated and observed PGA from the available recordings indicated that such high recorded PGA values could not be reached. Considering the fact that the general shape of the simulated spectra was comparable to the observed ones and the other input parameters were well constrained, it was concluded that the increase of the stress parameter was necessary. For this reason, a trial-and-error approach was adopted, which resulted in the use of $\Delta\sigma$ = 150 bars, a value that proved to provide a satisfactory comparison between the simulated and the observed acceleration Fourier spectra.

**4.5.2.2** Path properties

Regarding the geometric attenuation, a geometric spreading operator of $R^{-1}$ was applied for distances up to a transition distance of 40 km, beyond which $R^{-0.5}$ was applied, taking into account that the lower exponent at largest distances represents the transition to surface-wave spreading (Atkinson & Assatourians, 2014).

The anelastic attenuation was represented by the Q function given by Boore (1984) (eq. 5.1) which is in good agreement with later studies examining Q in Greece (Hatzidimitriou et al., 1993; Hatzidimitriou, 1995).

$$Q = 275(f/0.1)^{-2.0} \quad f \leq 0.2$$

$$Q = 88(f/1.0)^{0.9} \quad f \geq 0.6 \qquad (5.1)$$

Q values for frequencies between 0.2 and 0.6 Hz are determined from power-law fit to values of Q at f = 0.2 and f = 0.6 Hz.

**4.5.2.3** Site amplification

In an effort to represent the near-surface attenuation at high frequencies, the simulated acceleration spectral amplitudes were diminished by the factor $\exp(-\pi\kappa_0 f)$ as indicated previously. The spectral decay factor kappa ($\kappa_0$) was set as 0.035 which corresponds to rock (class B) site condition (Margaris & Boore, 1998). Then, the appropriate empirical attenuation factors for this soil type were integrated (Table 5.2) as suggested by Margaris & Boore (1998).

The complete set of parameters used for the stochastic simulation of the 26$^{th}$ January 2014 earthquake is summarized in Table 4.3.

**Table 4.2:** Empirical attenuation factors for soil type B (EC8) proposed by Margaris & Boore (1998).

| f (Hz) | Amplification |
|---|---|
| 0.11 | 1.309 |
| 0.16 | 1.3229 |
| 0.3 | 1.3709 |
| 0.46 | 1.4316 |
| 0.79 | 1.5733 |
| 1.06 | 1.6795 |
| 1.25 | 1.7377 |
| 1.54 | 1.8174 |
| 1.76 | 1.8692 |
| 2.07 | 1.9337 |
| 2.55 | 2.0197 |
| 3.42 | 2.1513 |
| 4.94 | 2.3258 |
| 7.24 | 2.5332 |
| 9.2 | 2.6685 |
| 15.72 | 2.9683 |
| 23.49 | 3.1921 |
| 30.42 | 3.3262 |
| 45.38 | 3.5247 |

**Table 4.3:** Modeling parameters used for the finite-fault stochastic method application performed with the EXSIM code

| Parameters | Values |
|---|---|
| **Source** | |
| Moment magnitude | 6.1 |
| Fault area | 20 x 20 km² |
| Fault geometry | Strike = 20°, Dip = 65° |
| Depth of the fault plane top | 0.5 km |
| Sub-fault Size | 1 x 1 km² |
| Slip Model | Millas (2018); Millas et al. (2018) |
| Stress Parameter | 150 bars |
| Subfault window | Exponential |
| Rupture velocity | 0.8Vs |

| | |
|---|---|
| Rise time | $1/f_0$ (Inverse of sub-fault corner frequency) |
| Pulsing % | 50% |
| **Path** | |
| Geometrical Spreading | $R^{-1.0}$ for 1 < R < 40 km<br>$R^{-0.5}$ for R ≥ 40 km |
| Anelastic Attenuation | $Q = 275(f/0.1)^{-2}$ $f \leq 0.2$ Hz<br>$Q = 88\ (f/1.0)^{0.9}$ $f \geq 0.6$ Hz |
| Crustal shear-wave velocity | 3.4 km/s |
| Crustal density | 2.7 g/cm$^3$ |
| **Site** | |
| Site and Crustal Amplification | Table 4.2 |
| Kappa | 0.035 |

**4.5.3** COMPSYN parameters

The application of the COMPSYN code requires the definition of certain basic parameters to set the proper spatial and time constraints. These parameters contribute to better outline the physical aspects behind the problem and to avoid numerical noise.

The time step for the finite element calculation depends on the maximum frequency and must satisfy the Courant stability criterion. This criterion simply requires that the length of the time step must be less than the minimum P wave travel time across any element of the grid. An approximation of this is given by:

$$dt = 0.15 \cdot \frac{V_s}{f_{max} \cdot V_p} \tag{5.3}$$

where $V_s$ and $V_p$ are the S and P wave velocities, respectively, at the shallowest part of the model.

The total duration of the calculated time series must equal or exceed the sum of the extended source duration and the duration of the Green's functions (eq. 5.4). This serves to avoid any noncausal noise before the hypocentral P wave.

$$t_{max} = t_{rupture} + t_{propagation} \tag{5.4}$$

The earth's crust was modeled as a vertically layered medium in order to account for the considerable changes in density and wave velocity as a function of depth. For this reason, the newly proposed velocity model for the Ionian Islands of Papadimitriou et al. (2017) was adopted (Table 4.4). In the 4th column of Table 4.4 the density for each layer of the model was computed using the equation of Gardner et al. (1974) which relates density to the P wave velocity (eq. 5.5).

$$\rho = 0.31 \cdot V_p^{0.25} \tag{5.5}$$

where $V_p$ is the P-wave velocity measured in m/s.

**Table 4.4:** Velocity model proposed by Papadimitriou et al. (2017). Density values in the 4th column were computed with the Gardner et al. (1974) relationship.

| Upper depth of layer (km) | P-wave velocity (km/s) | S-wave velocity (km/s) | Density (g/cm$^3$) |
|---|---|---|---|
| 0 | 5,850 | 3,145 | 2,71 |
| 1 | 5,870 | 3,156 | 2,71 |
| 2 | 5,980 | 3,215 | 2,72 |
| 6 | 6,235 | 3,352 | 2,75 |
| 8 | 6,490 | 3,489 | 2,78 |
| 9 | 6,525 | 3,508 | 2,78 |
| 11 | 6,560 | 3,527 | 2,78 |
| 13 | 6,580 | 3,538 | 2,79 |
| 21 | 6,625 | 3,562 | 2,79 |
| 28 | 6,700 | 3,602 | 2,80 |
| 40 | 8,000 | 4,301 | 2,93 |

As far as the kinematic parameters are concerned, the slip distribution model of Millas (2018) and Millas et al. (2018) was again used (as in the EXSIM computations) but it was integrated into the appropriate format demanded for the SLIP application. This procedure inevitably demands several assumptions to be performed. A boxcar source time function was defined and considered the same at all points of the fault. The rise time was considered constant at all points of the grid, therefore the rise time variability along the fault plane was not taken into account in this thesis. The rupture was initiated at a predefined hypocenter and the rupture front was considered to move outwards in the radial direction at a constant rupture velocity ($V_r$) of 3 km/s (Papadopoulos et al., 2014). The rupture time at each node was computed based on the time when the rupture front reaches its position. Moreover, COMPSYN does not account for multiple site

classification scenarios, thus all computations are performed at bedrock sites considering only one propagation model.

## 4.6 2nd case study - The M6.5 Lefkas 2015 earthquake

### **4.6.1** The M6.5 Lefkas 2015 earthquake sequence

The mainshock (Mw = 6.5) occurred on 17 November 2015 (07:10:07 GMT) and is associated with a fault segment along the SW coast of Lefkas Island. The epicenter was determined at 38.664°N, 20.585°E by Papadimitriou et al. (2017) who performed a high-precision relocation of the whole earthquake sequence. The earthquake was felt in an extended area covering the Ionian Islands, Western Greece, Peloponnesus and the South coast of Italy. This is one of the strongest reported earthquakes in Lefkas Island, especially in the instrumental era, compared only to the first mainschock of the 1948 doublet, which also ruptured the SW part of the Island (Papadimitriou et al., 2017).

All available determined focal mechanisms exhibit a right-lateral strike-slip fault striking NNE-SSW, parallel to the west coast of Lefkas, in agreement with the orientation of the KTFZ (Papadimitriou et al., 2015; Ganas et al., 2016; Sokos et al., 2016; Papadimitriou et al., 2017). The GCMT solution for the mainshock reveals a plane striking at 16°, dipping 64° to the ESE, with a rake of 179°. The double difference location technique conducted by Papadimitriou et al. (2017) revealed the simultaneous activation of other well-defined fault planes, along with the main rupture, with different strike and either west or east dipping. This is an indication of the activation of secondary and adjacent fault segments rather than of a single main fault exclusively releasing the total strain energy.

Sokos et al. (2016) stated that the mainshock is part of an asperity break which had not ruptured since the strong main event of the (Mw = 6.2) 2003 earthquake sequence (e.g. Karakostas et al., 2004; Papadimitriou et al., 2006; Karakostas & Papadimitriou, 2010; Kassaras et al., 2015). This observation is of high significance since it provides indications that the established KTFZ segmentation, which extends parallel to the west coast of Lefkas, should possibly be settled closer to the islands than previously considered.

Similar remarks were made by Chousianitis et al. (2016) who applied joint inversion of seismological and geodetic data alongside GPS displacements. Their proposed slip model unveiled the division of the LS of the transform zone into two segments, the sub-segment in the north, which accommodated the major event of the

2003 doublet and the one in the south that remained unbroken during the 2003 sequence, where the 2015 mainshock occurred.

The main event of 17 November resulted in a rich afterschock sequence consisting of over 2600 events up to 3 December 2015. According to Papadimitriou et al. (2017) the aftershock spatial distribution can be distinguished in three main clusters (Fig. 4.8). The first cluster is located north of the mainshock epicenter demonstrating high aftershock density. The central cluster indicates a distribution of epicenters that coincides with the strike of the mainshock CMT solution. The third one, located in the offshore area between Lefkas and Cephalonia Islands, manifests a NE-SW epicentral alignment, similar to the one of the first cluster. Ganas et al. (2016) and Papadimitriou et al. (2015) recognized two main aftershock clusters, a northern cluster containing shallower hypocenters, between 5 and 10 km and a southern cluster with focal depths ranging between 8 and 15 kilometers which can be divided in smaller sub-clusters.

Two deaths and eight injuries were reported along with damage in buildings and infrastructure. Overall, the damage caused by the mainshock was significantly lower compared to the 2003 event, which suggests that the buildings displayed significant resilience. It is also worth noting the good structural performance of the traditional anti-seismic architecture, with dual structural system, of Lefkas Island (Kazantzidou-Firtinidou et al., 2016; Kassaras et al., 2018). The majority of the building damage was observed in the SW part of Lefkas Island (Lefkata peninsula). In particular, masonry buildings suffered the most damage, whereas reinforced concrete structures have been slightly affected, showing localized damage close to the epicenter area (Kazantzidou-Firtinidou et al., 2016).

A plethora of geological effects were triggered by the mainshock. These effects, mainly concentrated in the western part of Lefkas Island, are ground cracks, slope failures (rock-falls and landslides) and liquefaction phenomena. The rock-falls and landslides were related to pre-existing geotechnically unstable zones which were previously identified as susceptible to landslides (Papathanassiou et al., 2013). The observed ground cracks were of secondary origin and were created by the ground shaking. Regarding the liquefaction phenomena, they were concentrated in the southern part of the island, along the coastal zone between Vassiliki and Ponti. (Papathanassiou et al., 2017; Lekkas et al., 2018).

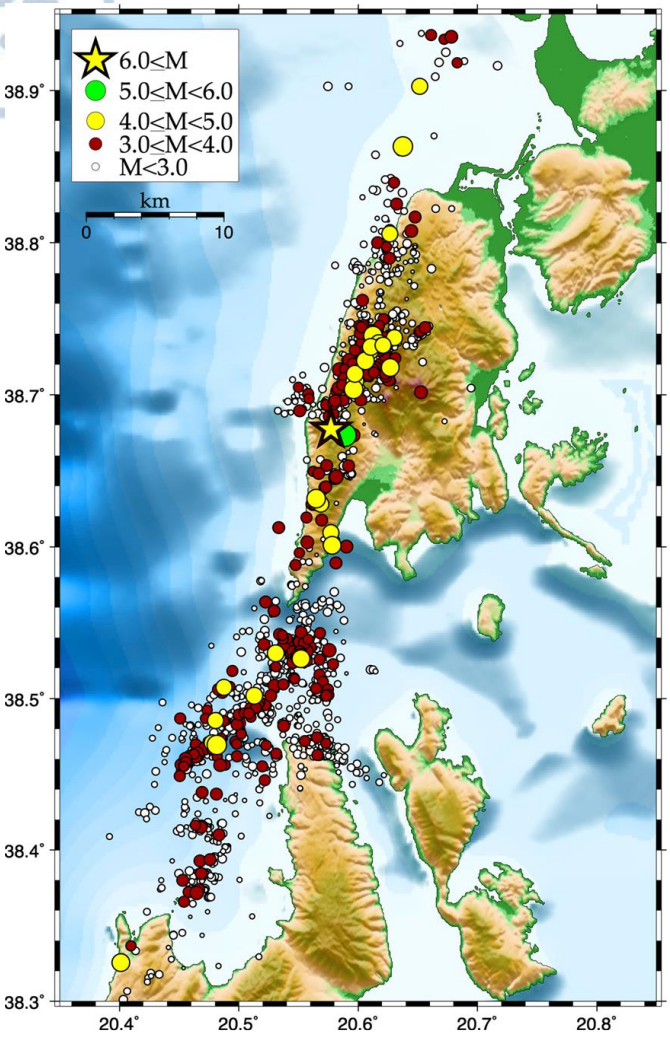


**Figure 4.8:** Relocated aftershock activity of the 2015 sequence after Papadimitriou et al. (2017). The yellow star represents the main shock epicenter and the aftershocks are depicted with different symbols according to their moment magnitude.

According to the National Accelerometric Network of ITSAK-EPPO (Fig. 4.9) the highest value of peak ground acceleration was recorded in Vasiliki (0.36 g), whereas a value of 0.1 g was recorded in the Town of Lefkas. In Table 5.6 the recorded PGA values of the nearest accelerographs of the network, are presented.

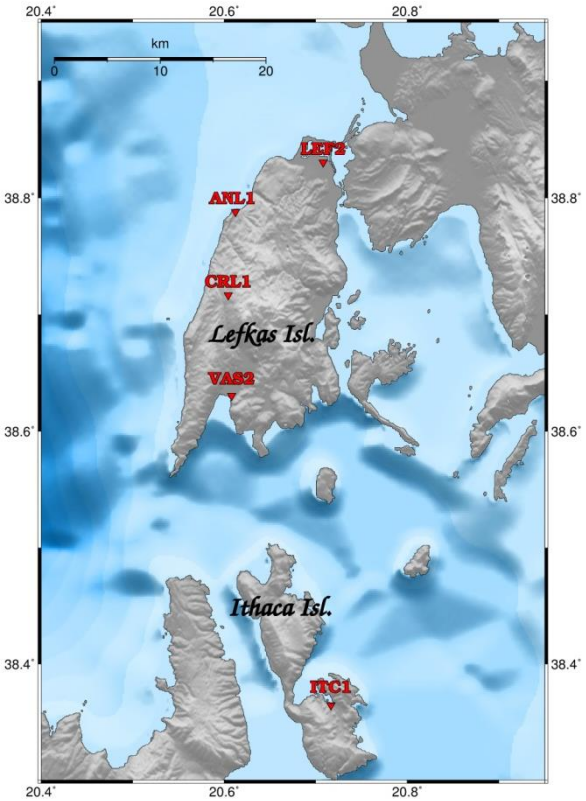


**Figure 4.9:** Locations of the accelerometric stations providing the strong motion data for the 17th November mainshock.

**Table 4.5:** Recorded PGA values for the Lefkas (Mw = 6.5) 17th November 2015 earthquake.

| Location | Code | Owner | Epic. Distance (km) | PGA (N - S) (cm/s²) | PGA (E - W) (cm/s²) | PGA (Z) (cm/s²) |
|---|---|---|---|---|---|---|
| Chortata | CRL1 | EPPO - ITSAK | 2 | 410 | 338 | 403 |
| Vassiliki | VAS2 | | 4 | 363 | 226 | 256 |
| Agios Nikitas | ANL1 | | 13 | 140 | 224 | 90 |
| Lefkas Town | LEF2 | | 21 | 102 | 86 | 55 |
| Ithaca | ITC1 | | 31 | 117 | 79 | 45 |

### **4.6.2** EXSIM parameters

#### **4.6.2.1** Source parameters

The parameters related to the fault orientation, fault dimensions and the slip distribution model of the mainshock were obtained from the work of Chousianitis et al. (2016) (Fig. 4.10). This obtained slip model resulted from the combination of four different seismic and geodetic data sets. The methods used were the joint inversion of near-source static and dynamic GPS displacements, strong motion and teleseismic waveforms. The fault model suggested by Chousianitis et al. (2016) was discretized into 2 x 1.5 km² subfaults and the rupture initiation point was set at 38.665°N, 20.600°E at a depth of 11 km according to the revised solution of the Geodynamic Institute of the National Observatory of Athens. The focal parameters (strike = 24°, dip = 80°) were obtained from the moment tensor solution of Zahradnik & Sokos (2015) which were also used by Chousianitis et al. (2016). This focal mechanism is consistent with other published ones, such as the one proposed by Papadimitriou et al. (2015) (strike = 22°, dip = 72°) or by Ganas et al. (2016) (strike = 18°, dip = 71°).

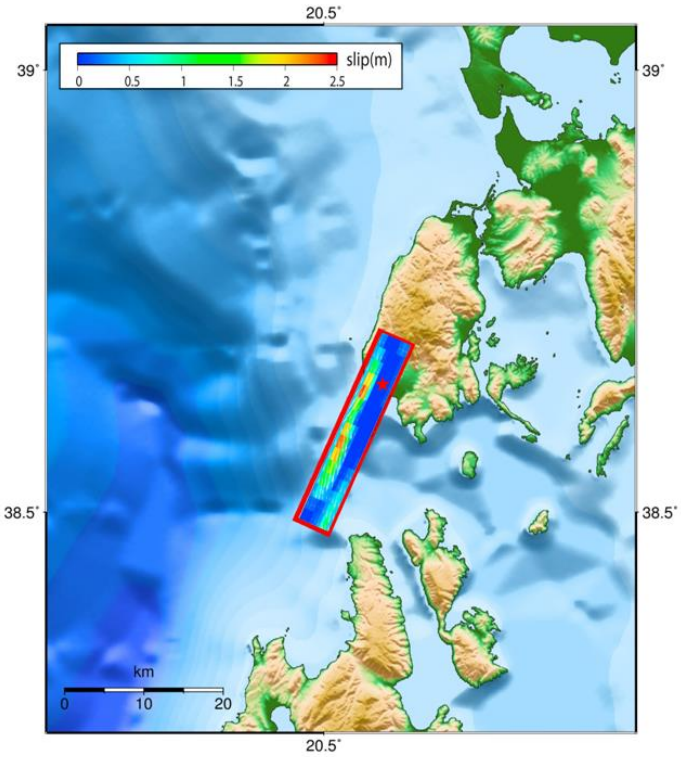


**Figure 4.10:** The slip distribution model (Chousianitis et al., 2016) used in the simulations in the present study. The re rectangle indicates the fault projection on the earth's surface and the red star denotes the epicenter position.

It is worth noting that other slip distribution models, such as the models proposed by Sokos et al. (2016) and Avallone et al. (2017) were also evaluated before it was concluded that this model performs better among the other ones, for this earthquake. The selection of the appropriate slip model was achieved through the comparison of the synthetic with the recorded acceleration spectra. The differences between all these slip models are mostly related to the peak slip values computed and not with the distribution of slip on the surface of the fault which seems similar.

The stress parameter ($\Delta\sigma$) was set at the value of 56 bars computed by Margaris & Hatzidimitriou (2002). Different stress parameter values were also tested but this a priori estimation proved to provide a sufficient comparison of the simulated and the observed acceleration Fourier spectra.

**4.6.2.2** Path properties and site amplification

These parameters were set exactly the same, as in the first case study of the 26$^{th}$ January 2014 mainshock since these two regions are adjacent and considered as seismotectonically homogeneous. The geometric attenuation was represented with an operator of $R^{-1}$ for distances up to 40 km, beyond which $R^{-0.5}$ is used. The Q function published by Boore (1984) (eq. 5.1) was employed to account for the anelastic attenuation. The simulations were performed assuming uniform rock (class B) site condition. For this reason, the spectral decay factor ($\kappa_0$) was set at 0.035 adopted from Margaris & Boore (1998) and the corresponding empirical attenuation factors for this soil type (Table 5.2). The complete set of parameters used for the stochastic simulation of the 17$^{th}$ November 2015 mainshock is summarized in Table 4.6.

**Table 4.6:** Modeling parameters used for the finite-fault stochastic method application performed with the EXSIM code.

| Parameters | Value |
|---|---|
| **Source** | |
| Moment magnitude | 6.5 |
| Fault area | 28 x 15 km$^2$ |
| Fault geometry | Strike = 24$^o$, Dip = 80$^o$ |
| Depth of the fault plane top | 0.66 km |
| Sub-fault Size | 2.0 x 1.5 km$^2$ |

| | |
|---|---|
| Slip Model | Chousianitis et al. (2016) |
| Stress Parameter | 56 bars |
| Subfault window | Exponential |
| Rupture velocity | 0.8Vs |
| Rise time | $1/f_0$ (Inverse of sub-fault corner frequency) |
| Pulsing % | 50% |
| **Path** | |
| Geometrical Spreading | $R^{-1.0}$ for 1 < R < 40 km<br>$R^{-0.5}$ for R ≥ 40 km |
| Anelastic Attenuation | $Q = 275(f/0.1)^{-2}$ f ≤ 0.2 Hz<br>$Q = 88\ (f/1.0)^{0.9}$ f ≥ 0.6 Hz |
| Crustal shear-wave velocity | 3.4 km/s |
| Crustal density | 2.7 g/cm$^3$ |
| **Site** | |
| Site and Crustal Amplification | Table 4.2 |
| Kappa | 0.035 |

### **4.6.3** COMPSYN parameters

The earth's crust model implemented in the Lefkas case study is exactly the same as in the first case study. The velocity model for the Ionian Islands of Papadimitriou et al. (2017) was employed (Table 5.5) along with the crustal density values derived from the empirical relationship of Gardner et al. (1975). In addition, the basic parameters that need to be defined in order to set the spatial and time constraints were set in the same way as in section 4.5.3. The slip distribution model of Chousianitis et al. (2016) was modified in order to employ the same source geometry as applied in the HF simulations performed with EXSIM. A boxcar source time function was adopted, having a constant rise time, and was considered the same all over the fault surface. In order to complete the kinematic parameters used in COMPSYN, the hypocenter position was fixed and the rupture fronts were considered to travel outwards with a constant rupture velocity ($V_r$) of 2.5 km/s, as determined by Chousianitis et al. (2016). Following this theoretical assumption, the rupture times of each grid node on the fault surface were determined based upon the time when the rupture front reaches its position. Finally, all computations were carried out for bedrock site condition (class B) considering a single propagation model.

# Chapter 5 - Broadband ground motion simulation results

## 5.1 Broadband ground motion simulation results for the 1st case study - The Cephalonia 26th January 2014 M6.1 earthquake

### 5.1.1 Spatial distribution of simulated ground motions

In an effort to better assess the ground motion variability caused by the 26th January earthquake, a normal grid was superimposed on the area encompassed between 38.04°N - 38.52°N and 20.36°E - 20.84°E with the nodes of the grid at a spacing of 0.02°. Synthetic records of acceleration for each node were simulated, assuming uniform soil B type (EC8) to account for the local site condition. Figure 5.1 shows the spatial distribution of PGA values which reflects mainly the source effect given that the soil condition is assumed to be uniform. Regarding the absolute PGA values, they contain the effect of local site condition along with the uncertainty related to the mean soil condition assumption that was necessary in the simulations.

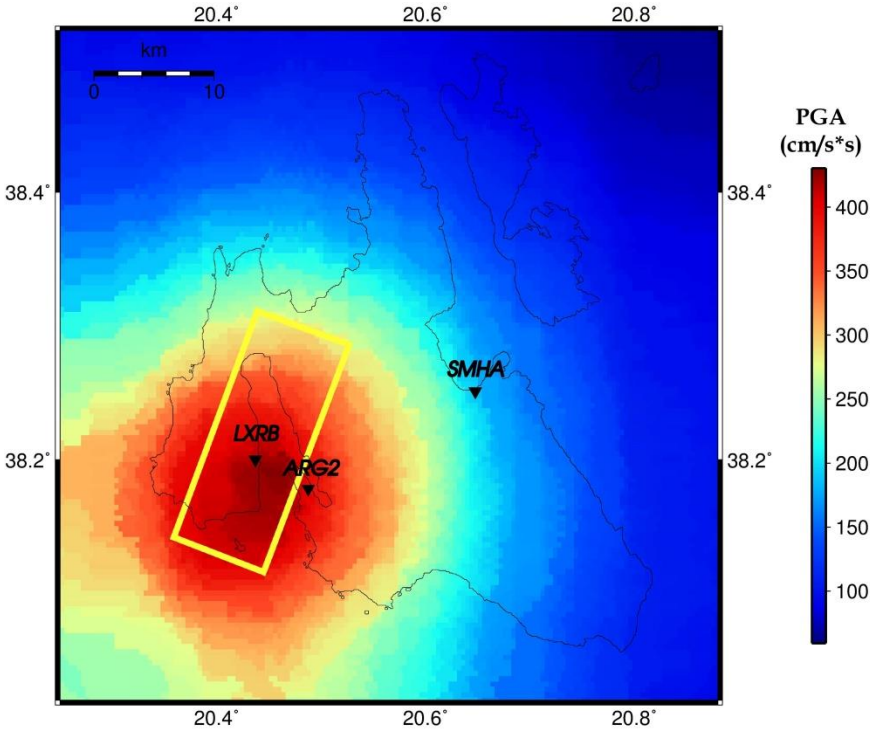


**Figure 5.1:** Spatial distribution of simulated PGA values using the EXSIM code for the 26th January 2014 mainshock.

The PGA distribution (Fig. 5.1) shows that the strongest ground shaking took place in the vicinity of the area around the main slip asperity of the activated fault (Fig. 4.7). This validates the assumption supported by Irikura & Miyake (2011) that slip heterogeneity within the source influences the strong ground motion rather than the average slip in the entire rupture area. The simulated PGA spatial distribution is in agreement with the spatial distribution of damage and other earthquake-induced geological effects as well as with the macroseismic intensity maps (e.g. Papadopoulos et al., 2014; Valkaniotis et al., 2014). However, the computed PGA value at Lixouri is underestimated compared to the recorded one. This deviation can be explained by the fact that the LXRB station is very close to the surface projection of the activated fault, therefore it is considerably more affected by source complexity and other near-source effects. Finally, as it was expected, with the increase of distance from the fault trace, the influence of slip distribution diminishes which leads to a decrease in ground motion variability.

### **5.1.2** Comparison of simulated ground motions with GMPEs

In order to compare the simulated ground motion obtained using EXSIM, the GMPEs of Bindi et al. (2007) and Akkar & Bommer (2010) were used. The former is derived from the Italian strong motion database (ITACA) whereas the latter from recordings in Turkey, Italy and Greece and can be used for crustal earthquakes in southern Europe and the Middle East region. Unfortunately, until today there is no available established GMPE purely from Greek records (See section 2.5) that uses the Joyner & Boore distance. This is attributed to the fact that in regions such as Greece and Italy the surface geology rarely exhibits any evident faulting, thus, it is impossible or unstable to use a fault distance definition (Margaris et al., 1998).

In Figure 5.2 the 57 horizontal PGA values recorded from the stations of the HUSN are plotted up to 150 km as a function of the Joyner & Boore distance and compared with both the values derived from the empirical regressions predicted by the selected GMPEs and the simulated peak ground acceleration for 696 dummy stations using the EXSIM code. The GMPEs are obtained for strike-slip faulting style and type B soil condition.

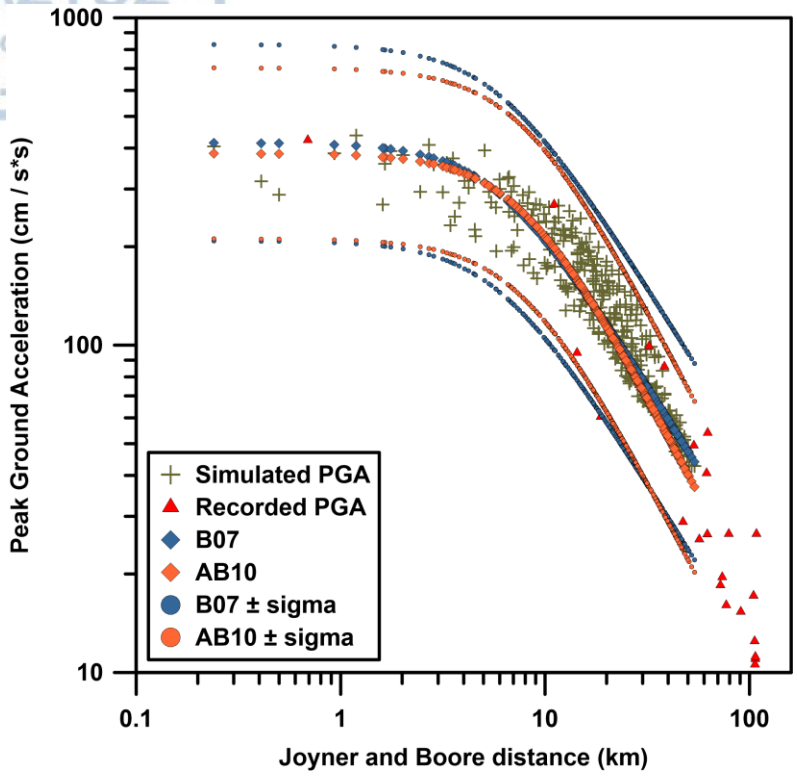


**Figure 5.2:** Comparison between the recorded (triangles), GMPE-derived (diamonds) and simulated (crosses) PGA values.

It is apparent that there is a lack of recordings in the near field, since the vast majority of recorded PGAs are at distances over 20 kilometers. As it can be seen from Figure 5.2, the simulated PGA values generally show good agreement for the entire distance range, although it is almost impossible to sufficiently assess the variability in smaller $R_{jb}$ distances were less data are available.

To better assess the level of fit between the PGA values obtained from the stochastic simulations ($PGA_{syn}$) and the ones derived from the GMPEs ($PGA_{GMPE}$) the residuals were calculated by the equation (5.2).

$$R = \ln(PGA_{syn}) - \ln(PGA_{GMPE}) = \ln\left(PGA_{syn} / PGA_{GMPE}\right) \quad (5.2)$$

The ground motion variability is illustrated (Fig. 5.3) with respect to the $R_{jb}$ distance from the fault.

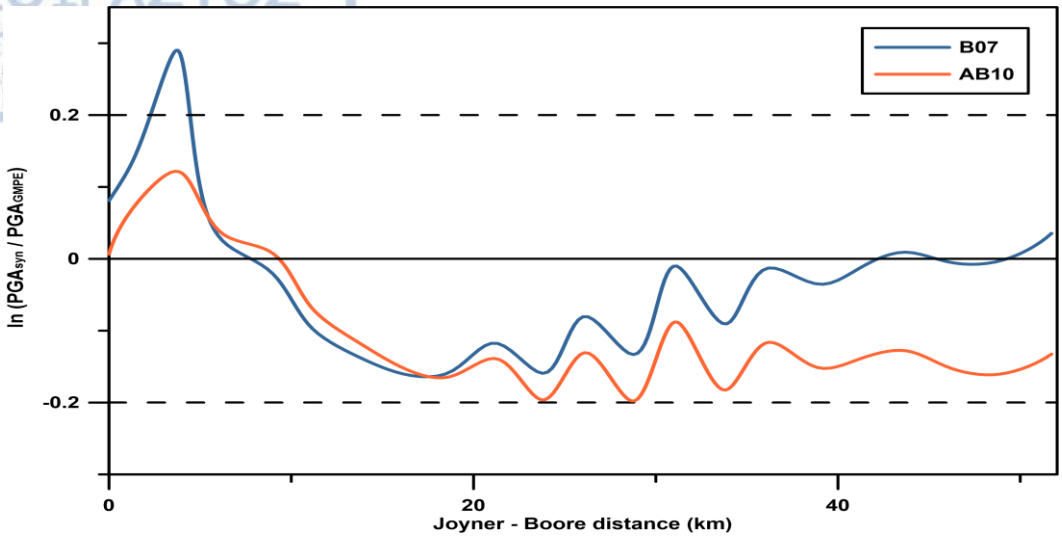


**Figure 5.3:** Residuals between the simulated PGA values and the PGA values obtained from the use of B07 and AB10 GMPEs, plotted as functions of Joyner & Boore distance.

Figure 5.3 evinces that the overall variability is placed inside the ±1 sigma range of the GMPEs. All residuals from the AB10 relationship (red line) are contained in a standard deviation of ± 0.2σ, which falls within the ± 1 sigma bound of AB10. The B07 residuals on the other hand, are also in the same range, apart from a spike in the near field (2-6 km) were they reach 0.3σ. This means that in this limited part, an overestimation of the simulated PGA values is observed. This can be attributed partly to the lack of sufficient near fault strong motion data which has an impact in the development of the GMPEs and their applicability in the near field. In the same context, it is evident that the variability decreases with the increase of distance from the fault trace because of the gradual reducing influence of the slip distribution in the far field.

### **5.1.3** Comparison of synthetic and observed Fourier amplitude spectra

In order to validate the computed synthetic time series, four accelerograms from the strong motion networks of ITSAK and NOA-IG were used for comparison (Table 5.1). These recordings contain the highest PGA values observed for the 26$^{th}$ January mainshock and they come from the closest seismic stations to the epicenter.

**Table 5.1:** The closest seismic stations to the epicenter of the 26th January 2014 mainshock.

| Location | Code | Organization | Epicentral Distance (km) | Max PGA (g) |
|---|---|---|---|---|
| Lixouri | LXRB | NOA-IG | 10 | 0.57 |
| Argostoli | ARG2 | ITSAK | 13 | 0.43 |
| Sami | SMHA | NOA-IG | 29 | 0.27 |
| Vasilikades | VSK1 | ITSAK | 34 | 0.10 |

As shown in Figure 5.4, the simulations provide reasonable estimates of the general shape and amplitudes of the spectra for the selected stations. As previously mentioned, in this stage of the analysis, the comparison concerns the HF part (>2 Hz) of the spectra, as the LF part will be integrated in forthcoming stages.

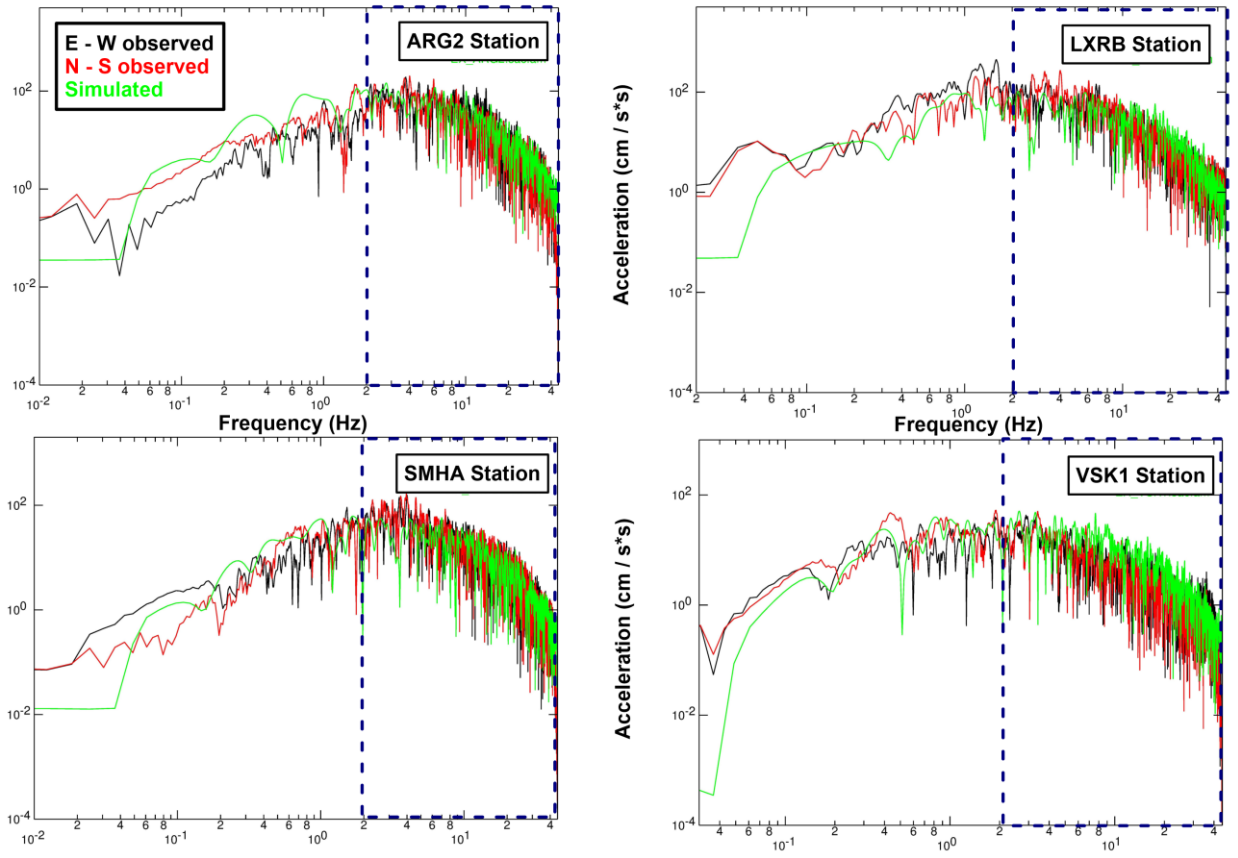


**Figure 5.4:** Comparison between the simulated (green) and the recorded (black and red) FAS of the four closest seismic stations to the epicenter. The dashed rectangles delineate the frequency band of interest.

**5.1.4** Merging the HF synthetics with LF synthetics

The hybrid broadband simulation results are presented along with the actual recorded data in Figures 5.5 - 5.8 It must be pointed out that the synthetic FAS and waveforms are not expected to completely match with the available strong motion records. The aspects examined in order to determine whether the simulations are comparable with the real data are the duration of the signals, their pulselike character and their frequency content.

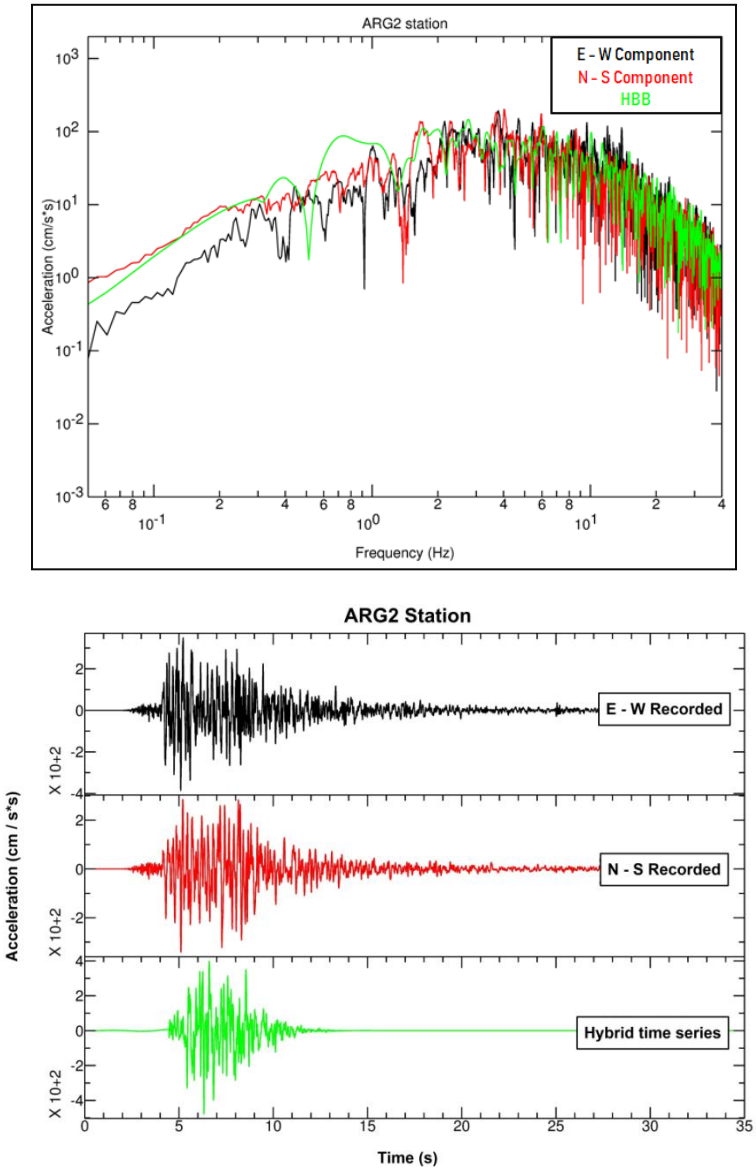


**Figure 5.5: a)** Frequency Amplitude Spectra of the recorded ground motions (E-W component in black, N-S component in red) in comparison with the hybrid broadband simulated spectra (in green) for ARG2 station. **b)** Recorded time series (E-W component in black, N-S component in red) and the hybrid synthetic time series (in green), obtained from the merging of the results of EXSIM (HF) and COMPSYN (LF) for ARG2 station.

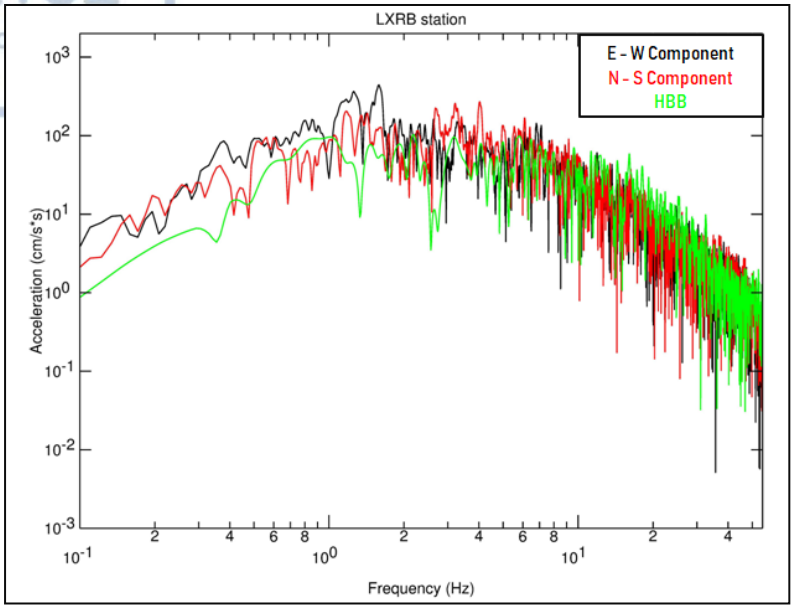


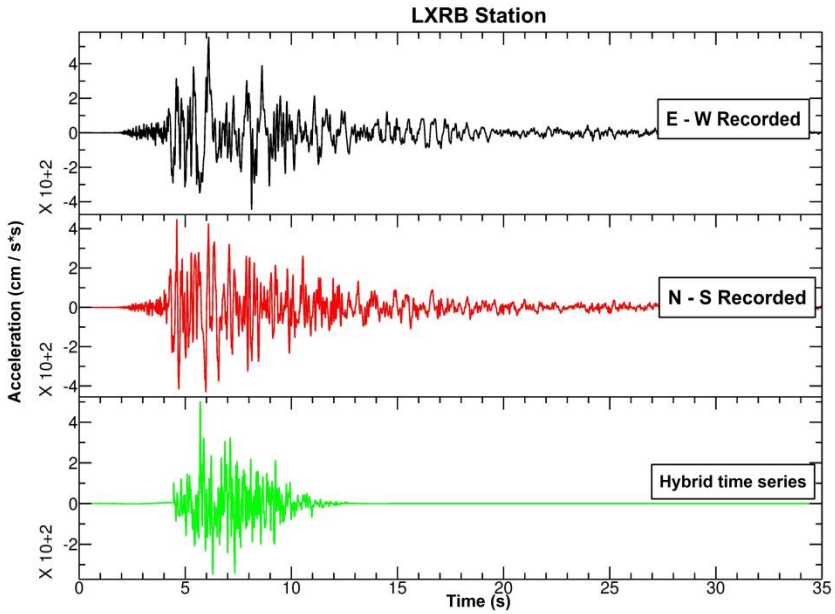


**Figure 5.6: a)** Frequency Amplitude Spectra of the recorded ground motions (E-W component in black, N-S component in red) in comparison with the hybrid broadband simulated spectra (in green) for LXRB station. **b)** Recorded time series (E-W component in black, N-S component in red) and the hybrid synthetic time series (in green) obtained from the merging of the results of EXSIM (HF) and COMPSYN (LF) for LXRB station.

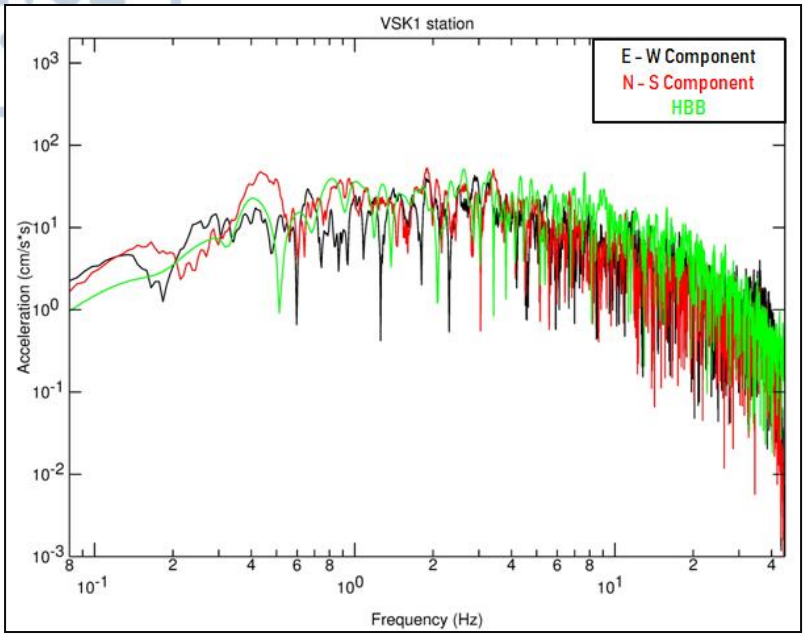


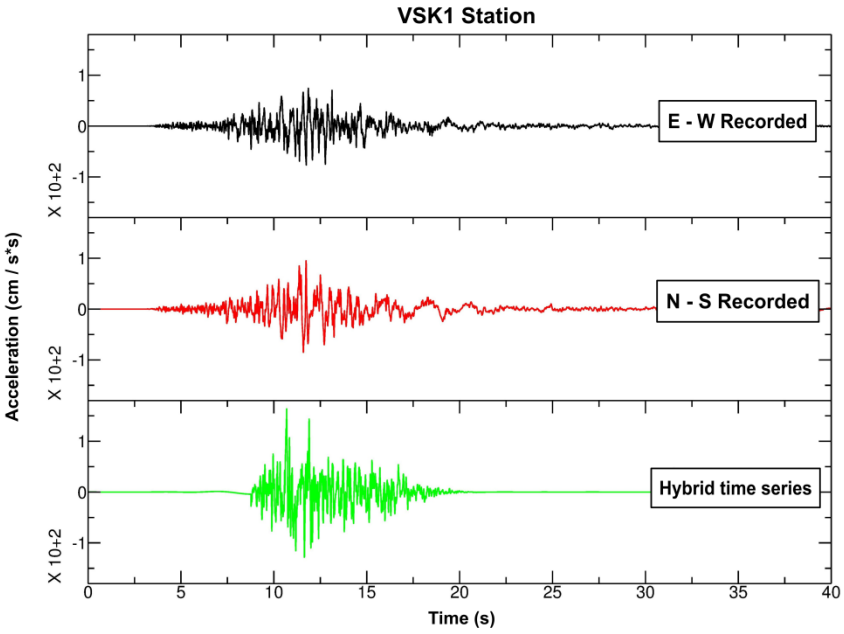


**Figure 5.7: a)** Frequency Amplitude Spectra of the recorded ground motions (E-W component in black, N-S component in red) in comparison with the hybrid broadband simulated spectra (in green) for VSK1 station. **b)** Recorded time series (E-W component in black, N-S component in red) and the hybrid synthetic time series (in green) obtained from the merging of the results of EXSIM (HF) and COMPSYN (LF) for VSK1 station.

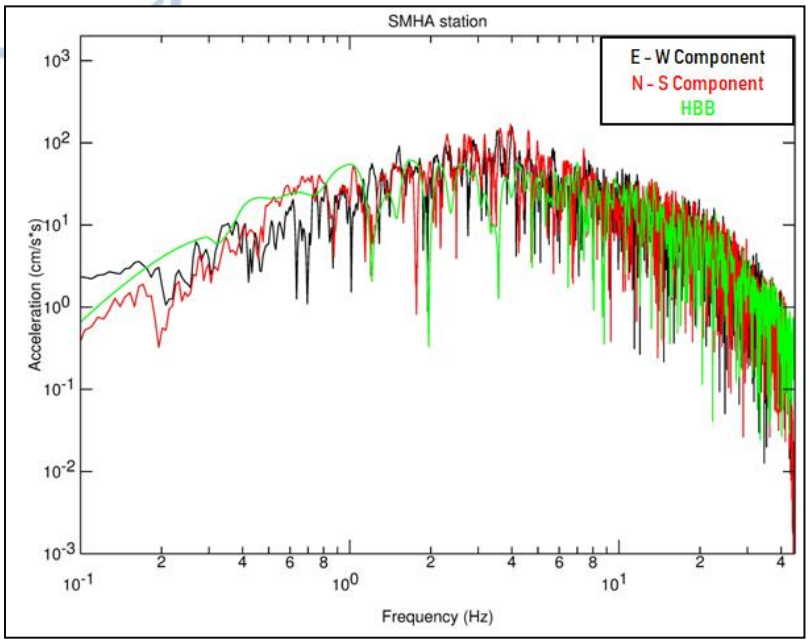


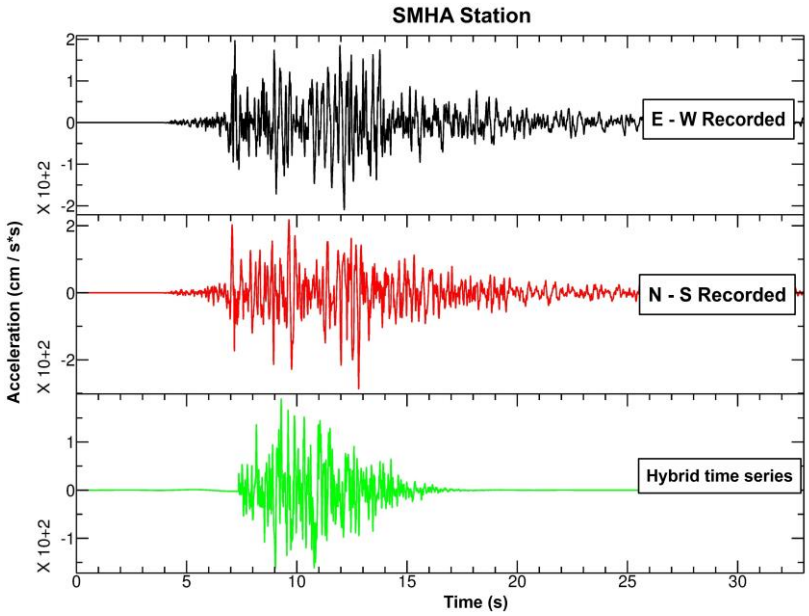


**Figure 5.8: a)** FAS of the recorded ground motions (E-W component in black, N-S component in red) in comparison with the hybrid broadband simulated spectra (in green) for SMHA station. **b)** Recorded time series (E-W component in black, N-S component in red) and the hybrid synthetic time series (in green) obtained from the merging of the results of EXSIM (HF) and COMPSYN (LF) for SMHA station.

The comparison of the hybrid synthetics with the recorded data reveals a satisfactory fit both in amplitudes and phases. The simulated PGA values are very close to the level of the recorded ones. The general shape of the simulated spectra matches very well the recorded ones in the whole frequency band, which that was a key objective of this study. However, the duration of the simulated time series seems to be slightly decreased compared to the recorded ones especially as the epicentral distance increases. This can be attributed to the reflected waves that reach the more distant stations and add further complexities to the case study. More specifically, the simulated PGA values for LXRB (0.51g) and ARG2 (0.48g) stations are in close proximity with the recorded ones (0.57g and 0.43g respectively). The same applies also to the more distant stations VSK1 (0.16g) and SMHA (0.19g) where the recorded PGA (0.1g and 0.27g accordingly) is in direct proximity.

## 5.2 Broadband ground motion simulation results for the 2nd case study - The Lefkas 2015 M6.5 earthquake

### 5.2.1 Spatial distribution of simulated ground motions

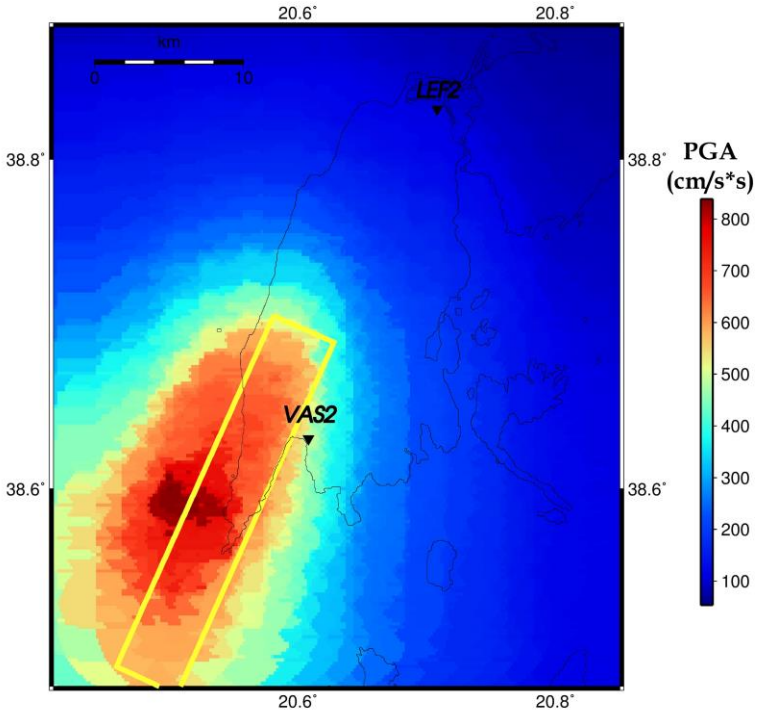


**Figure 5.9:** Spatial distribution of simulated PGA values using the EXSIM code for the 17th November 2015 earthquake.

In an effort to better assess the ground motion variability caused by this earthquake, a grid was generated between 38.52°N - 38.92°N and 20.44°E - 20.84°E divided into 0.02° x 0.02° grid cells. Synthetic records for each point of the grid were simulated, assuming uniform soil B type (EC8) to account for the local site condition. Due to the uniform site classification assumed, the spatial distribution of PGA illustrated in Figure 5.9 reflects mainly the source effect.

Similarly to the first case study, it is highlighted that the main slip asperities (Fig. 5.10) have a major influence on the regions suffering the strongest ground shaking. As shown in Figure 5.9 the simulated PGA values match quite well with the recorded data, however a slight overestimation is observed on the two closest recordings. This could possibly be explained by the site amplification factors used which correspond to soil type B sites and also by the presence of directivity effects (towards the south) (Sokos et al., 2016). Furthermore, the comparison with the obserced damage (and other earthquake-induced phenomena) distribution maps reveals a reasonable agreement with the simulated PGA distribution map. After the evaluation of macroseismic intensity maps (Papathanassiou et al., 2017) it is easily observed that the isoseismal pattern coincides with the one shown in Figure 5.9 especially in the region where the highest simulated PGA values were obtained (SW Lefkas).

### **5.2.2** Comparison of simulated ground motions with GMPEs

The calculated PGA values from the EXSIM code were compared with the synthetic PGA values obtained from the GMPEs of Bindi et al. (2007) and Akkar & Bommer (2010) as a function of Joyner & Boore distance. The GMPEs were used in their appropriate form referring to strike-slip faulting style and type B soil condition. In Figure 5.10 the PGA values predicted by the use of GMPEs, along with their standard deviations, and the simulated ones from EXSIM for 510 dummy stations, are presented.

As it can be seen from Figure 5.10, the simulated PGA values appear to have a matching trend with the ones derived from the GMPEs, particularly in distances over 10 km. Apart from this, in the total Joyner & Boore distance range, the simulated PGA values lie within the plus one and minus one standard deviation area. The differences of the simulated values with the ones derived from the GMPEs cannot (and should not) be assessed for very near-source distances given that the GMPEs were established using a dataset with limited near-source data.

To better assess the level of fit between the PGA values obtained from the stochastic simulations ($PGA_{syn}$) and the ones derived from the GMPEs ($PGA_{GMPE}$) the residuals were calculated as in equation (5.2).

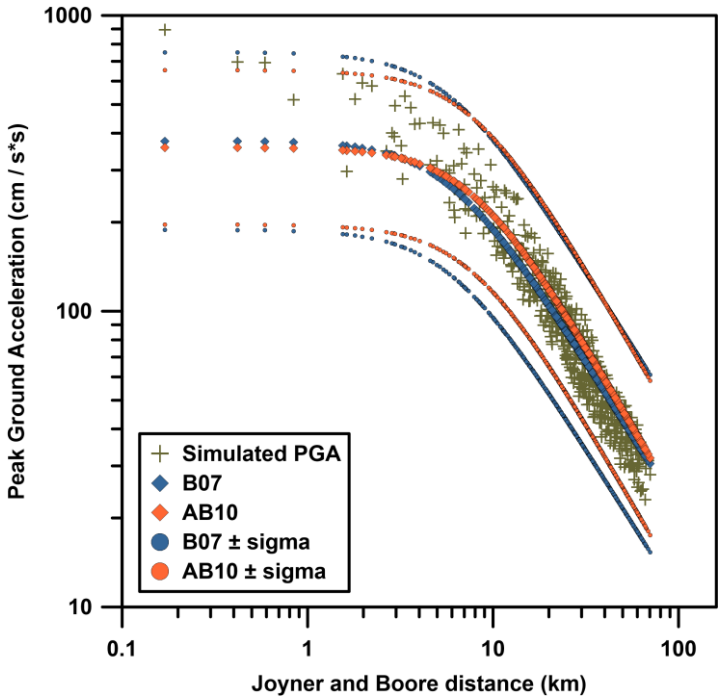


**Figure 5.10:** Comparison between the GMPE-derived (diamonds) and simulated (crosses) PGA values.

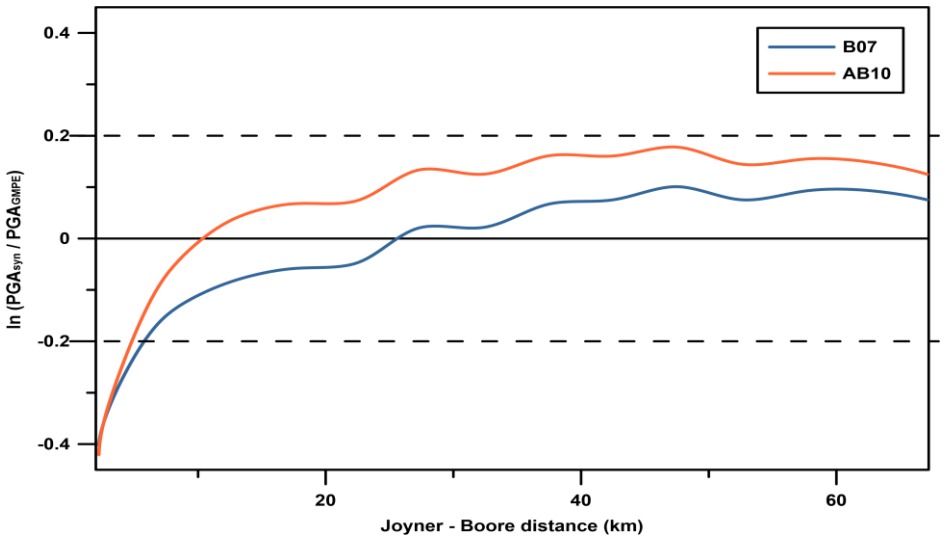


**Figure 5.11:** Residuals between the simulated PGA values and the PGA values obtained from the use of B07 and AB10 GMPEs, plotted as functions of Joyner & Boore distance.

As shown in Figure 5.11, for the largest part, the overall variability lies inside the ± 0.2σ band (dashed lines) which is placed inside the ±1 sigma range of the GMPEs. In the near field though (as in the 1st case study) an increase in the obtained residuals is observed. A possible explanation for this was analyzed in previous section. In any case, the majority of the overestimated synthetic PGA values in the near field that causes this increase belongs to off-shore dummy stations, therefore the comparison with observed PGA values is impossible.

### **5.2.3** Comparison of synthetic and observed Fourier amplitude spectra

For the validation of the synthetic time series, three accelerograms from the strong motion network of ITSAK were used for comparison (Table 5.2). In this particular stage of the analysis, the focus is concentrated on the HF part (> 2 Hz) of the spectra, as the LF portion will be merged in following stages. It is apparent from Fig. 5.12 that the simulations provide realistic estimates regarding the general shape of the spectra as well as their amplitudes.

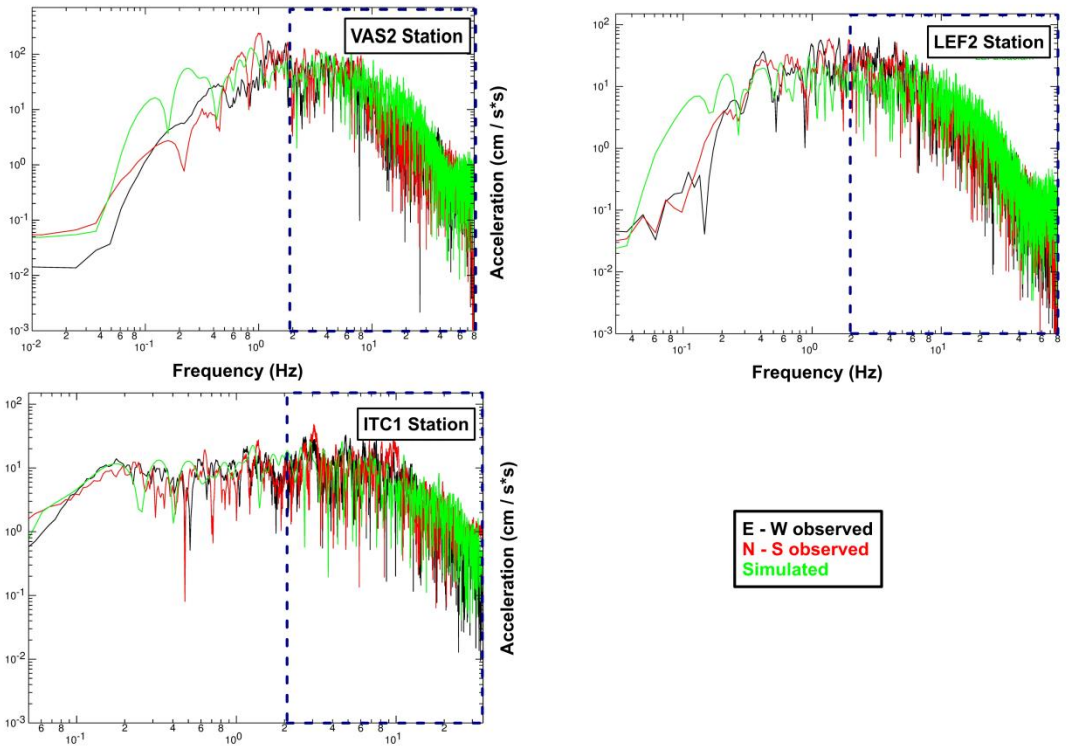


**Figure 5.12:** Comparison between the simulated and the recorded FAS of the three selected seismic stations. The dashed rectangles delineate the frequency band of interest.

Nevertheless, in the station closer to the epicenter (VAS2) the amplitude levels seem to be increased, which can be attributed either to near-source effects that cannot be described in detail in the framework of this study or to local site effects that are not examined.

**Table 5.2:** The closest seismic stations to the epicenter of 17th November 2015 earthquake.

| Location | Code | Organization | Epicentral Distance (km) | Max PGA (g) |
|---|---|---|---|---|
| Vassiliki | VAS2 | ITSAK | 8 | 0,36 |
| Lefkas Town | LEF2 | ITSAK | 21 | 0,10 |
| Ithaca | ITC1 | ITSAK | 35 | 0,12 |

### **5.2.4** Merging the HF synthetics with LF synthetics

The hybrid broadband simulation results are presented along with the recorded data in Figures 5.13- 5.15. Similarly to the first case study, the aspects examined in order to determine whether the simulations are comparable with the real data are the duration of the signals, their pulselike character and their frequency content.

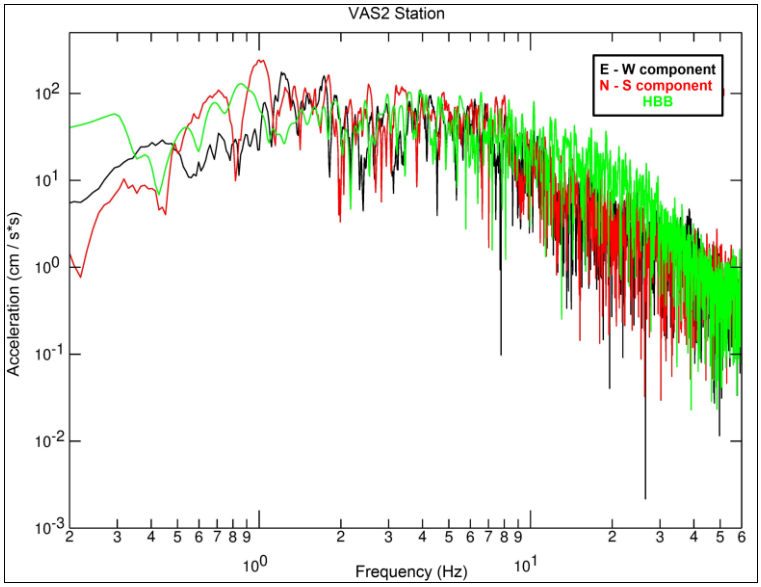

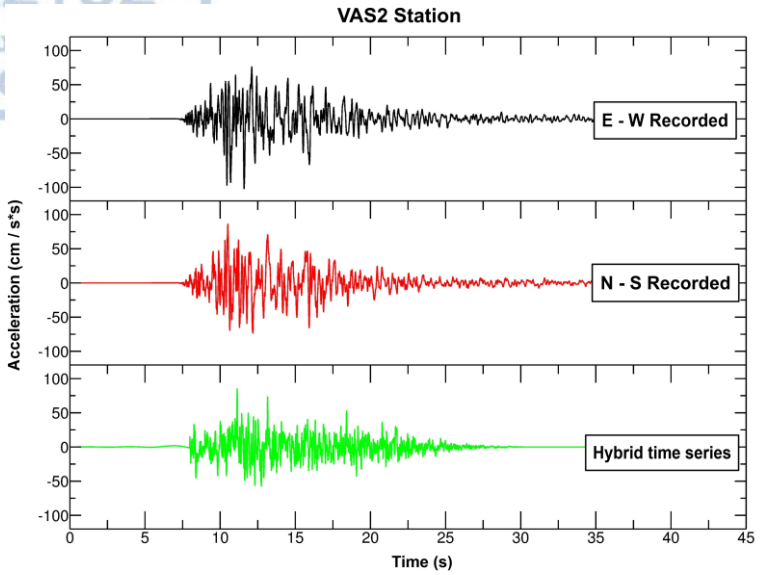


**Figure 5.13: a)** Frequency Amplitude Spectra of the recorded ground motions (E-W component in black, N-S component in red) in comparison with the hybrid broadband simulated spectra (in green) for VAS2 station. **b)** Recorded time series (E-W component in black, N-S component in red) and the hybrid synthetic time series (in green) obtained from the merging of the results of EXSIM (HF) and COMPSYN (LF) for VAS2 station.

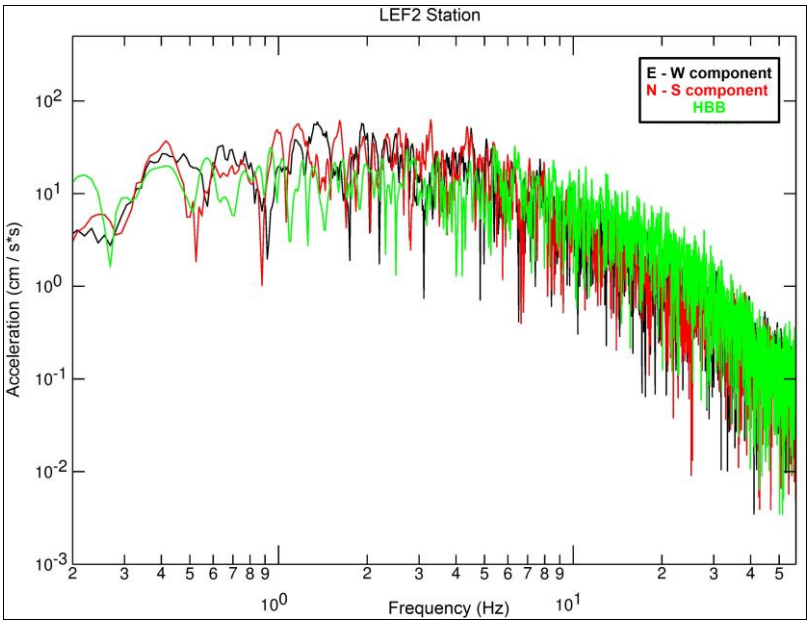

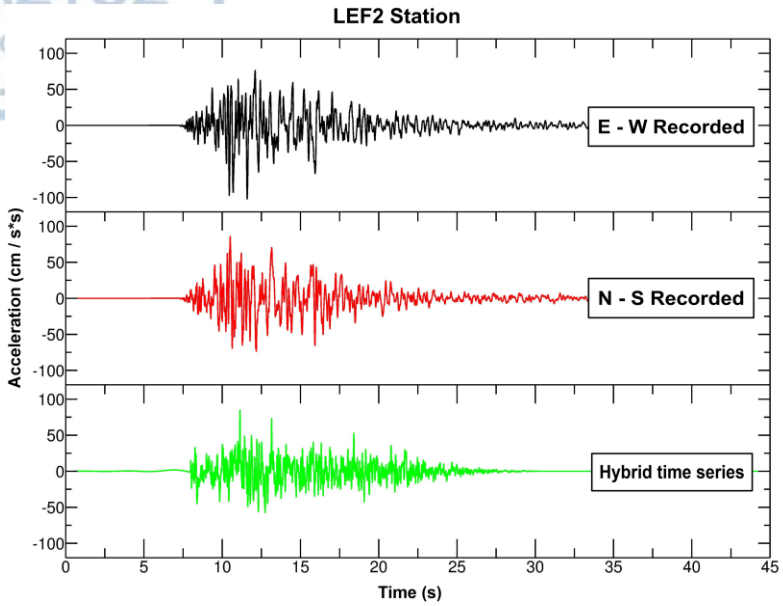


**Figure 5.14: a)** Frequency Amplitude Spectra of the recorded ground motions (E-W component in black, N-S component in red) in comparison with the hybrid broadband simulated spectra (in green) for LEF2 station. **b)** Recorded time series (E-W component in black, N-S component in red) and the hybrid synthetic time series (in green) obtained from the merging of the results of EXSIM (HF) and COMPSYN (LF) for LEF2 station.

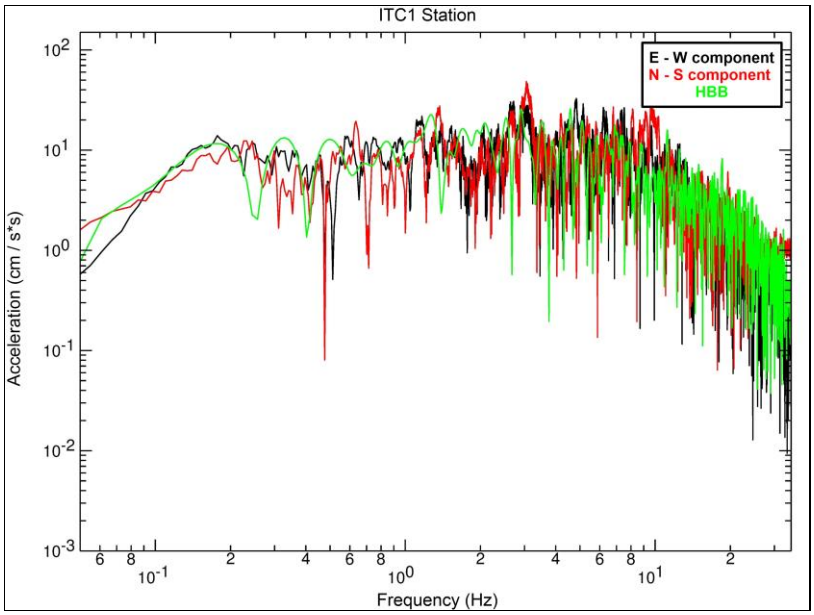

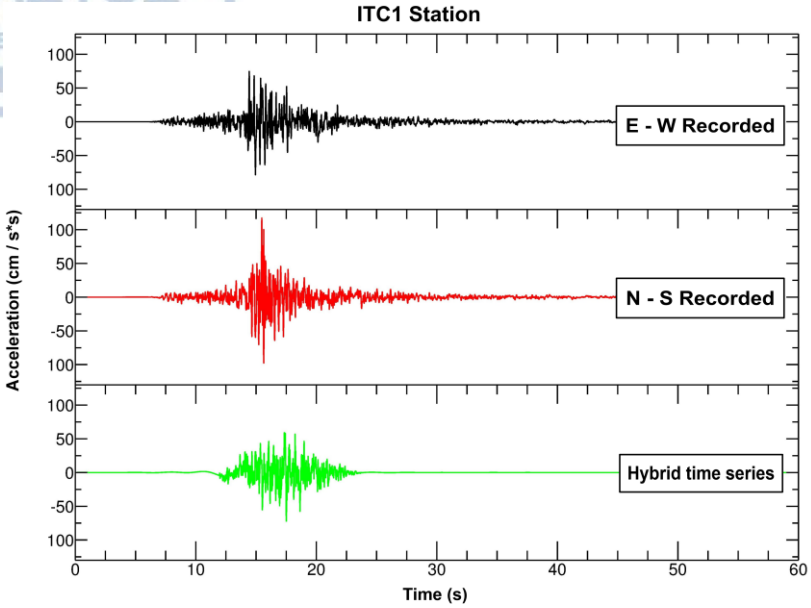


**Figure 5.15: a)** Frequency Amplitude Spectra of the recorded ground motions (E-W component in black, N-S component in red) in comparison with the hybrid broadband simulated spectra (in green) for ITC1 station. **b)** Recorded time series (E-W component in black, N-S component in red) and the hybrid synthetic time series (in green) obtained from the merging of the results of EXSIM (HF) and COMPSYN (LF) for ITC1 station.

The comparison of the hybrid synthetics with the recorded data reveals a satisfactory fit both in amplitudes and phases. The simulated PGA values are relatively close to the level of recorded PGA. More specifically, the PGA values simulated for LEF2 station (0,11g) and ITC1 station (0,11g) and the recorded values (0,10g and 0,12g, respectively) are very close. However, at the closest station to the fault projection (VAS2 station) the simulated PGA values (up to 0,48g) seem to be rather increased than the recorded ones (up to 0,36g). It is very significant to note that among the examined stations, the one that is certainly grounded in rock formations (ITC1) provides the best fit with the simulated data in comparison with other stations that deviate from typical rock type condition sites. Furthermore, the general shape of the simulated spectra fits with the recorded spectra in the whole frequency band, especially at ITC1 station, although the simulated PGA values and the duration of the time series are increased.

# Chapter 6 - Discussion & Conclusions

In the present Master's thesis multiple concepts of engineering seismology are taken into account in an effort to conduct a complete probabilistic seismic hazard analysis for the Central Ionian Islands along with an accurate estimation of strong ground motion for the two strongest earthquakes that took place in this region during the past few years.

The basic steps of the conducted PSHA do not deviate from the original procedure that Cornell (1968) proposed and includes the delineation of SZs where earthquakes follow a recurrence relationship and have the same probability of occurrence at any location, and the assignment of a GMPE to obtain ground motion values related to a specified probability of exceedance (or non - exceedance). In this case, five well-established GMPEs for Greek earthquakes were used. All the created hazard maps outlined Western Cephalonia as the most hazardous region, where values greater than 0.4 g (on average) for a return period of 475 years were determined, corresponding to rock site condition. The rest of the study area demonstrated low to moderate seismic hazard levels. The comparison of the created hazard maps with other related studies revealed that certain GMPEs performed better than others, thus producing more realistic results. Moreover, the computed values from this assessment indicate the need to update the Greek Building Code (Fig. 3.2) since the design values are underestimated.

The accurate simulation of strong ground motion still remains one of the most critical issues in modern seismic hazard studies and engineering seismology in general (Mai, 2009). Reliable broadband strong ground motion simulations can be extremely useful especially for regions with limited availability of strong ground motion data, since they can provide scientists with peak ground motion parameters and their frequency content of scenario earthquakes, in order to fill the gaps of the available seismic data. Apart from this, strong ground motion simulations are valuable as a means to understand the earthquake mechanisms and the characteristics of the media in a certain region. The use of GMPEs could be adequate in some cases, but due to their inefficiency to account for the complexities that take place in the near field, the optimum way to simulate ground motions is to compute broadband synthetic time series.

On that premise, a hybrid broadband simulation approach was applied in this study to simulate ground motions for the 26$^{th}$ January 2014 (Mw = 6.1) Cephalonia and 17$^{th}$ November (Mw = 6.5) Lefkas mainshocks. For frequencies higher than 2 Hz, where source and wave propagation effects become stochastic, a finite fault simulation model based on

a dynamic corner frequency was implemented via the EXSIM code. On the other hand, for the LF part of the synthetic seismograms a deterministic method was employed through COMPSYN, a well-established code to calculate synthetic time series occurring on extended faults by computing Green's functions using the Discrete Wavenumber / Finite Element (DWFE) method of Olson et al. (1984). The results from each simulation method were eventually merged in the frequency domain by using the technique of Mai & Beroza (2003).

The spatial distribution of simulated ground motions (Figures 5.1 & 5.9) reveals that they are highly influenced by the slip heterogeneity within the seismic source rather than by the average slip in the whole ruptured area. Site specific simulated PGA values show good correlation with the maximum recorded PGA values from the HUSN and the isoacceleration maps are supported by macroseismic observations. However, small discrepancies are observed in sites such as LXRB station, which is located very close to the surface projection of the activated fault. Two GMPEs, applicable for shallow Greek earthquakes, were employed, those of Bindi et al., (2007) and Akkar & Bommer (2010) in order to compare PGA values with the simulated ground motions obtained from EXSIM. In general, the simulated PGA values show good agreement with the values computed by the GMPEs (Figures 5.2 & 5.10) especially as the Joyner & Boore distance increases. After applying the merging technique, the broadband synthetic FAS and time series (Figures 5.5 - 5.8 & 5.13 - 5.15) were compared with the available recorded data (Tables 5.1 & 5.2). The comparison of the synthetic with the recorded FAS revealed a satisfactory fit both in amplitude and phases despite the fact that ground motions in some stations are slightly overestimated (VAS2 station) or underestimated (LXRB station). As far as the synthetic waveforms are concerned, the general shape and duration seems to be sufficiently represented by the hybrid simulations.

There are several useful applications concerning the results of the present study as well as plenty of possibilities for future research. First of all, the applied methodology of this study can be used in order to simulate past strong earthquakes for which there are not available recordings. In this manner, a potential strong ground motion database for a time period much longer than the recent instrumental period can be created and used in multiple applications such as the development of a region specific GMPE. The main challenge that modern GMPEs face is their inability to estimate strong ground motion in the near-field due to the lack of strong motion recordings and their inadequacy in replicating the directivity effects which are commonly observed in the near-field. The innovation introduced in the present and similar studies will lead to the development of reliable GMPEs that can reflect the near-source and directivity effects in contrary to the ones used in the past and nowadays.

Due to the increased level of complexity characterizing the scientific topics undertaken in this study, the research was based on several limitations and assumptions. The uniform type B soil condition taken into account for the calculations in the whole study area is a case in point. This particular assumption was required for two reasons. The first one was the inability of COMPSYN to adequately incorporate the local site effects and the second one was the lack of sufficient and/or reliable site characterization data for the study area. Consequently, the present study can be significantly improved in the future by taking into consideration the local site condition variability, for example by using Vs30 profiles covering the whole study area or by using ambient noise (HVSR), a technique widely used in Greece for site effects characterization (e.g. Apostolidis, 2002; Leventakis, 2003; Panou et al., 2005; Triantafyllidis et al., 2006; Kassaras et al., 2015)

Moreover, the present study could be extended to generate synthetic ground motions for future large earthquakes via a "most-probable" or a "worst-case" scenario. This complex procedure demands the specification of magnitude and rupture area, the examination of multiple hypothetical hypocenter locations and the resulting slip distribution over the fault, which can be represented by either kinematic or more complex dynamic rupture models. The results of this analysis could ultimately be compared to the PSHA maps created in the first part of this study as far as the level of expected PGA is concerned. This methodology has been widely used globally (e.g. Graves & Pitarka, 2010; Mena et al., 2010; Akinci et al., 2017) but little work has been done in Greece (e.g. Roumelioti et al., 2016; Ding et al., 2019; Kiratzi et al., 2019).

During the course of this study, the role of various fundamental seismological source and path parameters was investigated leading to a series of remarks. First of all, PGA variations were observed to be strongly influenced by slip heterogeneities and changes in the rupture propagation, such as the fault boundaries. PGA levels are primarily controlled by the hypocenter location, the assumed rupture velocity and the average stress drop. However, the average stress drop effect seems to gradually decrease in the far-field making room for other path and site related parameters. It should also be noted that the slip distribution on the fault surface does not considerably control the average simulated PGA values, yet it contributes significantly to the strong ground motion variability in the near-field.

# Data and Resources

The seismicity data were provided by the bulletins of the Seismological Station of Aristotle University of Thessaloniki (http://seismology.geo.auth.gr/ss/). Acceleration time histories from the seismological stations were provided by ITSAK (Institute of Earthquake Engineering and Engineering Seismology; http://www.itsak.gr) and the NOA-IG (National Observatory of Athens - Institute of Geodynamics; http:/bbnet.gein.noa.gr/HL).

A number of figures were created using the Generic Mapping Tools version 4.5.3 (Wessel et al., 2013). Plots and some figures were created with Grapher version 10 (http:// www.GoldenSoftware.com)

The HF ground motion simulations were performed using COMPSYN sxv3.11 (Spudich and Xu, 2002). The LF ground motion simulations were carried out using the EXSIM_DMB code (http://www.daveboore.com/software_online.html).

Seismic signal analysis was performed using SAC (Seismic Analysis Code) version 101.6 (Goldstein et al., 2003; Goldstein and Snoke, 2005).

# References

Aki, K., 1965. Maximum likelihood estimation of b in the formula logN a–bM and its confidence limits, Bull. Earthq. Res. Inst. Tokyo Univ. 43, no. 1965, 237–239.

Aki, K., 1967. Scaling law of seismic spectrum, J. Geophys. Res. 72, 1217–1231.

Aki, K., 1980. Scattering and attenuation of shear waves in the lithosphere, J. Geophys. Res., 85(B11), 6496– 6504, doi:10.1029/JB085iB11p06496.

Akinci, A., Aochi, H., Herrero, A., Pischiutta, M., Karanikas, D., 2017. Physics-Based Broadband Ground-Motion Simulations for Probable Mw ≥7:0 Earthquakes in the Marmara Sea Region (Turkey). Bulletin of the Seismological Society of America. 107. 10.1785/0120160096.

Akkar, S., Bommer, J., 2010. Empirical Equations for the Prediction of PGA, PGV, and Spectral Accelerations in Europe, the Mediterranean Region, and the Middle East. Seismological Research Letters - SEISMOL RES LETT. 81. 195-206. 10.1785/gssrl.81.2.195.

Ambraseys, N.N., Bommer, J.J., 1991. The attenuation of ground accelerations in Europe. Earthq. Eng. Struct. Dyn., 20, 1179-1202.

Anderson, H., Jackson, J., 1987. Active tectonics of the Adriatic region. Geophys. J.R. Astr. Soc., 91, 937-983.

Anderson, J.G., Hough, S.E., 1984. A Model for the Shape of the Fourier Amplitude Spectrum of Acceleration at High Frequencies. Bulletin of the Seismological Society of America, 74, 1969-1993.

Apostolidis, P., 2002. Determination of the soil structure using microtremors. Application to the estimation of the dynamic properties and the geometry of the soil formations at Thessaloniki city, PhD Thesis (in Greek), Aristotle University of Thessaloniki, Greece.

Assatourians, K., Atkinson, G., 2012. EXSIM12: A Stochastic Finite- Fault Computer Program in FORTRAN, http://www.seismotoolbox.ca (last accessed November 2014).

Atkinson, G., Boore, D., 1995. New ground motion relations for eastern North America, Bull. Seism. Soc. Am. 85, 17–30.

Atkinson, G., 1996. The High-Frequency Shape of the Source Spectrum for Earthquakes in Eastern and Western Canada. Bulletin of the Seismological Society of America. 86.

Atkinson, M., "An overview of developments in seismic hazard analysis" presented at the 13th World Conference on Earthquake Engineering, Vancouver, B.C., Canada, 2004.

Atkinson, G., Assatourians, K., 2014. Implementation and Validation of EXSIM (A Stochastic Finite-Fault Ground-Motion Simulation Algorithm) on the SCEC Broadband Platform. Seismological Research Letters. 86. 48-60. 10.1785/0220140097.

Avallone, A., Cirella, A., Cheloni, D., Tolomei, C., Theodoulidis, N., Piatanesi, A. , Briole, P., Ganas, A., 2017. Near-source high-rate GPS, strong motion and InSAR observations to image the 2015 Lefkada (Greece) Earthquake rupture history. Scientific Reports.

Bajaj, K., Panjamani, A., 2017. Determination of GMPE functional form for an active region with limited strong motion data: application to the Himalayan region. Journal of Seismology.

Banitsiotou, I. D., Tsapanos, T. M., Margaris, V. N., Hatzidimitriou, P. M., 2004. Estimation of the seismic hazard parameters for various sites in Greece using a probabilistic approach, Nat. Hazards Earth Syst. Sci., 4, 399–405, https://doi.org/10.5194/nhess-4-399-2004.

Beresnev, I., Atkinson, G., 1997. Modelling Finite-Fault Radiation from the n w Spectrum. Bulletin of the Seismological Society of America. 87.

Berge, C., Gariel, J.-C., Bernard, P., 1998. A very broad-band stochastic source model used for near source strong motion prediction. Geophys. Res. Lett. 25 (7), 1063–1066.

Bindi, D., Pacor, F., Sabetta, F., Massa, M., 2009. Towards a new reference ground motion prediction equation for Italy: Update of the Sabetta-Pugliese (1996). Bulletin of Earthquake Engineering. 7. 591-608. 10.1007/s10518-009-9107-8.

Boncori, M.J.P., Papoutsis, I., Pezzo, G., Tolomei, C., Atzori, S., Ganas, A., Karastathis, V., Salvi, S., Kontoes, C. and Antonioli, A., 2015. The February 2014 Cephalonia Earthquake (Greece): 3D Deformation Field and Source Modeling from Multiple SAR Techniques, Seismological Research Letters, January/February 2015, 86(1), 124-137.

Boore, D. M., 1983. Stochastic Simulation of High-frequency Ground Motions Based on Seismological Models of the Radiated Spectra, Bull. Seismol. Soc. Am. 73, 1865–1894.

Boore, D., 2003. Prediction of ground motion using the stochastic method, Pure Appl. Geophys. 160, 635–676.

Boore, D. M., 2009. Comparing stochastic point-source and finite-source ground-motion simulations: SMSIM and EXSIM, Bull. Seismol. Soc. Am. 99, no. 6, 3202–3216.

Boore, D., Joyner, W., 1997. Site amplifications for generic rock sites, Bull. Seism. Soc. Am. 87, 327–341.

Boore, D., Atkinson, G., 1987. Stochastic prediction of ground motion and spectral response parameters at hard-rock site in eastern North America. Bulletin of the Seismological Society of America, 77, 440-467.

Borcherdt, R. D., 1970. Effects of local geology on ground motion near San Francisco Bay, Bull. Seismol. Soc. Am. 60, 29–61.

Boyd, O. S., 2012. Including foreshock and aftershocks in time-independent probabilistic seismic-hazard analyses, Bull. Seismol. Soc. Am. 102, 909–917.

BP Co, 1971. The geological results of petroleum exploration in western Greece, Institute of Geology Subsurface Research, Athens, 10, 73 pp.

Brune, J., 1970. Tectonic stress and the spectra of seismic shear waves from earthquakes, J. Geophys. Res. 75, 4997–5009.

Brune, J. N., 1971. Correction, J. geophys. Res. 76, 5002.

Chousianitis, K., Konca, A. O., Tselentis, G.-A., Papadopoulos, G. A., Gianniou, M., 2016. Slip model of the 17 November 2015 Mw = 6.5 Lefkada earthquake from the joint inversion of geodetic and seismic data. Geophysical Research Letters, 43, 7973-7981.

Chousianitis, K., Del Gaudio, V., Pierri, P., Tselentis, G-A., 2018. Regional ground-motion prediction equations for amplitude-, frequency response-, and duration-based parameters for Greece. Earthquake Engng Struct Dyn., 47: 2252–2274.

Clément, C., Hirn, A., Charvis, P., Sachpazi, M., Marnelis, F., 2000. Seismic structure and the active Hellenic subduction in the Ionian Islands. Tectonophysics. 329. 141-156. 10.1016/S0040-1951(00)00193-1.

Cocard, M., Kahle, H-G, Peter, Y., Geiger, A., Veis, G., Felekis, S., Paradissis, D., Billiris, H., 1999. New constraints on the rapid crustal motion of the Aegean region: Recent results inferred from GPS measurements (1993-1998) across the West Hellenic Arc, Greece. Earth and Planetary Science Letters. 172. 39-47. 10.1016/S0012-821X(99)00185-5.

Cornell, C.A., 1968. Engineering seismic risk analysis, Bull. Seismo. Soc. Am., 58, 1,583–1,606.

Cornell, C.A., 1971. Probabilistic analysis of damage to structures under seismic loads, in Howells, D.A, Haigh, I.P., and Taylor, C., eds., Dynamic waves in civil engineering: Proceedings of a conference organized by the Society for Earthquake and Civil Engineering Dynamics, New York, John Wiley, 473–493

Cooke, P., 1979. Statistical inference for bounds of random variables, Biometrika 66, 367-374.

Cushing, M., 1985. Evoluation structurale de la marge nord-ouest hellenique dans l'ile de Lefkada et ses environs (Greece nord-occidentale), These du 3em cycle, Univ. de Paris-Sud (XI), Centre d'Orsay.

Danciu, L., Tselentis, A., 2007. Engineering Ground-Motion Parameters Attenuation Relationships for Greece. Bulletin of The Seismological Society of America - Bull. Seismol. Soc. Amer. 97. 162-183. 10.1785/0120050087.

Davis, S.D., Frolich, C., 1991. Single-link cluster analysis, synthetic earthquake catalogs, and aftershock identification, Geophys. J. Int. 104: 289-306.

Ding, Y., Mavroeidis, G., Theodoulidis, N., 2019. Simulation of strong ground motion from the 1995 Mw 6.5 Kozani-Grevena, Greece, earthquake using a hybrid deterministic-stochastic approach, Soil. Dyn. Earthq. Eng.: 117:357-73.

Doutsos, T., Kontopoulos, N., Fridas, D., 1987. Neotectonic evolution of northwestern continental Greece, Basin Res. 1, 177-190.

Esteva, L., 1970. Regionalización sísmica de México para fines de ingeniería. Instituto de Ingeniería. Universidad Nacional Autónoma de México.

Ferentinos, G., Brooks, M., Doutsos, T., 1985. Quaternary tectonics in the Gulf of Patras, western Greece, Journal of Structural Geology, Vol. 7, No. 6, pp. 713- 717.

Finetti, I., Morreli, C., 1973. Geophysical exprolation of the Mediterranean sea. Boll. Geofis. Teor. Appl., 15, 263-341.

Finetti, I., 1982. Structure, stratigraphy and evolution of central Mediterranean. Boll. Geofis. Teor. Appl., 24, 247-426.

Flinn, E.A., Engdahl, E.R., 1965. A proposed basis for geographical and seismic regionalization, Rev. Geophys., 3, 123–149, 1965.

Flinn, E.A., Engdahl, E.R., and Hill, A.R., 1974. Seismic and geographical regionalization, B. Seismol. Soc. Am., 64, 771–993, 1974.

Galanopoulos, A.G., 1950. Die Seismizitatder Insel Leukas, Geri. Beitr. Geophys., 63, 1-15.

Galanopoulos, A.G., 1953. Katalog der Erbeben in Griecheland fur die Zeit von 1879 bis 1892, Ann. Geol. Pays Hellen., 5, 144-229.

Galanopoulos, AG., 1960. A catalogue of shocks with Io ≥ VI or M ≥ 5 for the years 1801 - 1958, Athens, pp. 119.

Galanopoulos, AG., 1961. A catalogue of shocks with Io ≥ VII for the years prior to 1800, Athens, pp.19.

Ganas, A., Marinou, A, Anastasiou, D., Paradissis, D., Papazissi, K., Tzavaras, P., Drakatos, G., 2013. GPS-derived estimates of crustal deformation in the central and north Ionian Sea, Greece: 3-yr results from NOANET continuous network data, Journal of Geodynamics, 67, 62-71.

Ganas, A., Elias, P., Bozionelos, G., Papathanassiou, G., Avallone, A., Papastergios, A., Valkaniotis, S., Parcharidis, I., Briole, P., 2016. Coseismic deformation, field observations and seismic fault of the 17 November 2015 M = 6.5, Lefkada Island, Greece earthquake. Tectonics 687:210–222 (ISSN 0040–1951). http://dx.doi.org/10.1016/j. tecto.2016.08.012.

Gardner, G.H.F., Gardner, L.W., Gregory, A.R., 1974. Formation velocity and density – the diagnostic basics for stratigraphic traps: Geophysics, 39, 770-780.

Gardner, J. K., Knopoff, L., 1974. Is the sequence of earthquakes in southern California, with aftershocks removed, Poissonian? Bull. Seismol. Soc. Am. 64, 1363–1367.

Garini, E., Gazetas, G., Anastasopoulos, I., 2017. Evidence of significant forward rupture directivity aggravated by soil response in an Mw6 earthquake and the effects on monuments. Earthquake Engineering & Structural Dynamics, 46(13), 2103-2120.

GEER/EERI/ATC Earthquake Reconnaissance. January 26th /F ebruary 2nd 2014 Cephalonia, Greece events. Version 1: June 2014.

Geophysical Laboratory, Geology Department, Aristotle University of Thessaloniki (AUTH), available at: http://seismology.geo.auth.gr/ss/.

Giardini, D., Woessner, J., Danciu, L., 2013. Seismic Hazard Harmonization in Europe (SHARE): online data resource. doi:10.12686/SED-00000001-SHARE

Giardini, D., Woessner, J., Danciu, L., 2014. Mapping Europe's Seismic Hazard. EOS, 95(29): 261-262.

Goldstein, P., Dodge, D., Firpo, M., Minner, L., 2003. "SAC2000: Signal processing and analysis tools for seismologists and engineers, Invited contribution to "The IASPEI International Handbook of Earthquake and Engineering Seismology", Edited by WHK Lee, H. Kanamori, P.C. Jennings, and C. Kisslinger, Academic Press, London.

Goldstein, P., Snoke, A., 2005. "SAC Availability for the IRIS Community", Incorporated Institutions for Seismology Data Management Center Electronic Newsletter.

Graves, R., Pitarka, A., 2004. Broadband time history simulation using a hybrid approach.

Guatteri, M., Mai, P.M., Beroza, G.C., 2004. A PD approximation to dynamic rupture models for strong ground motion prediction, Bull. Seismol. Soc. Am. 94, 2051–2063.

Gutenberg, B., Richter, C. F., 1944. Frequency of earthquakes in California, B. Seismol. Soc. Am., 34, 185–188.

Gupta, H.K., Singh, H.N., 1989. Earthquake swarms precursory to moderate to great earthquakes in the northeast Indi region. Tectonophysics 167, 285-298.

Gupta, S.C., Singh, V.N., Kumar, A., 1995. Attenuation of coda waves in the Garhwal Himalaya, India. Phys. Earth Planet. Inter. 87, 247-253.

Habermann, R.E., 1987. Man-made changes of seismicity rates, Bull. Seismol. Soc. Am. 77, 141–159.

Hanks, T., 1982. fm~x, Bull. Seism. Soc. Am. 72, 1867-1879.

Hartzell, S.H., 1978. Earthquake aftershocks as Green's functions. Geophys. Res. Lett., 5: 1-4. doi:10.1029/GL005i001p00001

Hatzfeld, D., Kassaras, I., Panagiotopoulos, D., Amorese, D., Makropoulos, K., Karakaisis, D., Coutant, O., 1995. Microseismicity and strain pattern in northwestern Greece. Tectonics, Vol.14, No 4, 773-785.

Hatzfeld, D., Karagianni, E., Kassaras, I., Kiratzi, A., Louvari, E., Lyon-Caen, H., Makropoulos, K., Papadimitriou, P., Bock, G., Priestley, K., 2001. Shear wave anisotropy in the upper mantle beneath the Aegean related to internal deformation. Journal of Geophysical Research B: Solid Earth. 106. 30737-30753. 10.1029/2001JB000387.

Hatzidimitriou, P. M., Papadimitriou, E. E., Mountrakis, D. M., and Papazachos, B. C., 1985. The seismic parameter b of the frequency - magnitude relation and its association with the geological zones in the area of Greece, Tectonophysics, 120, 141–151.

Hatzidimitriou, P., Papazachos, C., Kiratzi, A., Theodulidis, N., 1993. Estimation of attenuation structure and local earthquake magnitude based on accleration records in Greece, Tectonophysics 217, 243–253.

Hatzidimitriou, P., 1995. S-wave attenuation in the crust in Northern Greece, Bull. Seism. Soc. Am. 85, 1381- 1387.

Hollenstein, Ch., Müller, M.D., Geiger, A., Kahle, H.G., 2008. Crustal motion and deformation in Greece from a decade of GPS measurements, 1993–2003. Tectonophysics. 449. 17-40. 10.1016/j.tecto.2007.12.006.

Husen, S., Hardebeck, J.L., 2011. Understanding seismicity catalogs and their problems, Community Online Resource for Statistical Seismicity Analysis doi: 10.5078/corssa-55815573.

Iervolino, I., Giorgio, M., Polidoro, B., 2012. Probabilistic seismic hazard analysis for seismic sequences, in Vienna Congress on Recent Advances in Earthquake Engineering and Structural Dynamics 2013, C. Adam, R. Heuer, W. Lenhardt, and C. Schranz (Editors), 28–30 August 2013, Vienna, Austria, Paper No. 66

Irikura, K., 1986. Prediction of strong acceleration motion using empirical Green's function,Proc. 7th Japan Earthq. Eng. Symp., Tokyo, 151-156.

Irikura, K., Miyake, H., 2011. Recipe for predicting strong ground motion from crustal earthquake scenarios. Pure Appl. Geophys., 168, 85-104, doi: 10.1007/s00024-010-0150-9.

Jackson, J., 1994. Active tectonics of the Aegean region. Annual Review of Earth and Planetary Sciences, 22: 239-271.

Jenny, S., Goes, S., Giardini, D., Kahle, H.-G., 2004. Earthquake recurrence parameters from seismic and geodetic strain rates in the eastern Mediterranean. Geophys. J. Int. 157, 1331–1347.

Jin, A., Aki, K., 1988. Spatial and Temporal Correlation between Coda Q and Seismicity in China. Bulletin of the Seismological Society of America, 78, 741-769.

Kahle, H.-G., Muller, M.V., Mueller, St., Veis, G., 1993b. The Kephalonia transform fault and the rotation of the Apulian platform: Evidence from satellite geodesy. Geophys. Res. Lett., 20(8): 651-654.

Kahle, H., Muller, M., Geiger, A., Danuser, G., Mueller, S., Veis, G., Billiris, H., Paradissis, D., 1995. The strain field in northwestern Greece and the Ionian islands: results inferres from GPS measurements. Tectonophysics, 249, 41-52.

Kahle, H., Muller, M., Veis, G., 1996. Trajectories of crustal deformation of Western Greece from GPS observations 1989 - 1994. J. Geophys. Lett., 23, 677-680.

Kahle, H-G, Cocard, M., Peter, Y., Geiger, A., Reilinger, R., Barka, A., Veis, G., 2000. GPS-derived strain rate field within the boundary zones of the Eurasian, African, and Arabian Plates. Journal of Geophysical Research. 105.

Kanamori, H., Anderson, D., 1975. Theoretical Basis of Some Empirical Relations in Seismology. Bulletin of the Seismological Society of America. 65. 1073-1095.

Kapetanidis, V., Agalos, A., Moshou, A., Kaviris, G., Karakonstantis, A., Papadimitriou, P., Makropoulos, K., 2008. Preliminary results from the study of a seismic swarm occurred in February 2008 in NW Peloponnesus.

Kapetanidis, V., Deschamps, A., Papadimitriou, P., Matrullo, E., Karakonstantis, A., Bozionelos, G., Kaviris, G., Serpetsidaki, A., Lyon-Caen, H., Voulgaris, N., Bernard, P., Sokos, E., Makropoulos, K., 2015. The 2013 earthquake swarm in Helike, Greece: seismic activity at the root of old normal faults. Geophys. J. Int. 202 (3), 2044–2073. https://doi.org/10.1093/gji/ ggv249.

Karakostas, V., Papadimitriou, E., Papazachos, C., 2004. Properties of the 2003 Lefkada, Ionian islands, Greece, Earthquake seismic sequence and seismicity triggering. BSSA 94 (5), 1976–1981.

Karakostas, V.G., Papadimitriou, E.E., 2010. Fault complexity associated with the 14 August 2003 Mw6.2 Lefkada, Greece, aftershock sequence. Acta Geophys. 58: 838. https://doi.org/10.2478/s11600-010-0009-6.

Karakostas, V., Papadimitriou, E., Mesimeri, M., Gkarlaouni, C., Paradisopoulou, P., 2015. The 2014 Kefalonia doublet (M w 6.1 and M w 6.0), central Ionian islands, Greece: seismotectonic implications along the Kefalonia transform fault zone. Acta Geotech. 1–16 http://dx.doi.org/10.2478/s11600-014-0227-4.

Karastathis, V., Mouzakiotis, A., Ganas, A., Papadopoulos, G., 2015. High-precision relocation of seismic sequences above a dipping Moho: The case of the January–February 2014 seismic sequence on Cephalonia Island (Greece). Solid Earth. 6. 10.5194/se-6-173-2015.

Kassaras, I., Papadimitriou, P., Hatzfeld, D., Makropoulos, K., Drakopoulos, J., 1994. Microearthquake seismicity and fault plane solutions in northwestern Greece.

Kassaras, I., Kalantoni, D., Benetatos, Ch., Kaviris, G., Michalaki, K., Sakellariou N., Makropoulos, K., 2015. Seismic damage scenarios in Lefkas old town (W. Greece). Bull. Earth. Engin., Vol. 13, Iss. 12, 3669-3711.

Κασσάρας, Ι., & Καβύρης, Γ., 2016. Εργαστηριακά Κεφάλαια Σεισμολογίας. Ανάκτηση από http://eclass.uoa.gr/courses/GEOL233/.

Kassaras, I., Kazantzidou-Firtinidou, D., Ganas, A., Tonna, S., Pomonis, A., Karakostas, Ch., Papadatou-Giannopoulou, Ch., Psarris, D., Lekkas, E., Makropoulos, K., 2018. On the Lefkas (Ionian Sea) November 17, 2015 Mw=6.5 Earthquake Macroseismic Effects. Journal of Earthquake Engineering. 1-31. 10.1080/13632469.2018.1488776.

Kastens, K. A., Gilbert, L. E., Hurst, K. J.A, Veis, G., Paradissis, D., Billiris, H., Schluter, W. and Seeger, H., 1996. GPS evidence for arc-parallel extension along the Hellenic arc, Greece. Tectonophysics.

Kazantzidou-Firtinidou, D., Kassaras, I., Tonna, S., Ganas, A., Vintzileou, E. and Chesi, C. [2016] "The November 2015 Mw6.4 earthquake effects in Lefkas Island", Proc. of 1st ICONHIC, Crete, Paper No 119

Kaviris, G., Papadimitriou, P., Makropoulos, K., 2010. Anisotropy study of the February 4th 2008 swarm in NW Peloponnesus (Greece). Bull. Geol. Soc. Greece, vol. XLIII, No 4, p. 2084-2092. doi: 10.12681/bgsg.11398.

Kaviris, G., Millas, C., Spingos, I., Kapetanidis, V., Fountoulakis, I., Papadimitriou, P., Voulgaris, N., Makropoulos, K., 2018. Observations of shear-wave splitting parameters in the Western Gulf of Corinth focusing on the 2014 Mw ¼ 5.0 earthquake. Phys. Earth Planet. Inter. 282, 60–76. https://doi.org/10.1016/j. pepi.2018.07.005.

Kaviris, G., Spingos, I., Kapetanidis, V., Papadimitriou, P., Voulgaris, N., Makropoulos, K., 2017. Upper crust seismic anisotropy study and temporal variations of shear-wave splitting parameters in the western Gulf of Corinth (Greece) during 2013. Phys. Earth Planet. Inter. 269 https://doi.org/10.1016/j. pepi.2017.06.006.

Kazantzidou-Firtinidou, D., Kassaras, I., Tonna, S., Ganas, A., Vintzileou, E., Chesi, C., 2016. "The November 2015 Mw6.4 earthquake effects in Lefkas Island", Proc. of 1st ICONHIC, Crete,Paper No 119.

Kijko, A., Singh M., 2011. Statistical tools for maximum possible earthquake magnitude estimation, Acta Geophys. 59, 674-700.

King G., Sturdy D., Whitney, J., 1993. The landscape geometry and active tectonics of the northwest Greece, Geol. Soc. Am. Bull. 105, 137-161.

Kiratzi A., Papadimitriou E., Papazachos, B.C., 1987. A microearthquake survey in the Steno dam site in northwestern Greece, Ann. Geophys. 592, 161-166.

Kiratzi, A., Langston, C., 1991. Moment tensor inversion of the 1983 January 17 Kefallinia event of Ionian islands (Greece). Geophys. J. Int., 105, 529-538.

Kiratzi, A., Louvari, E., 2003. Focal mechanisms of shallow earthquakes in the Aegean Sea and the surrounding lands determined by waveform modeling: a new database. J. Geodyn. 36, 251–274.

Kiratzi, A., Roumelioti, Z., Makra, K., Klimis, N., Koskosidi, A., 2019. Hybrid broadband seismic ground motions: application to the city of Edessa in northern Greece.

Klimis, N., Margaris, B., Koliopoulos, P., 1999. Site dependent amplification functions and response spectra in Greece, J. Earthquake Eng. 3, no. 2, 237–247.

Kokinou, E., Papadimitriou, E., Karakostas, V., Kamperis, E., Vallianatos, F., 2006. The Kefalonia Transform Zone (offshore Western Greece) with special emphasis to its prolongation towards the Ionian Abyssal Plain. Marine Geophysical Researches. 27. 241-252. 10.1007/s11001-006-9005-2.

Kostrov, B., Das, S., 1988. Principles of Earthquake Source Mechanics.Cambridge University Press, London.

Lay, T., Wallace, T.C., 1995. Modern global seismology, Volume 58 of International geophysics series. San Diego: Academic Press.

Lekkas E, Mavroulis, S., 2015. Earthquake environmental effects and ESI 2007 seismic intensities of the early 2014 Cephalonia (Ionian Sea, western Greece) earthquakes (January 26 and February 3, Mw 6.0). Nat Hazards. doi: 10.1007/s11069-015-1791.

Lekkas, E., Mavroulis, S., Carydis, P., Alexoudi, V., 2018. The 17 November 2015 Mw 6.4 Lefkas (Ionian Sea, Western Greece) Earthquake: Impact on Environment and Buildings. Geotechnical and Geological Engineering. 36. 10.1007/s10706-018-0452-8.

Le Pichon, X., Chamot-Rooke, N., Lallemant, S., Noomen, R., Veis, G., 1995. Geodetic determination of the kinematics of Central Greece with respect to Europe. Journal of Geophysical Research. 100. 12675-12690. 10.1029/95JB00317.

Leptokaropoulos, K. M., Karakostas, V.G., Papadimitriou, E.E., Adamaki, A.K., Tan, O., İnan, S., 2013. A homogeneous earthquake catalogue compilation for western turkey and magnitude of completeness determination, Bull. Seismol. Soc. Am. 103, 2739–2751.

Leventakis, G.A., 2003. Microzonation study of the city of Thessaloniki, PhD, Aristotle University of Thessaloniki, 84 p.

Louvari, E., Kiratzi, A.A., Papazachos, B.C., 1999. The Cephalonia transform fault and its extension to western Lefkada island (Greece). Tectonophysics 308 (1999) 223-236.

Mai, P. M., 2009. Ground motion: Complexity and scaling in the near field of earthquake ruptures, in Encyclopedia of Complexity and Systems Science, W. H. K. Lee and R. Meyers (Editors), Springer, New York, 4435–4474.

Mai, P.M., Beroza, G.C., 2003. A hybrid method for calculating nearsource, broadband seismograms: Application to strong motion prediction, Phys. Earth Planet. In. 137, nos. 1/4, 183–199, doi: 10.1016/ S0031-9201(03)00014-1.

Makropoulos, K.C., 1978. The statistics of large earthquake magnitude and an evaluation of Greek seismicity. Phd Thesis, Univ. of Edinburgh.

Makropoulos, K.C., Burton, P.W., 1985. HAZAN: A Fortran program to evaluate seismic - hazard parameters using Gumbel's theory of extreme value statistics. Computers & Geosciences Vol . 12, 29-46.

Makropoulos, K., Diagourtas, D., Kassaras, J., Kouskouna, V., Papadimitriou, P., Ziazia, M., 1996. The November - December 1994 Lefkas (W. Greece) earthquake sequence: results from in situ seismological survey (abstract). 1st Congress of the Balkan Geophysical Society, Sept. 23-27, Athens.

Makropoulos, K., Kaviris, G., Kouskouna, V., 2012. An updated and extended earthquake catalogue for Greece and adjacent areas since 1900, Nat. Hazards Earth Syst. Sci., 12, 1425-1430.

Margaris, B.N., Boore, D.M., 1998. Determination of Δσ and κο from response spectra of large earthquakes in Greece, Bull. Seism. Soc. Am. 88.

Margaris, B., Hatzidimitriou, P., 2002. Source Spectral Scaling and Stress Release Estimates Using Strong-Motion Records in Greece. Bulletin of the Seismological Society of America. 92. 1040-1059. 10.1785/0120010126.

Margaris, B.N., Papazachos, C.B., Papaioanou, Ch., Theodoulidis, N., Kalogeras, I., Skarlatoudis, A.A., 2002. Empirical attenuation relations for the horizontal strong ground motion parameters of shallow earthquakes in Greece. 12th European Conf. on Earthquake Engineering, London.

Marzocchi, W., Sandri, L., 2003. A review and new insights on the estimation of the b-value and its uncertainty. Annals of Geophysics. 46. 1271-1282.

Marzocchi, W., Taroni, M., 2014. Some thoughts on declustering in probabilistic seismic-hazard analysis, Bull. Seismol. Soc. Am. 104, 1838–1845.

McGuire, R.K., 1976. FORTRAN computer program for seismic risk analysis, U.S. Geological Survey Open-File Report 76-67.

McKenzie, D.P., 1978. Some remarks on the development of sedimentary basins, «Earth and Planetary Science Letters», 40, 25-32.

Mena, B., Mai, P., Olsen, K., Purvance, M., Brune, J., 2010. Hybrid Broadband Ground-Motion Simulation Using Scattering Green's Functions: Application to Large-Magnitude Events. Bulletin of The Seismological Society of America - BULLSEISMOL SOC AMER. 100. 2143-2162. 10.1785/0120080318.

Mercier, J., Carey, E., Philip, H., Sorel, D., 1976. La neotectonique plio-quaternaire de l' arc egeen externe et de la mer Egee et ses relations avec la seismicite. Bull. Soc. Geol. Fr.2.

Mesimeri, M., Karakostas, V., Papadimitriou, E., Schaff, D., Tsaklidis, G., 2016. Spatiotemporal properties and evolution of the 2013 Aigion earthquake swarm (Corinth Gulf, Greece). J. Seismol. 20 (2), 595–614. https://doi.org/10.1007/s10950-015-9546-4.

Mesimeri, M., Karakostas, V., Papadimitriou, E., Tsaklidis, G., Jacobs, K., 2018. Relocation of recent seismicity and seismotectonic properties in the Gulf of Corinth (Greece). Geophys. J. Int. 212(2, 1123–1142. ttps://doi.org/10.1093/gji/ggx450.

Mignan, A., Woessner, J., 2012. Estimating the magnitude of completeness for earthquake catalogs. Community Online Resource for Statistical Seismicity Analysis. 10.5078/corssa-00180805.

Millas, Ch., 2018. Slip Distribution Of Large Earthquakes In Greece, MSc Thesis. National and Kapodistrian University of Athens, Greece.

Millas, Ch., Kaviris, G., Karakostas, V., Papadimitriou, P., 2018. Slip distribution and resulting surface deformation assessment of strong earthquakes in Greece. Abstract, 36th ESC General Assembly, Valetta, Malta, ESC2018-S19-573.

Motazedian, D., Atkinson, G.M., 2005. Stochastic finite-fault mod-eling based on a dynamic corner frequency, Bull. Seismol. Soc. Am.95, 995–1010.

Nakamura, Y., 1989. A method for dynamic characteristics estimation of subsurface using microtremor on the ground surface, QR RTRI 30, 25–33.

Nyst, M., Thatcher, W., 2004. New constraints on the active tectonic deformation of the Aegean. JGR, Vol 109, No B11, 406.

Olson, A.H., Orcutt, J.A., Frazier, G.A., 1984, The discrete wavenumber / finite element method for synthetic seismograms, Geophys. J. R. Astr. Soc., v. 77, 421- 460.

Oral, M.B., Reilinger, R.E., Toksöz, M.N., King, R.W., Barka, A.A., Kinik, I., Lenk, O., 1995. Global positioning system offers evidence of plate motions in eastern Mediterranean, EOS Trans. AGU 76, 2, 9-11.

Ordaz, M., 1991. CRISIS. Brief description of program CRISIS, Internal report. Institute of Solid Earth Physics. University of Bergen, Norway, 16pp.

Ordaz, M., 1999. User's manual for program CRISIS1999. Technical report. Universidad Nacional Autónoma de México. Mexico City, Mexico.

Ordaz, M., Salgado-Gálvez, M.A., 2018. R-CRISIS Validation and Verification Document. ERN Technical Report. Mexico City, Mexico.

Panou, A., Theodoulidis, N., Hatzidimitriou, P., Stylianidis, K., Papazachos, C., 2005. Ambient noise horizontal-to-vertical spectral ratio in site effects estimation and

correlation with seismic damage distribution in urban environment: the case of the city of Thessaloniki (Northern Greece). Soil Dyn Earthq Eng 25:261–274

Papadimitriou, P., 1988. Etude de la structure du manteau superieur de l' Europe et modelisation des ondes de volume engendrees par des seismes Egeens. Phd Thesis, University Paris.

Papadimitriou, P., Kaviris, G., Makropoulos, K., 2006. The Mw= 6.3 2003 Lefkada earthquake (Greece) and induced stress transfer changes. Tectonophysics 423, 73–82. https://doi.org/10.1016/j.tecto.2006.03.003

Papadimitriou, P., Karakonstantis, A., Bozionelos, G., Kapetanidis, V., Kaviris, G., Spingos, I., Millas, Ch., Kassaras, I., Voulgaris, N., 2015. Preliminary report on the Lefkada 17 November 2015 Mw=6.4 earthquake.

Papadimitriou, E., 1993. Focal mechanism along the convex side of the Hellenic Arc. Bollettino di Geofisica Teorica ed Applicata. 35. 401-426.

Papadimitriou, E.E., 2002. Mode of strong earthquake recurrence in the central Ionian Islands (Greece): Possible triggering due to Coulomb stress changes generated by the occurrence of previous strong shocks, Bull. Seismol. Soc. Am. 92, 8, 3293-3308, DOI: 10.1785/0120000290.

Papadimitriou, E., Karakostas, V., Mesimeri, M., Chouliaras, G., Kourouklas, Ch., 2017. The Mw6.5 17 November 2015 Lefkada (Greece) Earthquake: Structural Interpretation by Means of the Aftershock Analysis. Pure and Applied Geophysics. 174. 10.1007/s00024-017-1601-3.

Papadopoulos, G., Karastathis, V., Koukouvelas, I., Sachpazi, M., Baskoutas, I., Chouliaras, G., Agalos, A., Daskalaki, E., Minadakis, G., Moshou, A., Mouzakiotis, A., Orfanogiannaki, K., Papageorgiou, A., Spanos, D., Triantafyllou, I., 2014. The Cephalonia, Ionian Sea (Greece), sequence of strong earthquakes of January-February 2014: A first report. 4. 5441-19. 10.4081/rg.2014.5441.

Papageorgiou, A., Aki, K., 1983. A specific barrier model for the quantitative description of inhomogeneous faulting and the prediction of strong ground motion. Part I: description of the model, Bull. Seism. Soc. Am. 73, 693-722.

Papaioannou, Ch.A., Papazachos, B.C., 2000. Time-independent and time-dependent seismic hazard in Greece based on seismogenic sources, B. Seismol. Soc. Am., 90, 22–33.

Papaioannou, C.A., 2001. Final rpt. of the Project: "Selection and elaboration of seismological data&compilation of new seismic hazard map of Greece compatible with the current Greek Seismic Code and Eurocode 8", [Scient. Resp.], EPPO-ITSAK, Greece, 68 pp.

Παπανικολάου, Δ.Ι., Σίδερης, Χρ.Ι., 2005. Γεωλογία. Η επιστήμη της Γης. Εκδόσεις Πατάκη, 291 σελ.

Papanikolaou, D., Bargathi, H., Dabovski, C., Dimitriu, R., El-Hawat, A., Ioane, D., Kranis, H., Obeidi, A., Oaie, G., Seghedi, A., Zagorchev, I., 2004. Transect VII: East European Craton - Scythian Platform - Dobrogea - Balkanides - Rhodope Massif - Hellenides - East Mediterranean - Cyrenaica. In: The TRANSMED Atlas - The Mediterranean Region from Crust to Mantle - Geological and Geophysical Framework of the Mediterranean and the Surrounding Areas, Editors: Cavazza, W., Roure, F., Spakman, W., Stampfli, G.M., Ziegler, P.A.

Papathanassiou, G., Valkaniotis, S., Ganas, A., Pavlides, S., 2013. GIS-based statistical analysis of the spatial distribution of earthquake-induced landslides in the island of Lefkada, Ionian Islands, Greece. Landslides 10 (6):771–783. http://dx.doi.org/10.1007/s10346–012-0357S.

Papathanassiou G., Valkaniotis S., Ganas A., Grendas N., Kollia E., 2017. The November 17th, 2015 Lefkada (Greece) strike-slip earthquake: field mapping of generated failures and assessment of macroseismic intensity ESI-07, Eng. Geol. , 220, 13–30.

Papazachos, B.C., 1974. Dependence of the seismic parameter b on the Magnitude range. Pure Appl. Geophys., 112, 1059-1065.

Papazachos, B.C., 1980. Seismicity rates and long term earthquake prediction in the Aegean area, Quaterniones Geodaesiae, 3, 171– 190.

Papazachos, B.C., 1990. Seismicity of the Aegean and surrounding area, Tectonophysics, 178, 287–308.

Papazachos, B.C., Papaioannou, C.A., 1993. Long term earthquake prediction in the Aegean area based on a time and magnitude predictable model, Pure Appl. Geophys., 140, 595–612.

Papazachos, B., 1996. Large seismic faults in the Hellenic arc. Annals of Geophysics. 39. 10.4401/ag-4023.

Papazachos C., Kiratzi A., 1996. A detailed study of the active crustal deformation in the Aegean and and surrounding area, Tectonophysics 253, 129-153.

Papazachos, B.C., Papadimitriou, E.E., Kiratzi, A.A., Papazachou, C.B., Louvari, E.K., 1998. Fault plane solutions in the Aegean sea and the surrounding area and their tectonic implication, Boll. Geof. Teor. Appl. 39, 3, 199-218.

Papazachos, C.B., 1999. Seismological and GPS evidence for the Aegean-Anatolia interaction. Geophysical Research Letters, 26: 2653-2656.

Papazachos, B.C., Comninakis, P.E., Karakaisis, G.F., Karakostas, B.G., Papaioannou, Ch.A., Papazachos, C.B., Scordilis, E.M., 2000. A catalogue of earthquakes in Greece and surrounding area for the period 550BC-1999. Publ. Geoph. Lab., Univ. of Thessaloniki, 1, 333pp.

Papazachos, B.C., Papazachou, C.B., 2003. The earthquakes of Greece. Ziti publications, Thessaloniki, 273pp.

Papazachos, B.C., Scordilis, E., Panagiotopoulos, D., Papazachos, C., Karakaisis, G., 2004. Global relations between seismic fault parameters and moment magnitude of earthquakes. Bulletin of the Geological Society of Greece. 36. 1482-1489. 10.12681/bgsg.16538.

Papazachos, B.C., Comninakis, P.E., Scordilis, E.M., Karakaisis, G.F., Papazachos C.B., 2010. A catalogue of earthquakes in the Mediterranean and surrounding area for the period 1901-2010, Publ. Geophys. Laboratory, University of Thessaloniki.

Pérouse, E., Sébrier, M., Braucher, R., Chamot-Rooke, N., Bourlès, D., Briole, P., Sorel, D., Dimitrov, D., Arsenikos, S., 2016. Transition from collision to subduction in Western Greece: the Katouna–Stamna active fault system and regional kinematics. International Journal of Earth Sciences. 106. 10.1007/s00531-016-1345-9.

Peter, Y., Kahle, H-G, Cocard, M., Veis, G., Felekis, S., Paradissis, D., 1998. Establishment of a continuous GPS network across the Kephalonia Fault Zone, Ionian Islands, Greece. Tectonophysics. 294. 253-260. 10.1016/S0040-1951(98)00103-6.

Raghukanth, S.T.G., Somala, S.N., 2009. Modeling of Strong-Motion Data in Northeastern India: Q, Stress Drop, and Site Amplification Bull. Seism. Soc. Am. 99, 705-725.

Reasenberg, P., 1985. Second-order moment of central California seismicity, 1969–1982, J. Geophys. Res. 90, 5479–5495.

Reilinger, R., Mcclusky, S., Oral, B., King, R., Toksoz, M., Barka, A.A., Kinik, I., Lenk, O., Sanli, I., 1997. Global Positioning System measurements of present-day crustal movements in the Arabia-Africa-Eurasia plate collision zone. Journal of Geophysical Research. 102. 9983-10000. 10.1029/96JB03736.

Reilinger, R., Ergintav, S., Burgmann, R., Mcclusky, S., Lenk, O., Barka, A., Gurkan, O., Hearn, L., Feigl, K., Cakmak, R., Aktug, B., Ozener, H., Töksoz, M.N., 2000. Coseismic and Postseismic Fault Slip for the 17 August 1999, M = 7.5, Izmit, Turkey Earthquake. Science (New York, N.Y.). 289. 1519-1524.

Reiter, L., 1990. Earthquake Hazard Analysis: Issues and Insights. New York: Columbia University Press.

Robinson, R., 1979. Variation of energy release, rate of occurrence and b value of earthquakes in the main seismic region, New Zealand, Phys. Earth Planet. Interiors 18, 209-220.

Robson, D.S., Whitlock, J.H., 1964. Estimation of a truncation point, Biometrika 51, 33-39.

Roumelioti, Z., Kiratzi, A., Margaris, B., Chatzipetros, A., 2016. Simulation of strong ground motion on near-fault rock outcrop for engineering purposes: The case of the city of Xanthi (Northern Greece). Bull. Earthq. Eng. 15, 25–49.

Sachpazi, M., Hirn, A., Clément, C., Haslinger, F., Laigle, M., Kissling, E., Charvis, P., Hello, Y., Lépine, J-C, Sapin, M., Ansorge, J., 2000. Western Hellenic subduction and Cephalonia Transform: Local earthquakes and plate transport and strain. Tectonophysics. 319. 301-319. 10.1016/S0040-1951(99)00300-5.

Sahu, O.P., Saikia, M.M., 1994. The b value before the 6th August, 1988 India-Myanmar border region earthquake: a case study. Tectonophysics 234, 349-354.

Scherbaum F., Bommer J.J., Bungum H., Cotton F., Abrahamson N.A., 2005. Composite ground-motion models and logic trees: methodology, sensitivities and uncertainties. Bulletin of the Seismological Society of America. 95(5):1575-1593.

Scholz, C., 1968. Microfracturing and the inelastic deformation of rock in compression. J. Geophys. Res. 73(4), 1417-1432.

Scordilis, E.M., Karakaisis, G.F., Karakostas, B.G., Panagiotopoulos, D.G., Comninakis, P.E., Papazachos, B.C., 1985. Evidence for transform faulting in the Ionian sea: The Cephalonia island earthquake sequence of 1983. Pure Appl. Geophys, 123, 388-397.

Segou, M., 2010. Frequency dependent seismic hazard in Greece by probabilistic and deterministic analysis. PhD Thesis.

Segou, M., Voulgaris, N., 2013. The Use of Stochastic Optimization in Ground Motion Prediction. Earthquake Spectra: Vol. 29, No. 1, pp. 283-308.

Senior Seismic Hazard Analysis Committee (SSHAC) Budnitz, R. J., G. Apostolakis, D. M. Boore, L. S. Cluff, K. J. Coppersmith, C. A. Cornell, Morris, P.A, 1997. Recommendations for probabilistic seismic hazard analysis: Guidance on uncertainty and use of experts, Washington, D.C., U.S. Nuclear Regulatory Commission Report, NUREG/CR-6372.

SHARE, 2010. Compilation od existing regional and national seismic source zones. Seventh Freaework Programme.

Siddiqqi, J., Atkinson, G., 2002. Ground motion amplification at rocksites across Canada, as determined from the horizontal-to-verticalcomponent ratio, Bull. Seism. Soc. Am. 92, 877–884.

Singh, S.K., Garcia, D., Pacheco, J.F., Valenzuela, R., Bansal, B.K., Dattatrayam R.S., 2004. Q of the Indian shield; Bull. Seismol. Soc. Am. 94 1564–1570.

Skarlatoudis, A.A., Papazachos, C.B., Margaris, B.N., Theodoulidis, N., Papaioannou, C.H., Kalogeras, I., Scordilis, E.M., Karakostas, V.G., 2003. Empirical peak ground motion predictive relations for shallow earthquakes in Greece. Bull. Seismol. Soc. Am, 93, 2591-2603.

Slejko, D., Santulin, M., Garcia, J., Papoulia, J. Daskalaki, E., Fasulaka, Ch., Fokaefs, A., Ilinski, D., Mascle, J., Makris, J., Nicolich, R., Papadopoulos, G. A., Tsambas, A., Wardell, N., 2010. SEAHELLARC Working Group. Preliminary seismic hazard assessments for the area of Pylos and surrounding region (SW Peloponnese), Boll. Geof. Teor. Appl., 51, 163–186.

Smith, W., 1981. The b-value as an earthquake precursor, Nature 289, 136-139.

Smith, W., 1986. Evidence for precursory changes in the frequency-magnitude b-value. Geophys. J. R. Asron. Soc. 86 (3). 815-838.

Song, S.G. & Dalguer, L.A., 2013. Importance of 1-point statistics in earthquake source modelling for ground motion simulation, Geophys. J. Int.,192, 1255–1270.

Sokos, E., Kiratzi, A., Gallovič, F., Zahradnik, J., Serpetsidaki, A., Plicka, V., Janský, J., Kostelecký, J., Tselentis, A., 2015. Rupture process of the 2014 Cephalonia, Greece,

earthquake doublet (Mw6) as inferred from regional and local seismic data. Tectonophysics. 656. 10.1016/j.tecto.2015.06.013.

Sokos, E., Zahradník, J., Gallovič, F., Serpetsidaki, A., Plicka, V., Kiratzi, A., 2016. Asperity break after 12 years: the Mw6.4 2015 Lefkada (Greece) earthquake. Geophys. Res. Lett. 43:6137–6145. http://dx.doi.org/10.1002/2016GL069427.

Song S., Dalguer, L.A., 2013. Importance of 1-point statistics in earthquake source modeling for ground motion simulation, Geophys. J. D210 Int., 192, 1,255-1,270.

Spudich, P., 1980. The Dehoop-Knopoff representation theorem as a linear inversion problem, Geophys. Res. Lett., 9, 717 – 720.

Spudich, P., Archuleta, R., 1987. Techniques for earthquake ground motion calculation with applications to source parameterization of finite faults, in Bolt, B.A. ed., SEISMIC STRONG MOTION SYNTHETICS: Orlando, Florida, Academic P

Spudich, P., Xu, L., 2002. Documentation of Software Package Compsyn sxv3.11: Programs for Earthquake Ground Motion Calculation Using Complete 1-D Green's Functions. International Handbook of Earthquake and Engineering Seismology.

Stride, A., Belderson, R., Kenyon, N., 1977. Evolving miogeoanticlines of the Eastern Mediterranean (Hellenic, Calabrian and Cyprus outer ridges). Philos. Trans. R. Soc. London, 282, 255-285.

Stucchi, M., Rovida, A., Gómez, A., Alexandre, P., Camelbeeck, T., Demircioglu, M., Gasperini, P., Kouskouna, V., Musson, R., Radulian, M., Sesetyan, K., Vilanova, S., Baumont, D., Bungum, H., Fäh, D., Lenhardt, W., Makropoulos, K., Martinez, J., Scotti, O., Giardini, D., 2012. The SHARE European Earthquake Catalogue (SHEEC) 1000–1899. Journal of Seismology. 17. 10.1007/s10950-012-9335-2.

Theodoulidis, N., 1991. Contribution to strong ground motion study in Greece. PhD Thesis, Aristotle University.

Theodulidis, N., Papazachos, B., 1992. Dependence of strong ground motion on magnitude-distance, site geology and macroseismic intensity for shallow earthquakes in Greece: I, Peak horizontal acceleration, velocity and displacement. Soil Dyn. & Earth. Eng., 11, p. 387-402.

Theodoulidis, N., Grendas, I., 2016. Near fault velocity pulse estimation: The Cephalonia Feb. 3, 2014 earthquake (M6.0). Bulletin of the Geological Society of Greece. [Online] 50:3

Theodoulidis, N., Karakostas, Ch., Lekidis, V., Makra, K., Margaris, B., Morfidis, K., Papaioannou, Ch., Rovithis, Emm., Salonikios, T., Savvaidis, A., 2016. The Cephalonia, Greece, January 26(M 6.1) and February 3, 2014(M 6.0) earthquakes: Near-faultground motion and effects on soil and structures, Bull. Earthq.Eng. 14, 1–38.

Triantafyllidis, P., Theodulidis, N., Savvaidis, A., Dimitriou, P. 2006. Site effects estimation using earthquake and ambient noise data: the case of Lefkas town. In: Proceedings of the First European conference on earthquake engineering and seismology. Geneva, paper 1249. 3–8 Sept 2006.

Tselentis, G.-A., 1993. Depth Dependent Seismic Attenuation in Western Greece. Tectonophysics, 225, 523-528.Bulletin of the Geological Society of Greece, XLIII/2, 754-762.

Tselentis, G., Danciu, L., 2010. Probabilistic seismic hazard assessment in Greece – Part 1: Engineering ground motion parameters. Natural Hazards and Earth System Science, 10(1), pp.25-39.

Utsu, T., 1999. Representation and analysis of the earthquake size distribution: a historical review and some new approaches, Pure Appl Geophys 155, 471–507.

Valkaniotis, S., Ganas, A., Papathanassiou, G., Papanikolau, M., 2014. Field observations of geological effects triggered by the JanuaryFebruary 2014 Cephalonia (Ionian Sea, Greece) earthquakes, Tectonophysics 630, 150–157, doi: 10.1016/j.tecto.2014.05.012.

Vamvakaris, D.A., 2010. Contribution to the study of the time dependant seismicity and the seismic hazard, Ph.D. thesis, Aristotle University of Thessaloniki, Greece, 428 pp., and 2 Appendices.

Vamvakaris, D., Papazachos, C., Papaioannou, Ch. Skordilis, Emm., Karakaisis, G., 2016. A detailed seismic zonation model for shallow earthquakes in the broader Aegean area. Natural Hazards and Earth System Sciences Discussions.

Wang, Z., 2009. Seismic Hazard vs. Seismic Risk. Seismological Research Letters. 80. 673-674. 10.1785/gssrl.80.5.673.

Waters, D., 1994. The tectonic evolution of Epirus, Northwestern Greece, PhD thesis, University of Cambridge, Cambridge, p. 248.

Wells, D.L., Coppersmith, K.J., 1994. New empirical relationships among magnitude, rupture length, rupture width, rupture area and surface displacement. Bull. Seism. Soc. Am., 84, 974-1002.

Wessel, P., Smith, W.H.F., Scharroo, R., Luis, J., Wobbe, F., 2013. Generic Mapping Tools: improved version released. Eos. Trans. AGU 94-45, 409–410. http://dx.doi.org/10.1002/2013 EO450001.

Wheeler, Russell L., 2009. Methods of Mmax Estimation East of the Rocky Mountains: U.S. Geological Survey Open-File Report 2009-1018, 44p.

Wiemer, S., Wyss, M., 1997. Mapping the frequency-magnitude distribution in asperities: an improved technique to calculate recurrence times? J Geophys Res 102(B7):15115–15128.

Wiemer, S., Wyss, M., 2000. Minimum magnitude of completeness in earthquake catalogs: Examples from Alaska, the Western United States, and Japan, Bull. Seismol. Soc. Am. 90, 859–869.

Woessner, J., Wiemer, S., 2005. Assessing the quality of earthquake catalogs: Estimating the magnitude of completeness and its uncertainty, Bull. Seismol. Soc. Am. 95, 684–698.

Wyss, M., Stefansson, R., 2006. Nucleation points of recent main shocks in Southern Iceland, mapped by b-values, Bull. Seismol. Soc. Am., 2006, vol. 96, pp. 599–608.

Young, J.B., Presgrave, B.W., Aichele, H.,Wiens, D. A., Flinn, E.A., 1996. The Flinn-Engdahl Regionalisation Scheme: the 1995 revision, Phys. Earth Planet. In., 96, 223–297.

Zahradnik, J., Sokos, E., 2015. Lefkada 17/11/2015, Mw 6.4 event: Quick estimate of source complexity, CSEM/EMSC Report.

Zhao, L., Chen, P., Jordan, T.H., 2006. Strain Green's tensors, reciprocity, and their applications to seismic source and structure studies, Bull. Seismol. Soc. Am. 96, no. 5, 1753–1763, doi: 10.1785/0120050253.